Influence of the local grain structure on the magnetization reversal behavior of ferromagnetic Co/Pt nanodots

Dissertation
zur Erlangung des Doktorgrades
an der Fakultät für Mathematik, Informatik und Naturwissenschaften
Fachbereich Physik
der Universität Hamburg

vorgelegt von

Eva-Sophie Wilhelm

Hamburg
2020

Gutachter der Dissertation:	Prof. Dr. Hans Peter Oepen Prof. Dr. Robert Blick
Zusammensetzung der Prüfungskommission:	Prof. Dr. Hans Peter Oepen Prof. Dr. Robert Blick Prof. Dr. Michael A. Rübhausen Prof. Dr. Michael Thorwart Prof. Dr. Ralf Röhlsberger
Vorsitzender der Prüfungskommission:	Prof. Dr. Michael A. Rübhausen
Datum der Disputation:	16. Juli 2020
Vorsitzender des Fach-Promotionsausschusses PHYSIK:	Prof. Dr. Günter Hans Walter Sigl
Leiter des Fachbereichs PHYSIK:	Prof. Dr. Wolfgang Hansen
Dekan der Fakultät MIN:	Prof. Dr. Heinrich Graener

Abstract

In this thesis the switching behavior of the magnetization of individual ferromagnetic Co/Pt nanodots and an ensemble of ferromagnetic double layer nanodots is studied. All dots were fabricated by a two step electron-beam lithography process and dry etching. Dot diameters down to 35 nm could be obtained on a Pt Hall cross with a width of 80 nm. The z-component of the magnetization of the nanodots was measured using the anomalous Hall effect (AHE). The influence of the local grain structure in the dots on the switching behavior is simulated with micromagnetic simulations and then compared to the experimental results.
First an almost coherent switching Co/Pt nanodot is discussed. The temperature dependent switching field is compared with a simple Sharrock equation. The blocking temperature and the anisotropy constant are obtained from the Sharrock fit. Deviations from the fit at very low temperatures ($\leq$ 50 K) are observed. Additionally a three dimensional analysis of the easy axis direction is given.
Also an ensemble of double layer nanodots with a 1 nm and a 0.8 nm layer of Co is studied. These layers were expected to be exchange decoupled by a 3 nm thick Pt interlayer. Therefor it was assumed that the two Co layers would switch separately. In the experiments however, a relatively broad switching field distribution is found and no separate reversal could be observed. The size distribution of the ensemble could be obtained from a SEM micrograph. For a virtual ensemble of 10 000 dots with a size distribution as measured, the influence of the different shape anisotropies due to the size distribution on the switching field distribution is calculated. These calculated distributions are compared to the experimental results. From this it can be concluded why the experimental switching field distributions become broader for lower temperatures. It is assumed that the influence of the local grain structure causes the broader experimental switching field distribution than the distributions found in the calculations.
In the second part two nanodots with clearly non-coherent reversal behavior are studied. The magnetization switches in two steps at lower temperatures, which results in two jumps in the hysteresis curve. From size, anisotropy and exchange stiffness, coherent rotation of a macrospin according to the Stoner-Wohlfarth model was expected, which would have resulted in one jump of the hysteresis only. The temperature dependence of both jumps in the hysteresis curves are discussed and the angular dependence of the switching field is studied at constant temperature.
Finally these results are compared to micromagnetic simulations that were done

using mumax3. In these simulation it is assumed that the nanodot consists of grains, as the polycrystalline films from which the dots were fabricated. It is found that the observed non-coherence reversal is not caused by the lack of exchange interaction between the grains. In fact, tilting of the crystallographic axes in the grains can cause inhomogeneous magnetization states and non-coherent switching behavior.

A simplified two grain model is used to investigate three different main tilting configurations of the crystallographic axes in the grains. For each configuration the influence of smaller and higher tilting angles was studied. In the first configuration a Bloch-like domain wall with a reduced wall angle is found. For stronger tilting the grains switch separately and a second jump occurs in the hysteresis curve. In the second tilting configuration quasi-coherent switching occurs for all angles. In configuration 3 only one grain is tilted and a Néel-like wall with a reduced wall angle is obtained for strong tilting. The grains switch also separately for strong tilting, which causes a second jump in the hysteresis curve. This last configuration exhibits surprising similarities in the hysteresis curves with the experimentally found results, when the magnetic field is applied in various directions.

Zusammenfassung

In dieser Arbeit wird das Schaltverhalten der Magnetisierung einzelner ferromagnetischer Co/Pt Nanopunkte und eines Ensembles ferromagnetischer Doppellagen Nanopunkte untersucht. Die Dots wurden durch zwei Elektronenstrahllithographie-Schritte und Trockenätzen hergestellt. Durchmesser kleiner als 35 nm konnten auf einem 80 nm breitem Hall Kreuz erreicht werden. Die z-Komponente der Magnetisierung wurde mit dem anomalen Hall-Effekt (AHE) gemessen. Der Einfluss der lokalen Kornstruktur in den Nanopunkten auf das Schaltverhalten wurde mittels mikromagnetischen Simulationen untersucht und mit den experimentellen Ergebnissen verglichen.

Als erstes wird ein nahezu kohärent schaltender Co/Pt Nanopunkt betrachtet. Das temperaturabhängige Schaltfeld wird mit einer einfachen Sharrock-Gleichung verglichen. Die „Blocking"-Temperatur und die Anisotropiekonstante können aus der Sharrock-Anpassung erhalten werden. Bei sehr niedrigen Temperaturen ($\leq 50\,\mathrm{K}$) werden Abweichungen von der Anpassung beobachtet. Außerdem wird eine dreidimensionale Analyse der Richtung der leichten Anisotropie Achse durchgeführt.

Anschließend wird ein Ensemble von Doppellagen Nanopunkten mit einer 1 nm und einer 0.8 nm dicken Co Schicht untersucht. Es war ursprünglich erwartet worden, dass diese Schichten durch eine 3 nm dicke Pt Zwischenschicht austauschentkoppelt ist. Daher wurde angenommen, dass die Magnetisierung der beiden Co Schichten einzeln schalten. In Experimenten wird jedoch eine relativ breite Schaltfeldverteilung gemessen und kein entkoppeltes Schaltverhalten beobachtet. Die Größenverteilung des Ensembles wurde mittels REM bestimmt. Für ein virtuelles Ensemble von 10.000 Punkten mit der gemessenen Größenverteilung, wird der Einfluss der unterschiedlichen Formanisotropien aufgrund der Größenverteilung auf die Schaltfeldverteilung berechnet. Diese berechneten Verteilungen werden mit den experimentellen Ergebnissen verglichen. Daraus kann geschlossen werden, warum die experimentellen Schaltfeldverteilungen bei niedrigeren Temperaturen breiter werden. Es wird vermutet, dass der Einfluss der lokalen Kornstruktur die breitere experimentelle Schaltfeldverteilung verursacht als die Berechnungen zeigen.

Im zweiten Teil werden zwei Nanopunkte mit deutlich inkohärentem Schaltverhalten untersucht. Die Magnetisierung schaltet in zwei Schritten, bei tieferen Temperaturen entstehen zwei Sprünge in den Hysteresekurven. Aufgrund der Größe, Anisotropie und Austauschsteifigkeit wurde jedoch kohärente Rotation eines Makrospins, wie durch das Stoner-Wohlfarth-Modell beschrieben, erwartet,

wobei dann nur ein Sprung in den Hysteresekurven sichtbar wäre. Die Temperaturabhängigkeit beider Sprünge in den Hysteresekurven wird diskutiert und die Winkelabhängigkeit des Schaltfeldes bei konstanter Temperatur untersucht.
Schließlich werden diese Ergebnisse mit mikromagnetischen Simulationen verglichen, die mit mumax3 durchgeführt wurden. In diesen Simulationen wurde angenommen, dass der Nanodot aus Körnen besteht, wie der ursprüngliche polykristalline Film aus dem die Dots hergestellt wurden. Es zeigt sich, dass die Inkohärenz im Schaltverhalten nicht durch die fehlende Austauschwechselwirkung zwischen den Körner verursacht wird. Tatsächlich kann ein Kippen der kristallographischen Achsen in den Körnern inhomogene Magnetisierungszustände und ein inkohärentes Schaltverhalten hervorrufen.
Ein vereinfachtes Zweikörnermodell wird verwendet um drei verschiedene Verkippungskonfigurationen der Anisotropie Achsen zu betrachten. Für jede Konfiguration wurde der Einfluss von kleineren und größeren Verkippungswinkeln untersucht. In der ersten Konfiguration wird eine Bloch-Wand ähnliche Domänenwand mit reduziertem Wandwinkel gefunden. Für größere Verkippungswinkel schalten die Körner einzeln und ein zweiter Sprung in der Hysteresekurve tritt auf. In der zweiten Konfiguration schaltet die Magnetisierung quasi kohärent für alle Verkippungswinkel. In der dritten Konfiguration wird nur ein Korn verkippt und es tritt für große Verkippungswinkel eine Néel-ähnliche Domänenwand mit reduziertem Wandwinkel auf. Die Körner schalten für starke Verkippung auch getrennt, was einen zweiten Sprung in der Hysteresekurve verursacht. Diese letzte Konfiguration zeigt überraschende Ähnlichkeiten in den Hysteresekurven mit den experimentell gefundenen Ergebnissen für in unterschiedlichen Richtungen angelegte Magnetfelder.

Contents

1 Introduction

Due to the digitalization of industries, smart innovations and the Internet of things (IoT), huge amounts of data are generated today. Every new car, modern homes and many other devices have sensors included to optimize safety, temperature and energy consumption, to water the plants and a multitude of other purposes. Various applications such as autonomous driving require artificial intelligence and therefore training data sets and new feedback data. Much of this data is collected and stored in huge data centers with enormous hunger for electricity. That is why The Guardian was headlining two years ago a «'Tsunami of data' could consume one fifth of global electricity by 2025». These numbers were based on predictions by Adrae and Edler [1], even though they are under debate [2–4], no doubt a lot of the energy is used in such data centers. A major amount of this energy is needed for cooling and much is discussed about improved concepts for cooling, but it is also estimated that about 10-20% of the energy is actually required for data storage [4, 5]. Renewable energy sources are built nowadays directly close to the data centers, but still carbon dioxide producing electricity sources are used. Already before all cooling and server architectural optimization is exhausted, new data storage concepts with higher storage density, fast accessing and writing rates, less power consumption, cheap costs and sustainable production will be needed. Fundamental research on magnetism is crucial to come up with new ideas for future data storage concepts.

In 1956, the first hard disc drive (HDD) with 5 MB and a storage density of $2\,\mathrm{kbit/in^2}$ was provided by IBM [6]. In 1986 floppy discs with 1.44 MB were brought to the market and were still quite common in the late 90s. Nowadays it is possible to carry a USB stick on a key ring with up to 1 TB, that is a multiple storage of a personal computer back then in the 90s. In USB sticks flash storage is used, which is a non-magnetic concept, but the more reliable and more cost efficient magnetic storage is still the major storage concept today. It relies on perpendicular magnetic recording (PMR) of a granular film. Today HDDs up to

16 TB are available with areal storage densities of around 1 Tbit/in^2 [7–9]. Among other optimization shingled magnetic recording (SMR) is used, this means slightly overlapping traces, in order to increase the areal density.
All these storage concepts come by miniaturization to a natural limit, for magnetic storage this is the superparamagnetic limit [10–12]. When a magnetic volume is switched a certain energy is necessary. The needed energy is equal to KV, where K is the effective anisotropy constant of the system and V the switched volume. This energy is provided by the magnetic field (for example of a write head) and thermal energy. When the volume becomes smaller, less energy is needed to switch the volume. If the ratio KV/k_BT becomes smaller than 40 to 80 however, uncontrolled switching of the magnetization may occur and the information stored is lost [11, 13]. Another approach is to increase the anisotropy constant K. However in that case more localized higher fields are needed for the writing, which are also limited [10].
To overcome this problem microwave assisted (MAMR) [14, 15] and heat assisted (HAMR) [16] storage concepts are suggested and implemented. They decrease the switching field of one bit temporarily and thus the storage density can be increased. An areal density of 1.97 Tbit/in^2 was demonstrated and with more optimization it is hoped to achieve an areal density up to 4 Tbit/in^2 [17]. Although prototypes exist already and they were announced to be available in 2019, none of these HDDs can be purchased at the beginning of 2020.
But also HAMR and MAMR have a limit in areal density and new ideas are necessary to handle the growing data amounts. One concept is bit patterned media (BPM) where tiny islands of hard magnetic material are produced and used to store one bit [18–20]. These islands are either fabricated by direct E-beam lithography, by self-assembled diblock copolymer or nano-imprint lithography [21–25]. It was suggested in 2016 by the Advanced Storage Technology Consortium (ASTC) roadmap [26] that by 2025 heated-dot magnetic recording (HDMR) could be available with areal densities expected up to 10 Tbit/in^2 or beyond [17].
For these kind of storages very controlled material properties are needed, since it is favorable to achieve a narrow switching field distribution (SFD), all bits should switch at almost the same magnetic field [24, 27–30]. This is also required because otherwise stray fields from the write head or other bits could accidentally switch weaker bits. Apart from data storage further interesting applications for superparamagnetic nanoparticles is medical magnetic particle imaging or drug delivery [31–33].

The aim of this thesis is to study realistic magnetic switching behavior of small Co/Pt nanometer sized discs, that are influenced by the local grain structure and describe deviations from the Stoner-Wohlfarth model [34]. These nanodiscs are referred to as nanodots.
There are many methods to investigate the average properties of an ensemble of nanodots. Such as SQUID[1] [35, 36], MOKE[2] [37–40] and VSM[3] [41, 42]. In order to verify the origin of switching field distribution and the switching process itself, investigations on individual nanodots are required. Such methods can be raster sensor methods, such as MFM[4] [27, 30, 42] and spin-polarized scanning tunneling microscopy [43, 44]. These methods are very time consuming though and need very clean sample surfaces. Also other imaging techniques as SEMPA[5] [45–47], Lorentz TEM [48, 49] and soft X-ray holographic microscopy (XHM) [50–52] can be used. While the two latter ones need very delicate sample preparation on thin membranes, all of these techniques are at least challenging to do in a wide temperature range (2 K to 300 K) and the application of higher magnetic fields (up to 1 T) might be technically difficult. Furthermore for SEMPA only a very thin Pt protection layer would be required and the residual e-beam resist needs to be removed. MicroSQUID needs also a complicated sample preparation and is restricted to very low temperatures [53–55].
In this thesis the anomalous Hall effect (AHE) is exploited to investigate the switching of individual nanodots. Some measurements were shown already by Schuh et al. [56]. The technique was further established by Kikuchi et al. [57–60] and on a Hall cross with several dots the signals can be attributed [61]. The major advantage of the Hall measurements is that they can be done at various temperatures (2 K to 295 K for the here used setup) in a cryostat and also high magnetic fields can be applied (here up to 6 T). Furthermore, micromagnetic simulations are used to understand the experimental results [62]. Here the influence of the polycrystalline film properties, that had been investigated in previous work [63–65], on the switching behavior of the magnetization was studied.

First in chapter 2 an overview of the theoretical background of reversal modes of magnetization with emphasis on the Stoner-Wohlfarth model is given. Also the Hall effects relevant for the presented experiments and the Landau-Lifschitz-

[1] superconducting quantum interference device
[2] magneto-optic Kerr effect
[3] vibrating sample magnetometer
[4] magnetic force microscopy
[5] scanning electron microscopy with polarization analysis

Gilbert equation, which is the base of the simulations, is described. In chapter 3 the experimental set-up and sample preparation is explained. Hall measurements were performed in cryostat with variable temperature and magnetic fields. The samples were fabricated by a two step e-beam lithography process and Ar ion etching from sputtered platinum cobalt film systems. The experimental part begins with quasi-coherent rotation of magnetization in nanodots in chapter 4. The results from a single Pt/Co/Pt nanodot and an ensemble of double Co layer nanodots are shown and discussed. Followed by results, simulations and a discussion of non-coherent reversal behavior in a single Pt/Co/Pt nanodot in chapter 5. Finally a conclusion and outlook are given in chapter 6.

2 Theoretical background

In this chapter all theory relevant for the experiments and simulation is summarized. It is mainly a introduction to the context. For detailed treatment the reader is referred to textbooks such as [66–68] and primary literature.
In the first section 2.1 of this chapter the reversal of magnetization is described. The energy terms that influence the reversal are introduced and the Stoner-Wohlfarth model of coherent rotation of the magnetization is presented. Also temperature dependence of the switching field is touched. The phenomenology of the anomalous, normal and planar Hall effect is described in the next section 2.2, since these effects are part of the measurements. Finally the Landau-Lifshitz-Gilbert equation is introduced (sect. 2.3) as all the simulations with mumax3 (in sect. 5.2) are based on this theory.

2.1 Reversal of magnetization

There are different major modes for magnetization reversal in ferromagnets. In bulk like material or films one of the most important mode is reversal by a propagation of a domain wall. In very small (nanoscale) structures different modes appear because domain walls are energetically unfavored. One mode is coherent rotation of the magnetization, where the magnetization behaves as one macrospin. Other intermediate modes are curling and buckling. For all modes different energetic contributions are relevant. These energy contributions will be summarized in the next section.
In section 2.1.2 single domain particles will be introduced, as a prerequisite for the Stoner-Wohlfarth model that will also be described. In the following section 2.1.3 the temperature dependence of the switching field will be presented. The last section 2.1.4 is about the switching field distribution.

2.1.1 Magnetic energy contributions

In this chapter a short summery of the magnetic energy contributions is given in order to make clear what affects the reversal behavior of the magnetization. Detailed description can be found in [66].
The total energy of a ferromagnetic system E_{tot} can be described by the following contributions: the exchange energy E_{exch}, the anisotropy energy E_{anis}, the demagnetization energy E_{demag} and the Zeeman energy E_{Zeeman}

$$E_{\mathrm{tot}} = E_{\mathrm{exch}} + E_{\mathrm{anis}} + E_{\mathrm{demag}} + E_{\mathrm{Zeeman}} \; (+ E_{\mathrm{elast.}} + E_{\mathrm{magstat}}) \tag{2.1}$$

Depending on which term is dominating different magnetic configurations and reversal behavior can be found. Each contributing energy term will be briefly described in the following paragraphs:

Exchange energy The parallel alignment of magnetic moments in a ferromagnet is caused by the long-ranged exchange interaction. Its origin can be found in the quantum mechanics and is caused by the in total asymmetry of the wave function for fermions consisting of local and spin term (Pauli principle).

Anisotropy energy In some systems certain directions are energetically preferred or avoided by the magnetic moments due to magnetocrystalline and additionally for thin samples interfacial anisotropy. These directions are called easy or hard axis (e.a. or h.a.) and also easy or hard plane. The reason for magnetocrystalline anisotropy is spin-orbit coupling regarding the crystalline axes of a system.
In uniaxial systems the magnetocrystalline anisotropy energy can be described by a Taylor expansion with the direction sine (θ is the angle between film normal and magnetization) and the magnetic anisotropy constants:

$$E_{\mathrm{anis}}^{\mathrm{magnetocryst}} = V K_{1,V} \sin^2(\theta) + V K_{2,V} \sin^4(\theta) + \mathcal{O}(\sin^6(\theta)) \tag{2.2}$$

For the surface anisotropy only the first order is considered, thus it can be approximated by:

$$E_{\mathrm{anis}}^{\mathrm{surf}} = 2V \frac{K_{\mathrm{S}}}{t} \cdot \sin^2(\theta) \tag{2.3}$$

where t is the thickness of the sample and the factor 2 corresponds to two interfaces of thin films.

Demagnetization energy This energy contribution describes the change in stray field energy due to different configurations of magnetization. It strongly depends on the shape of the system. In this work only thin films and thin discs are considered. The demagnetization energy of a ultra-thin cylindrical nanodot is described by Millev et al. [69]. Often the demagnetization energy is also referred to as shape anisotropy.

Zeeman energy The Zeeman term refers to the energy of a magnetic moment in a external magnetic field. It is given by the integral of the product of local magnetization $\vec{M}$ and external field $\vec{H}$ over the whole volume of the sample:

$$E_{\text{Zeeman}} = -\mu_0 \int_V \vec{M} \cdot \vec{H} \ \mathrm{d}V \tag{2.4}$$

It can be simplified for uniform magnetization (also referred to as macrospin) and homogeneous field to:

$$E_{\text{Zeeman}} = -\vec{m} \cdot \mu_0 \vec{H} \tag{2.5}$$

Furthermore also elastic and magnetostatic energy within double layers ($E_{\text{elast.}}$ and E_{magstat}) could be relevant in a system of a nanodot described here. However elastic energy will not be further considered within this thesis since it does not seem to show any influence. Only magnetostatic interaction will be discussed briefly in the case of double layer nanodots in chapter 4.2.

2.1.2 Coherent rotation of a macrospin

Reversal modes of magnetization, describing the way the magnetization switches, are determined by the interplay of the different magnetic energy terms described in the previous section. Depending on the size, shape, anisotropy, saturation magnetization and exchange interaction different switching modes can be found: The most simple mode for small structure in the nanometer regime is coherent rotation of a macrospin which can be described by the Stoner-Wohlfarth (SW) model [34]. Furthermore buckling and curling are discussed in literature [70]. Also reversal through nucleation and propagation of a domain wall is possible [71]. Simulation results showing this can be found in [72, 73] and experimental evidence in [27, 74].

Critical diameter for coherent rotation

The exchange interaction influences the magnetic moments in a ferromagnet to align parallel. The opposite influence is given by the demagnetization energy, a reduced stray field can be found if magnetic moments align anti parallel or rotational configuration within the sample. For small systems with lower anisotropy flux closure configurations like e.g. the Landau, diamond or vortex state can be found [68]. Systems with higher uniaxial anisotropy tend to exhibit magnetic domains[1] pointing (anti)parallel to one distinct direction, due to the equilibrium between exchange interaction, demagnetization energy and anisotropy energy.
In very small systems with comparably magnetostatic exchange interaction length $l_0 = \sqrt{\frac{2A_{\mathrm{ex}}}{\mu_0 M_S^2}} = 5\,\mathrm{nm}$ [66] (with $M_S = 1440\,\mathrm{kA\,m^{-1}}$ the saturation magnetization [75] and $A_{\mathrm{ex}} = 31.4\,\mathrm{pJ}$ the exchange constant for hcp Co [76]) the minimum energy configuration is a single domain state. Different assumptions like the domain wall width and comparison with polydomain configurations lead to different critical diameter for single domain particles. Single domain configuration is a necessary but not sufficient criterion for the assumption of coherent rotation of magnetization, which can be then described as a macrospin in the Stoner-Wohlfarth model. A critical diameter for coherent rotation in very thin films was found by Skomski as $D = 11.4\frac{l_0^2}{t}$ [77]. For our typical exchange length of 5 nm we obtain then $D \approx 290\,\mathrm{nm}$ for a 1 nm thick Co film. For thicker film with $t_{\mathrm{Co}} = 1.4\,\mathrm{nm}$ the critical diameter is $D \approx 205\,\mathrm{nm}$.
These values can be compared with the Bloch wall width $\delta_0 = \pi\sqrt{\frac{A}{K_{\mathrm{eff}}}} \approx 31.5\,\mathrm{nm}$ [66] (for a dot with $K = 300\,\mathrm{kJ/m^3}$). For dots with smaller anisotropy the Bloch wall width becomes even wider. The dots investigated in this thesis have a diameter of 30 nm to 65 nm and should be in principle single domain particle and reverse by coherent rotation. However it will be shown in chapter 5 why this is not always the case.

Stoner-Wohlfarth (SW) model

The most common and simple model for magnetization reversal is the coherent rotation of a macrospin in a system with uniaxial anisotropy, which was first described by Stoner and Wohlfarth [34]. Depending on the angle θ between magnetization and the easy axis of the system (here also z-axis) and the direction of the applied external field (angle φ between easy axis and applied field) the

[1] Domains are areas with uniform magnetization separated by magnetic domain walls. Domain walls are the areas between domains, here the magnetization changes gradually.

total energy density of the system can be written as:

$$\frac{E_{\text{tot}}}{V} = K_{\text{uniax}} \sin^2(\theta) - \mu_0 M_{\text{S}} H \cos(\varphi - \theta) \tag{2.6}$$

For theoretical discussion this equation can be expressed in a reduced form with the reduced field $h = \frac{H}{H_{\text{K}}}$ using the anisotropy field $H_{\text{K}} = \frac{2K}{\mu_0 M_{\text{S}}}$ and the reduced energy density f:

$$f = \frac{E_{\text{tot}}}{K_{\text{uniax}} V} = \sin^2(\theta) - 2h \cos(\varphi - \theta) \tag{2.7}$$

The minimum regarding θ can be calculated ($\frac{\partial f}{\partial \theta} = 0$ and $\frac{\partial^2 f}{\partial \theta^2} = 0$), from this the magnetization direction for a given field strength and direction is received.
When we plot the projection of the magnetization on the field over the field strength, we receive typical hysteresis curves as in fig. 2.1 a). If the magnetic field is applied in the direction of the easy axis (0°) an open hysteresis curve with square shape is the result. The magnetization switches at the anisotropy field $h = \frac{H}{H_{\text{K}}} = 1$.
If the magnetic field is applied in hard axis direction (90° to the easy axis) a closed hysteresis with a certain non-zero slope through the origin and kinks at the anisotropy field $h = 1$. For all other angles the shape is curved and in between easy and hard axis.

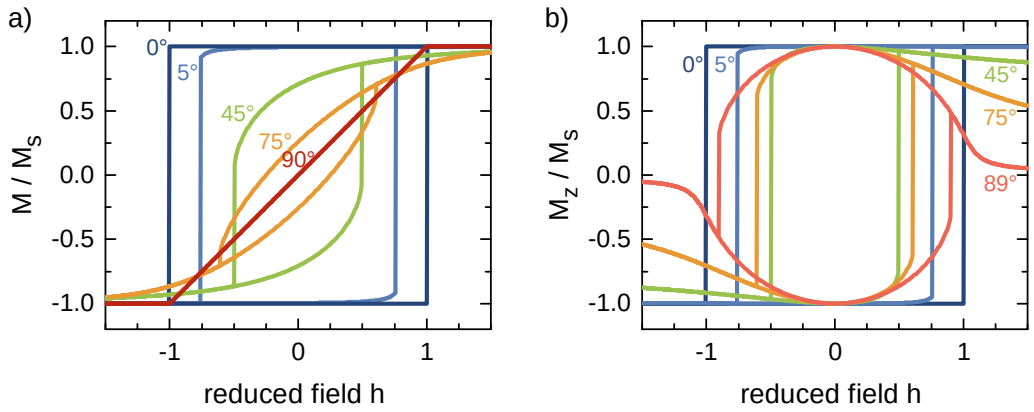

fig 2.1 Stoner-Wohlfarth hysteresis curves with external field applied in different directions. In a) the magnetization vector is projected on the direction of the magnetic field. In b) M_z, the projection of the magnetization vector on the z-axis of the system is shown. The M_z component is also the quantity received from the anomalous Hall measurements within this thesis.

Since our measurement exploit the anomalous Hall effect (see sect. 2.2.2), which is sensitive to the z-component only the projection of the magnetization on the z-axis is relevant within this thesis and is depicted in fig 2.1 b).

The coercive field H_c is defined as the field where the magnetization is zero[2].

For a parallel or perpendicular direction of the applied field towards the easy axis the coercive field H_c is equal to the anisotropy field H_K while for all other angles of φ H_c is smaller (compare fig 2.1).

The energetic landscape is described by the energy density f (eq. 2.7). It is different for every angle of the applied field. Two cases, parallel ($\varphi = 0$) and perpendicular ($\varphi = 90°$) to the easy axis, are shown in fig 2.2. For zero field (dark blue curve) two minima ($\theta = 0°$ and $\theta = 180°$), separated by an energetic barrier ($\theta = 90°$), appear, they correspond to up and down configuration of the magnetization. If a field $h = 0.2$ is applied in parallel direction the minimum at $\theta = 0°$ decreases and the minimum at $\theta = 180°$ increases. For higher fields the difference between the two minima increases further. When the anisotropy field H_K is reached, the reduced field h becomes equal to 1 and the minimum at $\theta = 180°$ becomes a saddle point. Thus anti-parallel configuration of the magnetization becomes instable and a switching occurs if the magnetization was pointing anti-parallel to the applied field.

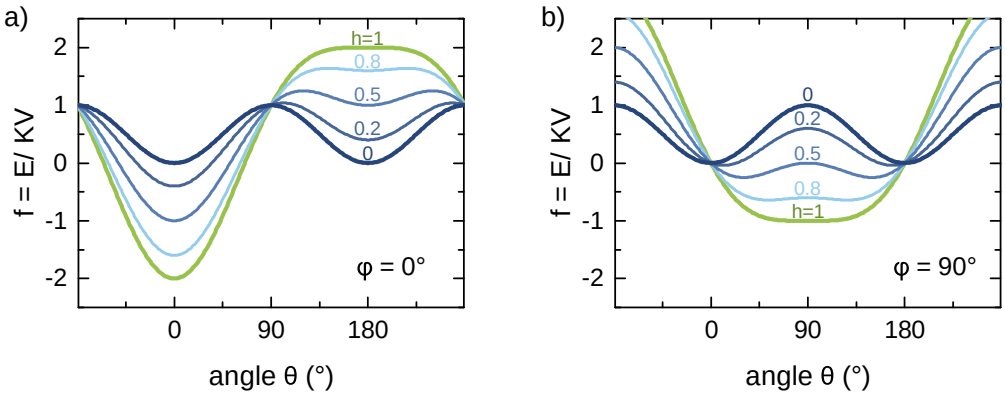

fig 2.2 a) Energetic landscape for an applied field parallel to the easy axis of the system (here also the z-axis ($\varphi = 0$)). b) for an applied field perpendicular to the easy axis ($\varphi = 90°$). θ is the angle between the magnetization and the easy axis.

[2]The coercive field is defined as $H_c := H(M = 0)$. It is often used synonymously with the switching field H_{sw}, which is defined as the field where $\frac{dM}{dH}$ is maximum. Within the Stoner-Wohlfarth mode $H_c = H_{sw}$, but for other reversal processes this is not always the case, as for example in [78].

For an applied field in the hard plane of the system the situation is different. For $h = 0.2$ the potential barrier decrease and the value of the minima is smaller, but also the position on the θ-axis changes. It moves towards the barrier. This means that the energetic minimum for the magnetization is not at $\theta = 0°$ and $\theta = 180°$ but at $\theta = 12°$ and $\theta = 168°$, the magnetization starts to rotate away from the easy axis direction. This trend continues for higher field values till at $h = 1$ ($H = H_K$) the barrier vanishes and a minimum appears at $\theta = 90°$ which corresponds to saturation in the applied field direction. This behavior can be seen also in the hysteresis curves in 2.1. For field direction between $\varphi = 0°$ and $90°$ the behavior is a mixture of both cases, showing rotation and sudden switching, which becomes visible also in the hysteresis curves, but will not be discussed further regarding the energetic landscapes.
Also from minimization of f (eq. 2.7) regarding θ and solving of a linear equation system the coercive field depending on the direction of the external magnetic field can be found:

$$H_c = H_K(\cos^{2/3}(\varphi) + \sin^{2/3}(\varphi))^{-3/2} \tag{2.8}$$

A plot of the coercive field strength over the angle φ of the external field towards the easy axis gives the following diagram in fig 2.3 a). The symmetry of the coercive field to $\varphi = 0°, 90°$ is a strong indication for Stoner-Wohlfarth behavior in magnetic systems.

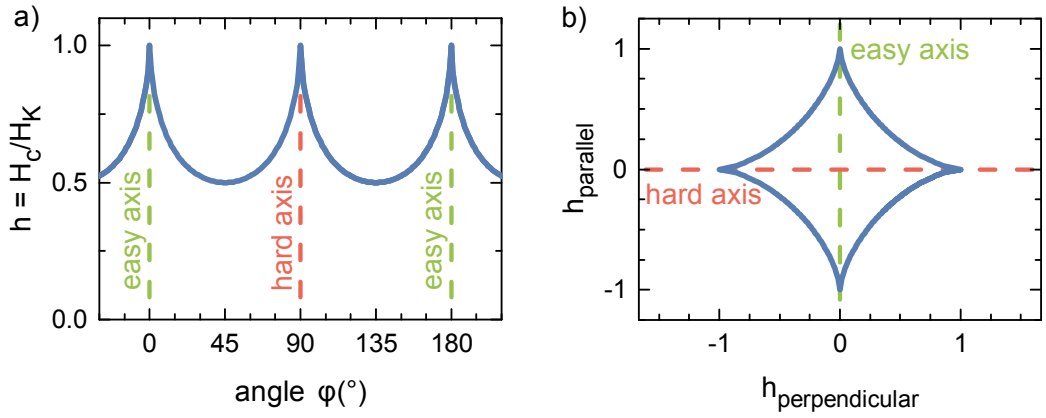

fig 2.3 a) Reduced coercive field over the angle φ between the applied field and the easy axis of the system (here also the z-axis). b) A Stoner-Wohlfarth asteroid in 2 dimensions.

Another very common picture is the Stoner-Wohlfarth asteroid [34] where the applied field is separated in a component parallel and perpendicular to the easy

axis and the coercive field h_c is plotted according to its components parallel and perpendicular as shown in figure 2.3 b).
A comprehensive summery of the Stoner-Wohlfarth model can be found in [79].

2.1.3 Temperature dependence of the switching field

Now we consider the influence of a temperature $> 0\,\mathrm{K}$ on the switching field of a system with coherent rotation of a macrospin. The thermal energy helps the system to overcome the energetic barrier and thus lowers the switching field with increasing temperatures. We start with the Néel-Arrhenius law [80–83]

$$\tau = \tau_0 e^{\frac{\Delta E}{k_B T}} \tag{2.9}$$

with the relaxation time τ, $\tau_0 = \frac{1}{f_0} = 10^{-11} - 10^{-9}\,\mathrm{s}$ [84] and f_0 the attempt frequency[3]. Without field the energy barrier is $\Delta E = KV$. Thus the switching becomes harder for systems with high anisotropy or volume. For small particles eventually the temperature and thus the thermal energy is high enough for the macrospin of the system to overcome the barrier by thermal fluctuations. This phenomena is called superparamagnetism. The particles behave similar to a paramagnet but with a high susceptibility. A critical temperature, the blocking temperature T_B is defined as:

$$T_B = \frac{\Delta E}{k_B \ln(\tau/\tau_0)} = \frac{KV}{k_B \ln(\tau/\tau_0)} \tag{2.10}$$

τ is here the measuring time and actually depends on the type of experiment, often the definition for T_B is $\tau = 100\,\mathrm{s}$ and $\tau_0 = 1\,\mathrm{ns}$, which gives a value of $\frac{KV}{k_B T_B} \approx 25$ [85]. When a magnetic field is applied, the energy barrier has to be modified. If we assume coherent rotation of a macrospin the Stoner-Wohlfarth model can be used:

$$\Delta E(H) = KV \left(1 \pm \frac{H}{H_K}\right)^2 \tag{2.11}$$

for magnetic fields parallel to the anisotropy axis, with the anisotropy field $H_K = \frac{2K}{\mu_0 M_S}$. Rearranging this equation ($H = H_C$), using eq. 2.9 and the

[3] The switching frequency $f = \frac{1}{\tau}$ and the attempt frequency $f_0 = \frac{1}{\tau_0}$ are also often used to express the Néel-Arrhenius law.

definition for the blocking temperature 2.10, gives [86, 87]:

$$H_C^{\text{Sharrock}}(T) = H_K\left(1-\sqrt{\frac{\Delta E}{KV}}\right) = H_K\left(1-\sqrt{\frac{k_BT}{KV}\ln\frac{\tau}{\tau_0}}\right) = H_K\left(1-\sqrt{\frac{T}{T_B}}\right) \tag{2.12}$$

This equation is called also the Sharrock equation, even though a similar equation was found already by Kneller and Wohlfarth [88, 89]. The Sharrock equation can be used in the experiments within this thesis because all measurements within one experiment are done with the same sweeping rate and thus have the same blocking temperature, which is here defined by the measuring time τ_m. This has a major advantage if only switching fields are measured. The volume, the relaxation time τ and the prefactor τ_0 are contained in the blocking temperature T_B, which can serve as a fit parameter and is equivalent to the temperature where the switching field becomes zero for the specific sweep rate of magnetic field in the hysteresis measurement.

Other experiments such as telegraph noise experiments, measuring τ, give also insight in the magnetic moment ($m = M_S V$). One can then insert the volume in the more sophisticated and slightly more accurate Garg equation [90], which will be presented briefly in the following: From the switching frequency and the expectation value of the switching field, the thermal dependence of the switching field has been deduced for the general case by Garg [91]. How to apply this theory to the case of a magnetic particle and a comparison with other approaches can be found in the PhD thesis of Neumann [90]. The result for the temperature dependence of the coercive field is:

$$H_C(T) = H_K\left[1-\left(1+\frac{\gamma_{EM}}{2\ln\left(\frac{k_BTf_0\mu_0H_k}{R2KV}\right)}\right)\sqrt{\frac{k_BT}{KV}\ln\left(\frac{k_BTf_0\mu_0H_K}{2RKV}\right)}\right] \tag{2.13}$$

with the sweeping rate of the magnetic field R and the Euler-Mascheroni constant $\gamma_{EM} \approx 0.5772$. It has to be taken into account that f_0 and V seem to depend on each other in the fits (or values for f_0 have to be assumed that are several magnitudes off the expected range $1 \times 10^{12}\,\text{s}^{-1}$ to $1 \times 10^{35}\,\text{s}^{-1}$), as a consequence only f_0 and K can be fitted at once. In principle f_0 also depends on various parameter such as the anisotropy, saturation magnetization, temperature and volume, but can be considered as constant within this thesis.

2.1.4 Switching field distribution (SFD)

Since all experiments take place at a temperature above 0 K, the switching will be a stochastic process. If an external field is ramped and an ensemble of identical nanodots switches they will have a certain distribution of switching fields with one mean field and a certain width. The same applies for a single nanodot that switches many times (e.g. 1000 or more). The width of this switching field distribution is very important for application since it is in most cases desired that all dots switch in a certain magnetic field range only and the width of the distribution needs to be known. We start with a simple rate equation:

$$\frac{dn_{\mathrm{down}}}{dt} = -f_{-}n_{\mathrm{down}} + f_{+}n_{\mathrm{up}} \tag{2.14}$$

where $n_{\mathrm{down}}, n_{\mathrm{up}}$ is the number of dots with magnetization up or down and f_{-} and f_{+} the switching frequency for up and down:

$$f_{\pm} = f_0 \exp\left[-\frac{KV}{k_{\mathrm{B}}T}\left(1 \pm \frac{H}{H_K}\right)^2\right] \tag{2.15}$$

which is eq. 2.9 with eq. 2.11 inserted and converted to frequencies. It is assumed now that $f_{+} = 0$, since the magnetization of the dot points up, is in the blocked state and the field is applied in down direction. Thus the rate for the magnetization switching back is negligible small (see also [92]). The number of particles in the down (and up state correspondingly) can be expressed by the probability p_{not} that the dot has not switched and the number of the dots n: $n_{\mathrm{down}} = np_{\mathrm{not}}$. We get the master equation [92]

$$\frac{dp_{\mathrm{not}}}{dt} = -f_{-}p_{\mathrm{not}} \tag{2.16}$$

and as a solution of this equation:

$$\ln p_{\mathrm{not}} = -\int_{-\infty}^{t_0} f_{-}dt \tag{2.17}$$

The probability for switching can be expressed as $p_{\mathrm{sw}} = 1 - p_{\mathrm{not}}$ since the sum of both have to be equal 1. Thus the change of the probability of switching with the change of the magnetic field gives:

$$SFD = \frac{dp_{\mathrm{sw}}}{dh} = -\frac{dp_{\mathrm{not}}}{dt}\frac{dt}{dh} \tag{2.18}$$

The external field is sweeped with a certain rate and thus can be expressed as $\mu_0 H(t) = Rt$ and thus $\frac{dt}{dh} = \frac{\mu_0 H_K}{R}$ (with the normalized field $h = \frac{H}{H_K}$). If the

solution eq. 2.17 and the master equation 2.16 are inserted the following is received for the switching field [91]:

$$SFD(h) = \frac{\mu_0 H_K}{R} f_-(h) \exp\left(-\frac{\mu_0 H_K}{R} \int_{-1}^{h} f_-(h')dh'\right) \tag{2.19}$$

The integral can be solved numerically. For high sweeping rates of the magnetic field, the field dependence of the attempt frequency f_0 has to be considered, that will however not be the case for the presented experiments (max. $0.5\,\mathrm{T\,min^{-1}}$ sweeping rate). A detailed discussion on this topic can be found in [90, 92] and also for the field dependent switching rates in [84].

2.2 Hall Effects

Several different effects carry the name Hall effect. Many of them have in common that a voltage can be measured perpendicular to a current due to a magnetic field or due to spin dependent scattering. The z-component of the magnetization (current applied in x-direction, transverse voltage measured in y-direction) in the Pt/Co/Pt nanodots is probed by the anomalous Hall effect (AHE). But also the normal Hall effect (NHE) and the planar Hall effect (PHE) can influence the measured signal[4].

2.2.1 The normal Hall effect (NHE)

The normal Hall effect[5] (NHE) is present in metals and semi-conductors and describes a transversal voltage due to a magnetic field perpendicular to the applied current. The normal Hall effect is caused by the Lorentz force. It can be used to measure the magnetic field strength, usually semiconductors are used for this purpose[6]. For Co the following NHE constants were reported: -0.24×10^{-10} to $-1.3 \times 10^{-10}\,\mathrm{m^3/(As)}$ [93]. The values may vary with the the residual resistivity ratio (RRR), thickness and actual crystal phase and purity of the material. For the NHE constant of polycrystalline Pt bulk values of -2.2×10^{-11} and $-2.44 \times 10^{-11}\,\mathrm{m^3}$ /(As) exist but would decrease to $-1.5 \times 10^{-11}\,\mathrm{m^3}$ /(As) for 5 nm thick films [93].

[4] Furthermore the Quantum Hall effect, the spin Hall effect (here not a voltage but a spin imbalance appears) and the quantum spin Hall effect exist, but are not subject within this thesis.

[5] also ordinary Hall effect

[6] Since the normal Hall constant depends like $R_{\mathrm{NHE}} = \frac{1}{qn^*}$ on the charge carrier density n^*, which is usually lower in semiconductors, thus resulting in a high R_{NHE}. The sign of R_{NHE} depends on the character of the charge carrier ($q = e$ for holes or $q = -e$ for electrons).

2.2.2 The anomalous Hall effect (AHE)

The anomalous Hall effect[7] can be found in ferromagnetic material only. It is a transversal voltage that is caused by asymmetric scattering of the spin-polarized electrons in the ferromagnet due to spin orbit interaction. The voltage U_{Hall}, which is the sum of NHE and AHE, can be measured perpendicularly to a current and the magnetization of a system. If the applied current lies in the x-direction and the Hall voltage is measured in the y-direction the following empirical equation can be applied [94]:

$$U_{\mathrm{Hall}} = \mu_0 (R_{\mathrm{NHE}} H_z + R_{\mathrm{AHE}} M_z) \frac{I_x}{t} \tag{2.20}$$

Where t is the thickness of material, R_{AHE} the anomalous Hall constant of a material. In the case of Co the anomalous Hall constant is of opposite sign compared to the normal Hall constant and the AHE is one order of magnitude higher than the NHE. The NHE therefore can either be neglected or the data can be corrected by subtracting a linear slope.
In our measurement design the anomalous Hall effect is used as a probe of the z-component of the magnetization in the samples. The values from literature are different for each Co system. The AHE values range from $0.19{-}0.83 \times 10^{-10}\,\mathrm{m}^3/(\mathrm{As})$ for bulk systems and from $8{-}20 \times 10^{-10}\,\mathrm{m}^3/(\mathrm{As})$ for thin films (up to 200 nm thickness) [93].
The AHE resistivity depends on the zero-field resistivity ρ_{xx} and is therefore dependent on temperature, Kötzler et al. investigated a system similar to our Co films and found the following dependence: $\rho_{\mathrm{AHE}} = \sigma_{xy}\rho_{xx}^2 + a\rho_{xx} = \mu_0 R_{\mathrm{AHE}} M_z$, where a is small and σ_{xy} is temperature independent [95]. The exact relation with temperature strongly depends on the system under investigation. There are contributions by defects, structure and for thin samples interfaces (scattering). Also the size constriction in nanostructures may contribute to scattering as well. Further literature about NHE and AHE can be found in [96,97] and a more recent review on AHE in [98].

2.2.3 Planar Hall effect (PHE)

The planar Hall effect (PHE) is another effect which can produce a transversal voltage. It depends on the in-plane component of the magnetization and the magnetic field [99]. The origin of the PHE are non-isotropic magnetoresistance

[7] also extraordinary Hall effect.

effects such as the anisotropic magnetoresistance effect and the Lorentz magneto resistance effect [93, 100, 101]. The effect has nothing to do with other Hall effects. Since it does not change the sign, when the magnetic field or magnetization is reversed (it is even in B), the name Hall effect is not appropriate, but historically established.

The generalized Ohm's law (in thermal equilibrium) can be written as follows:

$$\mathbf{j} = \overline{\overline{\sigma}}\,\mathbf{E} \qquad \Leftrightarrow \qquad \mathbf{E} = \overline{\overline{\rho}}\,\mathbf{j} \tag{2.21}$$

$\mathbf{j}$ is the current density vector, $\mathbf{E}$ the electric field vector, $\overline{\overline{\sigma}} = \overline{\overline{\rho}}^{-1}$ the electrical conductivity tensor and $\overline{\overline{\rho}}$ the electrical resistivity tensor. From a Taylor expansion and symmetry considerations the following equation can be deduced [102]:

$$\mathbf{E} = \rho_\perp \mathbf{j} + \mathbf{n}(\mathbf{j}\cdot\mathbf{n})(\rho_\parallel - \rho_\perp) + \rho_H \mathbf{n}\times\mathbf{j} \tag{2.22}$$

with $\mathbf{n} = (\sin\theta\cos\phi, \sin\theta\sin\phi, \cos\theta)^T$ the unity vector in the direction of $\mathbf{B} = \mu_0(\mathbf{H}+\mathbf{M})$ and the azimuthal angle ϕ. When the current is applied in x direction, the resulting electric field for the y-direction (the transversal direction) is:

$$E_y = (\rho_\parallel - \rho_\perp) j_x \sin^2\theta \sin\phi\cos\phi - \rho_{\mathrm{AHE,NHE}} \cos\theta M j_x \tag{2.23}$$

The last term corresponds to the normal and anomalous Hall effect. The first term to the planar Hall effect. If we apply a field in the xy-plane only, the measured planar Hall resistivity ρ_{PHE} is described by the difference between the resistivity with the magnetization or field parallel to the current ($\rho_\parallel$) and the resistivity when the magnetization or magnetic field is perpendicular to the current ($\rho_\perp$) and the angle α between the actually applied field or magnetization and the current. Since the current is applied in x direction, $\phi = \alpha$ and [101, 102]:

$$\rho_{\mathrm{PHE}} = \underbrace{(\rho_\parallel - \rho_\perp)}_{\Delta\rho_{\mathrm{AMR}}} \sin\alpha\cos\alpha. \tag{2.24}$$

The angle dependence is depicted in fig 2.4. If the anisotropic magneto resistance (AMR) is the only anisotropic resistance, then the difference $\rho_\parallel - \rho_\perp$ corresponds to $\Delta\rho_{AMR}$. But also other resistivity effects may cause planar Hall voltage. If the magnetic field and magnetization are not restricted to the xy-plane, than also a dependence on θ has to be considered.

In the case of this thesis the magnetic field is rotated between xy-plane and z-axis in the direction $\alpha = 45°$. The PHE is maximal in that direction (with

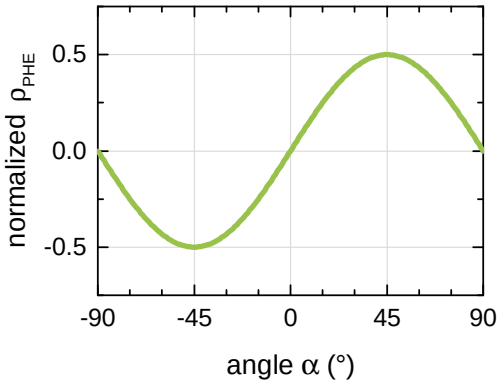

fig 2.4 Normalized PHE resistivity over the angle α. α is the angle between magnetization direction and current direction.

$\cos 45° = \sin 45° = \frac{1}{\sqrt{2}}$) and

$$\rho_{\mathrm{PHE}} = \frac{(\rho_{\parallel} - \rho_{\perp})}{2} \sin^2 \theta \tag{2.25}$$

can be used to describe the angle dependence with z-direction (θ: angle between z-axis and $\mathbf{B}$).

2.3 Micromagnetic simulations

Since it is very difficult to find the global minima of all energy terms in eq 2.1, in micromagnetic simulations commonly a different approach is used. All influences (Zeeman field, magnetostatic field, Heisenberg exchange field, magnetocrystalline anisotropy field) are summarized in an effective field H_{eff} and the Landau-Lifshitz-Gilbert (LLG) is used to calculate the change of the magnetization [62]:

$$\frac{\mathrm{d}\mathbf{M}}{\mathrm{d}t} = \gamma \mathbf{M} \times \mathbf{H}_{\mathrm{eff}} + \frac{\alpha}{M_S} \mathbf{M} \times \frac{\mathrm{d}\mathbf{M}}{\mathrm{d}t} \tag{2.26}$$

$$= -\frac{\gamma}{1+\alpha^2} \mathbf{M} \times \left(\mathbf{H}_{\mathrm{eff}} + \frac{\alpha}{M_S} \mathbf{M} \times \mathbf{H}_{\mathrm{eff}} \right) \tag{2.27}$$

with α the damping parameter and $\gamma = g\mu_B/\hbar$ the gyromagnetic ratio. The first term in 2.26 describes rotation of the magnetic moments due to $\mathbf{H}_{\mathrm{eff}}$. The second term describes the damping caused by dissipation. The LLG is numerically solved for small cells defined in the simulation (here cuboid). The cells have

uniform magnetization and have to be smaller than the characteristic length scales such as magneto static exchange length or Bloch domain wall width. A widely used magnetization software is OOMMF[8] [103] The simulation within this thesis were done with mumax3 which provides faster simulations on a GPU [62, 104]. Temperature is not considered here, thus $T = 0\,\mathrm{K}$ is assumed. Detailed reviews on micromagnetic simulations can be found in [104–106]

[8] object oriented micromagnetic framework

3 Sample preparation and experimental setup

In the first part of this chapter the used Co/Pt layer system and the following structuring process of the nanodots on Hall bars is described. In the second part the set-up for Hall measurements with variable temperature is presented. Finally the residual resistivity (RRR) of the samples is discussed and compared to previous results.

3.1 Pt/Co/Pt film system

Co/Pt layered systems with perpendicular magnetic anisotropy (PMA) are widely examined systems since the late 80s [107]. The origin of the PMA is the interface or surface anisotropy which becomes dominant for ultrathin films.
Competing with shape anisotropy and magnetocrystalline anisotropy the easy axis of magnetization is out-of-plane for thicknesses below 1.2 nm to 1.5 nm and in-plane for the thicker sample regime. They have been studied in our group [63–65,108–112] and the detailed fabrication procedure can be found there in. Here a short overview is given. The film systems are sputter deposited on silicon wafers with a several hundred μm thick layer of SiO_2 or Si_4N_3. The sputtering process is done in a ultrahigh vacuum chamber with a base pressure below $2 \cdot 10^{-9}$ mbar. The films are polycrystalline. For layer-by-layer growth at first a Pt seed layer of either 4 or 6 nm is deposited with ECR sputtering[1] at an argon pressure of $p_{\mathrm{Ar}} = 3 \times 10^{-4}$ mbar. This seed layer yields smooth interfaces and a high quality <111> texture. A 1 nm to 3 nm thick Pt layer is deposited by DC magnetron sputtering on top of the ECR layer [111]. Then the desired Co layer (or sequence of Co and Pt layers) is deposited by DC magnetron sputtering ($p_{\mathrm{Ar}} = 3 \times 10^{-3}$ mbar). Finally a 3 nm Pt layer is applied (DC magnetron) in order to protect the Co from oxidation later on on air. The anisotropy of the resulting film systems is characterized by MOKE[2] and after each bake out of the used UHV chamber the layer quality and thickness is additionally verified via XRR[3] measurements.

[1] ECR: electron cyclotron sputtering
[2] MOKE: Magneto optical kerr effect
[3] XRR: X-ray reflectivity

Structural properties

In SEM micrographs of the a broken film sample and HRTEM measurement by Winkler et al. [63], a columnar growth of the grains could be observed. For thick films ($t_{Co} = 50\,\text{nm}$), the lateral grain structure of the polycrystalline film can be imaged by SEM[4] as depicted in fig 3.1 a). With a Fourier transformation (see fig 3.1 b)) the average grain size can be calculated. From this a grain size of 16 nm is received. Because of the columnar growth the results of the thick sample can be most likely also assumed for thinner samples. In a previous work by Kobs a grain size of 11 nm was found [65].
From XRD measurement by Winkler et al. [63] it was concluded that the Co grows in a fcc(111) structure.
For a Pt(5 nm)/Co(3.5 nm/Pt(3 nm) film system on SiO_2, they measured a rocking scan of a Pt peak, that can be fitted by a Gaussian function with a full width of half maximum of $b_\omega = 23(\pm 2)^\circ$ [63–65]. From this an upper limit of $\sigma = 10^\circ$ can be estimated for the mean tilting angle of the crystallographic axes of the grains.

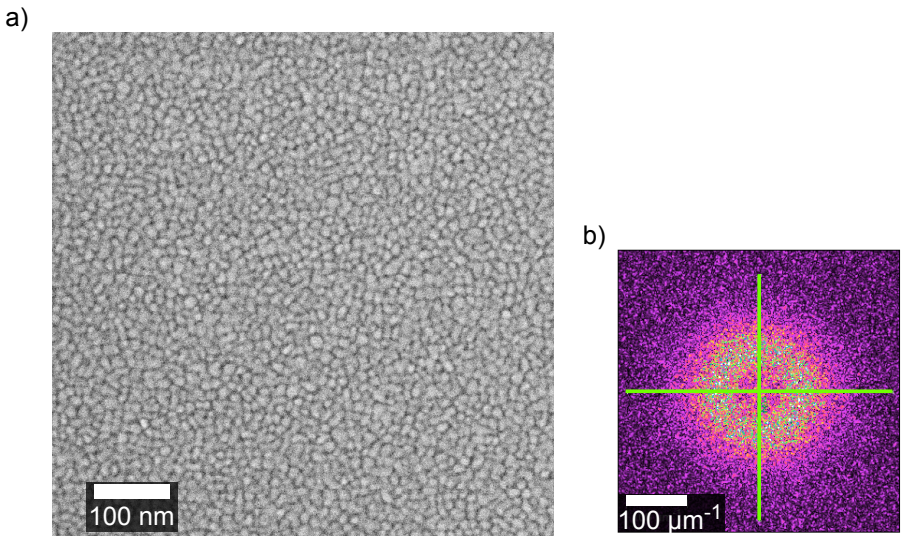

fig 3.1 a) SEM micrograph of a polycrystalline Pt(5 + 1 nm)/Co(50 nm)/Pt(3 nm) film on a SiO_2 substrate. The grains become only visible for thick enough Co layers. b) Fourier transformation of a). A profile in x and y direction is measured, resulting in a average lateral grain size of 16 nm

[4]SEM: scanning electron microscopy

3.2 Fabrication of nanodots and Hall bar

Additive UV-lithography and two steps of subtractive e-beam lithograph (EBL) are employed to structure nanodots and Hall-bars from the layered Co/Pt films. As a first step, larger gold pads are added via UV-lithography and lift off to facilitate electric contacting of the Hall bars by ultrasonic bonding (see also fig 3.3). A detailed description can be found in [90, 113]. These gold pads also serve as markers for orientation in the first EBL step.
After the gold pads the first EBL step is applied which will produce the nanodots. In former years micelles were used to structure dots, however EBL is a much more controlled process to receive only one dot in the crossing area of the Hall bars. For EBL an chemical enhanced e-beam resist[5] is applied. Dots are then written in an SEM which produce shadow mask for the nanodots after the development. The dots are written in a square pattern with a distance of 200 nm.

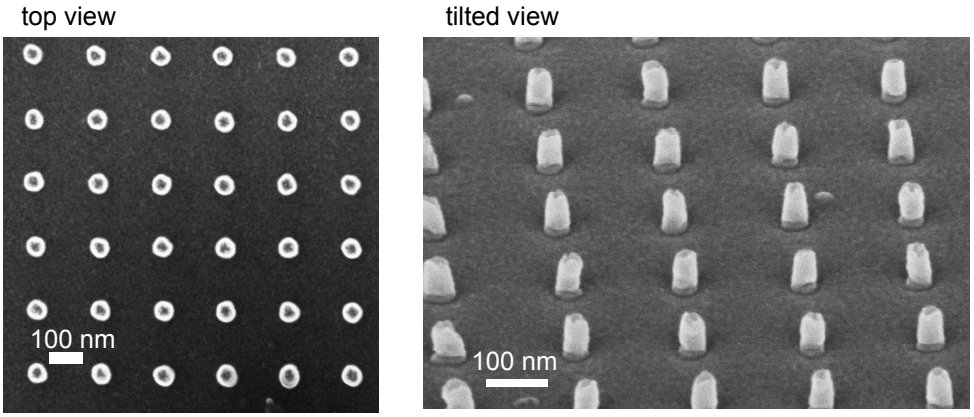

fig 3.2 SEM micrographs of a nanodot array after removing the film around the dots with Ar ion etching at 150 V. The etching was stopped in the Pt seed layer. Top view (on the left), the dots appear bright due to edge contrast. Tilted view (left side) of the same sample, the residual resist (bright, truncated cones) is visible on top of the nanodots (darker ellipse on the bottom of the truncated cones).

For the first time in our group a dot size of 30 nm could be achieved by e-beam lithography through the usage of diluted e-beam resist which has a nominal resolution of 80 nm [6].
The sample is then exposed to soft argon ion plasma etching in a Kaufman

[5] AR-N 7700.08 from Allresist GmbH
[6] from data sheet of Allresist GmbH

source [114] with an acceleration voltage of 150 V, which removes the Pt/Co/Pt wherever the film is not covered by the shadow masks. The etching is stopped after removing 1 nm of the bottom Pt-layer. A SEM micrograph of a nanodot array after the first etching step is shown in fig 3.2. On the left a top view of the dots is shown. On the right a tilted view is shown, here the residual resist on top of the nanodots is visible.
In the second step the Hall bars are structured from the remaining Pt-layer by e-beam lithography. The same resist as for the nanodots is used here, or PMMA[7] which can serve as a negative resist when a high electron dose is applied.

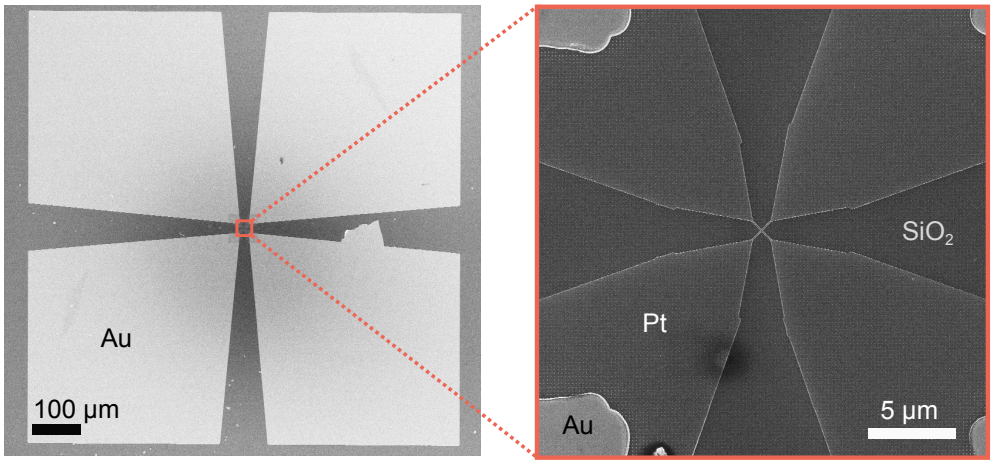

fig 3.3 Overview on the sample design. The bright areas on the left are the gold pads fabricated by additive photo lithography. The zoom (on the right) shows the Hall bar between the gold pads. The very small dots in the array can be seen in the electronic version only (depending on the screen and zoom Moiré pattern might appear)

The advantage of PMMA is, that the residual resist after the fabrication can be easily removed by oxygen plasma. However a higher temperature (160 °C) has to be applied while processing, which might affect the magnetic properties. The drawback of the chemical enhanced negative resist (AR-N 77000.08) is, that it has to be removed by permonosulfuric acid in the end, since it appears to be conducting. A short treatment seems not to affect the dots. Special markers produced with the dots are used with an alignment by the software to find the right position for the Hall bars. After exposure and development the remaining Pt is removed with argon ion plasma etching (500 V). An example of the final nanodot sample is shown in fig 3.3. More detailed recipes can be found in the PhD theses of Thönnißen, Staeck and Neumann [52, 90, 115].

[7] AR-P631.02 from Allresist GmbH

3.3 Measurement setup

All Hall measurements were done in a superconducting magnet[8] with the possibility to apply fields up to 6 T and variable temperatures between 2 K and 290 K with a temperature stability below 5 mK. The sample rod can be rotated which can be used to apply the magnetic field in different directions. The accuracy is approximately 1°.
Care must be taken when applying very small magnetic fields (≤ 20 mT): the field direction and strength is not accurate due to flux trapping in the superconducting ceramic material (NbTi) of the coils [116].
The Hall cross lies in the xy-plane and the sample normal is parallel to the z-axis. A current, (usually 40 µA) is applied to one lead of the Hall cross of the sample with a high precision current source with very low noise [9]. The (transversal) Hall voltage is measured with a nanovoltmeter[10]. The measured signal of the AHE is proportional to the M_z component of the dot (see 2.2.2). Also the longitudinal voltage is measured, though with less accuracy and therefore no anisotropic magnetoresistance (AMR) effects can be observed. But still this gives information about thermal drift and the change of the resistivity with temperature. A detailed discussion of the measurement procedure can be found in [61]

3.4 Residual resistivity ratio (RRR)

A convenient measure to characterize the structural order of the samples is a comparison of the resistivity at room temperature (295 K) and at liquid helium temperature (4.2 K). At room temperature mainly three effects contribute to the resistivity: phonons, magnons and static defects. Phonons and magnons are thermal excitations and therefore suppressed at liquid helium temperature. The residual resistivity ratio (RRR) describes the ratio of dynamic (phonons and magnons) vs. static (defects, disorder) scattering [117] and is defined as:

$$RRR = \frac{\rho_{T=295\,\mathrm{K}}}{\rho_{T=4.2\,\mathrm{K}}} \tag{3.1}$$

The RRR can be also interpreted as a measure for the purity of a sample [117]. In our case it is more a indication for structural order for example grain boundaries.

[8] Spectromag, Oxford Instruments
[9] 6221 current source Keithley
[10] 2182A nanovoltmeter Keithley

It was shown in a previous PhD thesis by Kobs [65] that for our thicker Pt/Co/Pt films the RRR is higher than for thinner films. This means that on the one hand, scattering at the interfaces is enhanced in thinner films and magnon and phonon scattering is reduced. He found $RRR = 1.28$ for samples with $t_{Co} = 2\,\text{nm}$ and $RRR = 1.5$ for samples with $t_{Co} = 20\,\text{nm}$.
However his film composition differs from the samples in this thesis in terms of the seed layer. The samples of Kobs have a seed layer of $t_{\text{Pt}}^{\text{ECR}} = 4\,\text{nm}$ and another magnetron DC layer of $t_{\text{Pt}}^{\text{DC}} = 1\,\text{nm}$ for better interfaces. In the cases of nanodots an even lower RRR is expected since most scattering happens in the very thin Pt seed layer of the Hall bars and only to a little extend in the nanodots where the geometry is also confined. The thickness of the Hall bars is 1 nm smaller than in the seed layer (see table 3.1). If the thickness of the structure is smaller than the grain size of the polycrystalline material, the scattering is dominated by the interface [118]. For epitaxial films much higher ($\gg 1$) RRR values are reported [119, 120].
In fig 3.4 a typical resistance over temperature measurement is shown. The curve is linear for higher temperatures and at lower temperatures ($< 100\,\text{K}$) the slope becomes different due to the reduction of phonons (and magnons).
The RRR values found for the samples in this thesis are shown in tab 3.1. Indeed the RRR value becomes higher with increasing Pt seed layer (and thus thickness of the Hall bar) and a little higher for the ensemble case where the width of the Hall bar is much wider (3 µm compared to $\sim 80\,\text{nm}$).

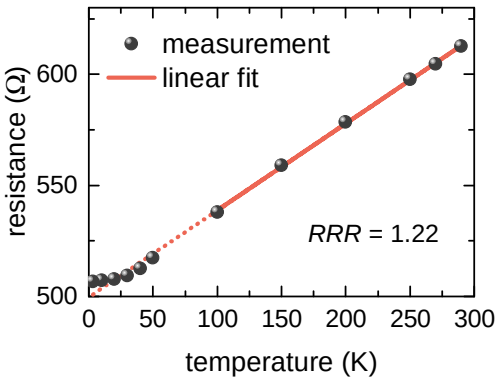

fig 3.4 Resistance over temperature for the ensemble of double layer nanodots discussed in chapt. 4.2. A linear fit (solid red line) is applied for higher temperatures. At lower temperatures ($< 100\,\text{K}$) the resistivity change is not linear anymore. For the residual resistivity ratio $RRR = 1.22$ is received. The measurements were done with an applied current of 400 µA.

composition, thickness (nm)	**diameter** (nm)	**RRR**	**chapt.**
Pt(6+1)/Co(1)/Pt(3)	35	1.21	4.1
Pt(4+3)/Co(0.8)/Pt(3)/Co(1)/Pt(3), ensemble	38	1.22	4.2
Pt(6+1)/Co(1)/Pt(3) (same film as first)	35	1.21	5.1
Pt(6+4.6)/Co(1.4)/Pt(3)	60	1.26	5.1

tab 3.1 RRR values of the nanodot samples in this thesis. For some of the samples the resistance at 295 K was extrapolated from measurements at lower temperatures.

4 Dots with quasi-coherent rotation of magnetization

Nanodots with different diameters and cobalt thicknesses were investigated. In this chapter results of dots with (quasi) coherent rotation of magnetization will be shown and than discussed. The term quasi-coherent rotation[1] is used here, since the switching behavior appears coherent at first glance. Later on in in chapter 5.2 simulations, which include the granular character of the Co dots, will show that in fact it is possible that the magnetization is clearly non-coherent during the reversal, but the overall character of the process is very close to coherent reversal. These simulated hysteresis curves appear to be also very similar to the experimental results.
First, a dot with a $t_{\mathrm{Co}} = 1\,\mathrm{nm}$ thick Co layer and a diameter of 35 nm is introduced. In the second part an ensemble of nanodots with a double Co layer will be presented.

4.1 Single layer nanodot

At first results of the nanodot with a magnetic field perpendicular to the film plane (same as the plane defined by the Hall cross) are shown. The temperature dependence of the switching field is investigated and is compared to the Sharrock model. Later the magnetic field is applied in other angles and the switching field is compared to the Stoner-Wohlfarth (SW) model. In all experiments a current of 40 µA is applied. It was assumed that the easy axis of magnetization of the nanodot is perpendicular to the film plane[2].
A single hysteresis loop at 2 K with the magnetic field applied perpendicularly to the film plane can be seen in fig 4.1 a). The hysteresis shows a typically squared shape very similar to what is expected from the SW model. At ±75 mT all

[1] The term quasi-coherent rotation is used also in literature with meanings that are all subtly different, but have in common that a magnetization reversal which is close to coherent or coherent-like is described [121–123].
[2] Results later on in this section and section 4.1.2 will show that this assumption is not true, however for the first experiments we assume an ideal SW system.

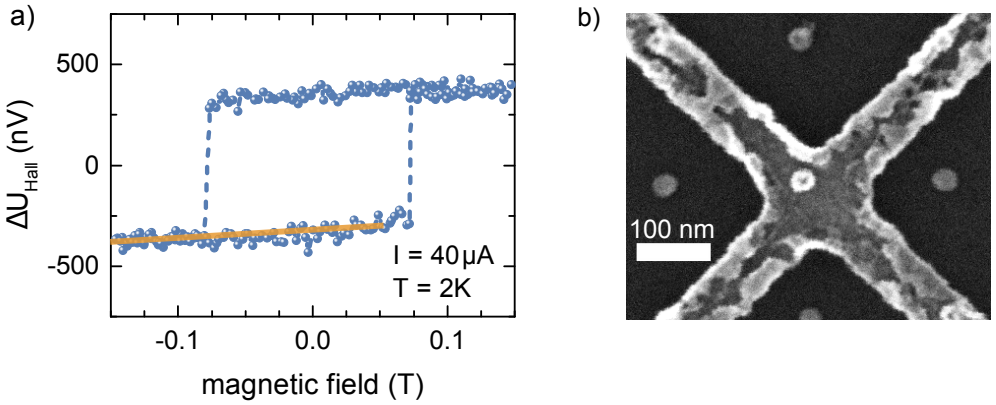

fig 4.1 a) Single hysteresis loop of a nanodot with a Co thickness of $t_{\mathrm{Co}} = 1\,\mathrm{nm}$ and a diameter of 35 nm at 2 K with a current of 40 µA. The magnetic field is sweeped with a rate of $0.1\,\mathrm{T\,min^{-1}}$. At ±75 mT all magnetic moments switch together acting as a single macrospin. The magnetization reversal is referred to also as a jump in the hysteresis and marked here with dashed lines, that are guides to the eye only. An additional slope is marked in orange and probably caused by rotation of the magnetization. b) SEM micrograph of the Hall bar with the dot after fabrication with e-beam lithography.

magnetic moments switch together acting as a single macrospin.

Above 75 mT and below −75 mT the magnetization is (almost) saturated. An additional slope (here marked in orange) can be observed which could be easily mistaken as the normal Hall voltage of the Pt in the leads. However the sign of the normal Hall voltage of Pt and Co would be the opposite of the AHE voltage of Co [93]. (see also section 2.2.2).

The origin of this slope will be addressed again. In fig 4.2 a) a hysteresis curve at 270 K is shown. Here much higher fields are applied, as before in direction perpendicular to the film plane. For this temperature and sweep rate ($0.5\,\mathrm{T\,min^{-1}}$) the dot appears to be in the superparamagnetic state. The hysteresis curve is zero at zero field, because the magnetization fluctuates very fast between near zero field between two states due to thermal activation. Thus the averaged AHE signal over time becomes zero. At higher fields the magnetization is stabilized in direction of the applied field.

A negative constant slope can be observed in the signal for very high fields. This slope is caused by the normal Hall effect of the Pt Hall bar and the Co nanodot. The normal Hall voltage is fitted (in dark blue) and then extrapolated to zero (dotted lines). The NHE constant from the fit is $(2.6 \pm 0.1) \times 10^{-11}\,\mathrm{m^3/(As)}$, which is a little higher than expected for pure Pt (especially ultrathin films [65, 93]), but also the the NHE signal from the Co nanodot with a higher NHE constant has to be considered.

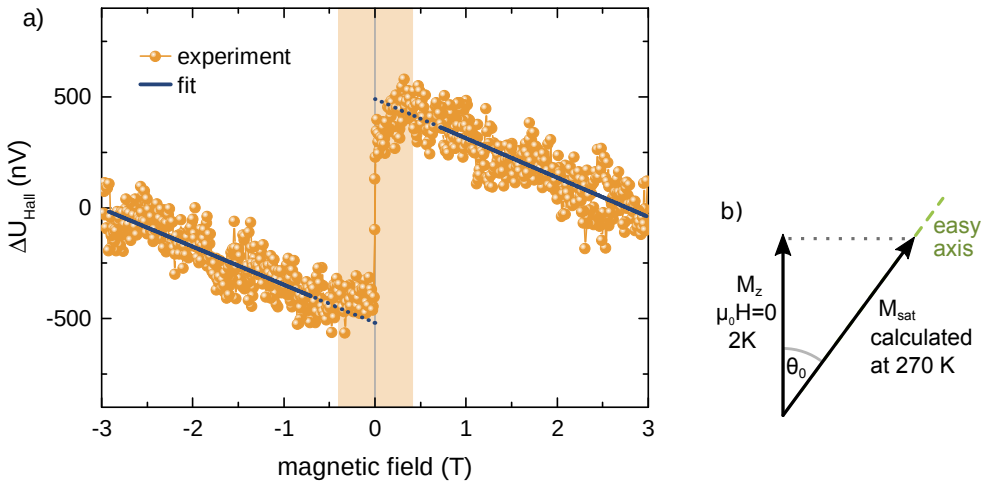

fig 4.2 a) Hysteresis curve (single measurement) at 270 K (solid lines in experimental data are guides to the eye only). The dot is already in superparamagnetic state. The sweep rate is 0.4 T min^{-1}. In dark blue the fit represents the normal Hall effect. The dotted line is an extrapolation to zero. In the orange shaded area ($\pm$0.4 T) the M_z component is reduced compared to fields above $\pm$0.4 T. The M_z component is smaller for lower fields. Considering the normal Hall effect the signal should increase. The observed decrease is typical for a rotation of the magnetization from a tilted easy axis into the field direction (with increasing fields). The magnetization is fully aligned with the magnetic field at approximately $\pm$0.4 T. Another signal change due to the thermally induced switching of the magnetization is expected only at fields between $-$20 mT and 20 mT. This occurs when the magnetic field is very low and the thermal energy high enough to allow the magnetization to fluctuate. The measured time average of the magnetization follows a modified Langevin function and is reduced for low fields (see also for more details [115]). This effect is not visible in the shown measurement since the sweep rate is high and the field resolution very low. b) Sketch of the rotated magnetization without external magnetic field. From the measurement of M_z and M_{sat} the easy axis tilt θ_0 can be deduced.

Below 0.4 T the hysteresis curves deviates from a straight line, here rotation of the magnetization starts since the easy axis of magnetization is tilted. Another experiment showing the tilt will be discussed in section 4.1.2 and simulation that verify the influence of the tilt on the hysteresis are presented in chapter 5.2.2 and 5.3.

Only for fields between 20 mT and -20 mT another change in the signal is caused by the thermally activated switching of the superparamagnetic nanodot. This effect occurs when the magnetic field is very low and the thermal energy high enough to allow the magnetization to fluctuate. The measured time average of

the magnetization follows then a modified Langevin function and is reduced for low fields (see also for more details in the PhD thesis of P. Staeck [115]). This change is not visible in the high field measurement shown in 4.2 however, because of too fast sweeping of the magnetic field and not enough data points. The superparamagnetic contribution of the nanodots is not present at low temperatures. Going back to fig 4.1 a), the slope can be explained probably by the rotation of the magnetization too, since the easy axis and the applied field direction are not collinear. In section 4.2.4 it will be shown that background signals from contamination in the Pt current leads can influence the signal at low temperatures as well. This might also be the case for this measurement.

From the hysteresis curves of fig 4.1 a) and 4.2 a) one can already estimate the tilting angle of the easy axis. This is done in the following way: The signal of the entirely with the magnetic field (in z direction) aligned magnetization (M_{sat}) is compared with the signal of the magnetization at zero field where the magnetization points in easy axis direction. The signal at zero field is reduced, if the easy axis direction is not collinear with the z-axis, since only the projection of $\vec{M}$ on the z direction is measured by the anomalous Hall effect. The extrapolation of the normal Hall voltage to zero field in fig 4.2 a) gives the signal height corresponding to M_{sat}: $\Delta U^{M_{\mathrm{sat}}} = (505 \pm 25)\,\mathrm{nV}$. Since the magnetization fluctuates without magnetic field for this measurement at 270 K, the low temperature hysteresis curve in fig 4.1 a) is used to determine M_z. The signal height is $\Delta U^{M_z} = (345 \pm 10)\,\mathrm{nV}$ at zero field. With simple trigonometry the tilting angle θ_0 of the easy axis can be then calculated (see fig 4.2 b)): $\theta_0 = \arccos(\frac{M_z}{M_{\mathrm{sat}}}) \approx (47 \pm 3)^\circ$.
There are two assumptions made to receive to this result: first, the signal height for the saturated magnetization is constant for all temperatures. This is equivalent to a constant anomalous Hall constant and a constant saturation magnetization. It was found that the anomalous Hall constant increases with temperature for thicker film systems of our group with $t_{\mathrm{Co}} = 2$, 6 and 20 nm [65] however the temperature dependence became less pronounced for the thinner sample. Other studies also found an increase [124]. The exact values and dependency depends strongly on the scattering of the electrons and therefore on growth and quality of the magnetic material [95]. In the next section it will be shown that for an approximation of the tilting angle the assumption of an almost with temperature stable Hall constant is indeed sufficient for this specific nanodot.
The second assumption is that the saturation magnetization stays constant for temperatures up to 270 K. This is certainly the case for bulk cobalt with a Curie

temperature of $T_C = 1385 - 1394\,\mathrm{K}$ [125–127] but for ultrathin layers of Co with a reduced Curie temperature also a reduced saturation magnetization is found [128–130]. However the findings strongly depend on the sample systems, probably the structural properties of the samples[3]. For the rough estimation of the easy axis direction here and also for all other experiments within this thesis small changes of up to 5% in the saturation magnetization are still in the error margins and not relevant. A good summary for the thickness dependence of M_S and T_C in literature can be found in the PhD thesis of J. Wagner [133].
Another point that has to be considered is, that the easy axis direction might change with temperature. This is actually the case and will be shown in section 4.1.2, which follows after the next section dealing with the temperature dependence of the switching field.

4.1.1 Temperature dependence of the coercive field

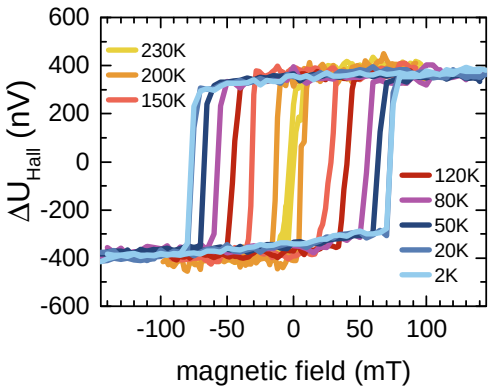

fig 4.3 Hysteresis curves of nanodot with $t_{Co} = 1\,\mathrm{nm}$ and a diameter of 35 nm. Each curve is an average of several (3-10) measurements. For higher temperatures noise is more pronounced. The coercive fields increase for decreasing temperatures. The AHE signal decreases slightly with lower temperatures. At 200 K a small step near 10 mT is visible in the curve due to the thermal broadening the dot switches at different fields for each measurement. In the averaged curve this broadening becomes sometimes visible as a step, but no step can be found in the individual hysteresis curve. At 230 K still a small opening can be observed, however in the individual curves (not shown here) the magnetization fluctuates strongly for low fields.

[3] As was found only very recently, actually the interdiffusive layer at the interface between Co and Pt influences the saturation magnetization at different temperatures [131, 132]. An alloy with gradual change in Co and Pt concentration forms. For the parts of the interdiffusive layer with lower Co concentration the Curie temperatures is reduced. Therefore at lower temperatures more Co atoms contribute to the total magnetic moment and therefore the saturation magnetization increases.

Hysteresis curves as in the previous section were also measured for a wide temperature range. They are shown in fig 4.3. For each temperature several loops were averaged in order to compensate for statistics in the thermally induced switching process. As expected from theory the coercive field increases with decreasing temperatures. The amplitude of the Hall signal decreases also slightly. From this measurement it is however not possible to deduce the temperature dependence of the anomalous Hall constant. Measurements with magnetic fields up to saturation (also of the background at low temperatures) are required for a detailed evaluation and a thorough background correction has to be done.
A plot of the coercive field over temperature gives the following diagram (fig 4.4):

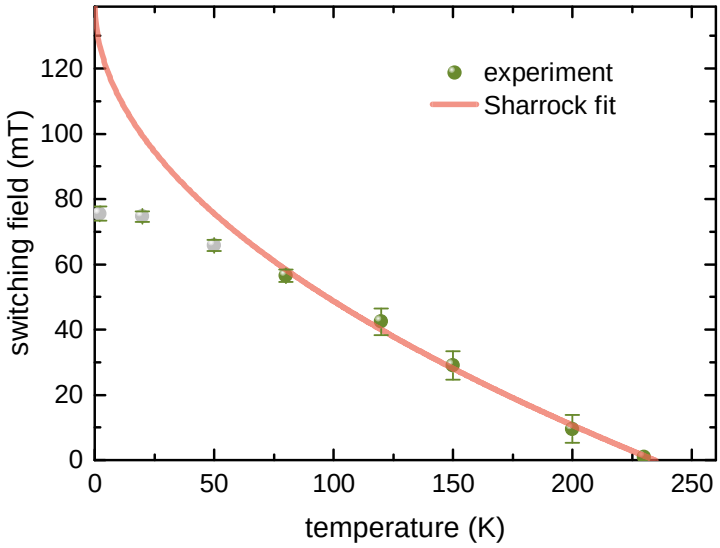

fig 4.4 Coercive fields of the hysteresis loops in fig 4.3 over temperature. For values above 70 K (green) a equation after Sharrock (eq. 2.12) can be fitted. The results are for the anisotropy constant $K = (102 \pm 4)\,\mathrm{kJ/m^3}$ and $T_B = (234 \pm 5)\,\mathrm{K}$ for the blocking temperature. Below 70 K (grey) the coercivity increases much slower with decreasing temperature.

Fitting according to the Sharrock equation (eq. 2.12) was done. However only temperatures above 70 K are included (green symbols) since the switching fields increase much slower than predicted by the model for temperatures below (gray symbols). The resulting anisotropy constant from the fit is $K = (102 \pm 4)\,\mathrm{kJ/m^3}$ and the blocking temperature $T_B = (234 \pm 5)\,\mathrm{K}$, which corresponds also to the previous finding from the hysteresis curves, that the nanodot appears to be in the superparamagnetic state at 230 K. The advantage of the Sharrock fit over a fit according to Garg is here, that fewer fitting variables are used and thus the

variables are truly independent. Furthermore no assumption regarding the attempt frequency f_0 has to be made, which cannot be verified within the experiments shown here. Apart from that the magnetic moment of the dot or the active magnetic volume, that can be obtained from the Garg model, are not discussed here.

Very similar behavior was found also by previous work in our group [52, 90, 134]. The discrepancy varies from nanostructure to nanostructure. For some nanostructures the increase of the coercive field becomes slower already at 60 K for other the deviations start only at 20 K and other again do not show this behavior at all. Several reasons can be discussed for the slower increase of the switching field with decreasing temperatures:

First quantum tunneling of magnetization would cause a similar effect, however temperatures are at least one or maybe even two orders of magnitude too high (> 1 K) for structures of the size of $10 - 100$ nm. [135–139]

Another reason suggested is Bose-Einstein condensation of magnons [140, 141], which causes a small increase of the saturation magnetization with lower temperatures. The increased saturation magnetization then increases the shape anisotropy, which results in a decrease of total anisotropy and therefore switching field. The temperature dependence range $10 - 20$ K they found for their Co/Pt samples, corresponds to our temperature range. It was not possible to verify this theory within our experiments.

On the other hand the slower increase (and in some cases even a decrease) is also found for various films and materials [142–145]. Another possible reason could be contamination with magnetic material that becomes magnetic at very low temperatures. Also recently it was found in our group that an interdiffusive layer at the interface contributes more with increasing temperatures [132]. This results in a change of the anisotropy with temperature and is the topic of the PhD thesis of S. Freercks [131].

All in all the system is very complex and more detailed and sophisticated experiments would be necessary to conclude what the actual origins are. Also a combination of several reasons might be possible.

4.1.2 Angular dependence of coercive field

Hysteresis curves were measured also for different directions of the applied magnetic field at 2 K and 80 K. In the first part of this section the dependence of the coercive field on the applied field angle is discussed and in the second part the shape of

the resulting astroids. Repeating the experiment in all three planes can be finally used to calculate the direction of the easy axis in 3D space.

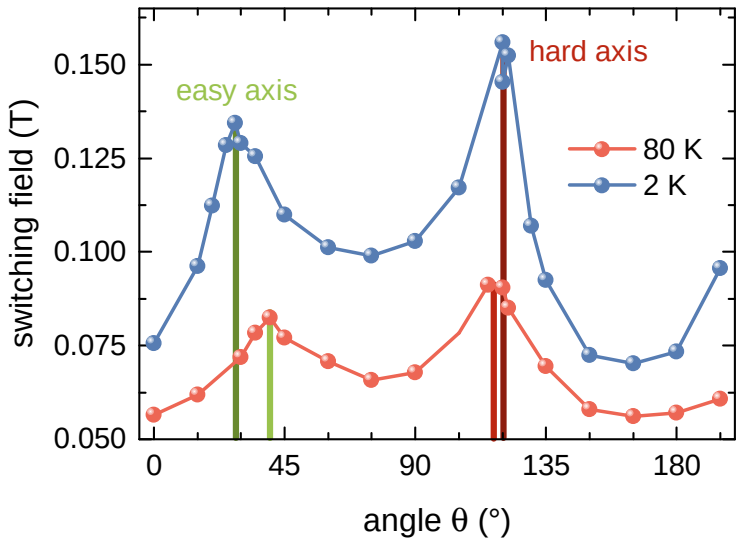

fig 4.5 Coercive fields of the nanodot in fig 4.1 against applied field angle at 2 K and 80 K. The easy axis at 2 K lies at 28° and the hard axis at 120°. The easy axis is shifted at 80 K to 40° and the hard axis to 117°. (Lines connecting the data points are only straight connections for better visibility.)

The dependence of the coercive field on the direction of the applied field is shown in fig 4.5. Typically two maxima can be expected (see section 2.1.2), which are 90° apart according to the SW model. They are shifted from the 0° and 90° position which is attributed to a tilt of the sample's easy axis away from the SW model. Both maxima should have the same value but the easy axis direction has a lower value for both temperatures. This difference cannot be attributed to the fact that the maxima are not hit accurately by choosing to large steps for the angles of the magnetic field in the experiment. This could be in principle the case, since the slope becomes very high near the maxima and small inaccuracy could have a large effect. However, a smaller maximum along the easy axis direction was observed in the work by Neumann [90], Thönnißen [52] and Staeck [115] too.
Also in literature a lower maximum in the easy axis direction is reported for an ensemble of iron particles [146, 147] and other systems [54, 148]. Theoretical calculation give indication that a second order anisotropy constant could be the origin of the lower maximum in easy axis direction than in the hard axis direction [149, 150].

For the 80 K measurement the amplitude between minimum and maximum is smaller than in the 2 K case. Additionally the easy axis of magnetization for 2 K is shifted for the 80 K measurement by 10° while the hard axis almost stays the same. As the maxima, both minima between the hard and easy axis should have the same values in an ideal SW system.
All this features can be qualitatively attributed to the tilt of the easy axis in the system as explained by Staeck [115] (p.80, fig 4). Shape anisotropy and magnetocrystalline anisotropy axis are not perpendicular to each other anymore in this case. This results in a deviation from the 90° symmetry of the two maxima for easy and hard axis. However in the calculations by Staeck the width of the minimum valley and maximum hill is roughly the same, in the experiment such behavior was not observed. It appeared always that the minimum valley is much broader and in this aspect more similar to the ideal SW system.

Switching field astroid

The astroid of the switching fields can be deduced from the angular dependence of the switching field as measured in fig 4.5. The corresponding B_z and B_x components of the switching field can be calculated from the switching field $|B|$ by simple trigonometry:

$$B_z = |B| \cos\theta \qquad \text{and} \qquad B_x = |B| \sin\theta \tag{4.1}$$

B_z can be than plotted over B_x and a shape similar to an astroid is observed[4]. Besides the shift in the easy axis for different temperatures which were observed already in the previous section also a change in the astroid's shape is observed.

For 80 K both sides of the astroid seem very straight, they resemble more a parallelogram than the geometrical definition of an astroid. Similar results are reported also by Jamet et al. [151] and Vouille et al. [152]. For 2 K the astroid has one straight and one curved flank. Similar behavior was also observed by Bonet et al. [55] and [131].

However, if the anisotropy is constant one would expect only a shrinking of the astroid. Since the shape of the astroid changes, it can be concluded that at

[4] From theory of a perfect SW particle a perfect astroid is expected (see also 2.1.2). In most experimental cases this is however distorted. Even though this is not entirely mathematically correct this distorted curve is still referred to as an astroid.

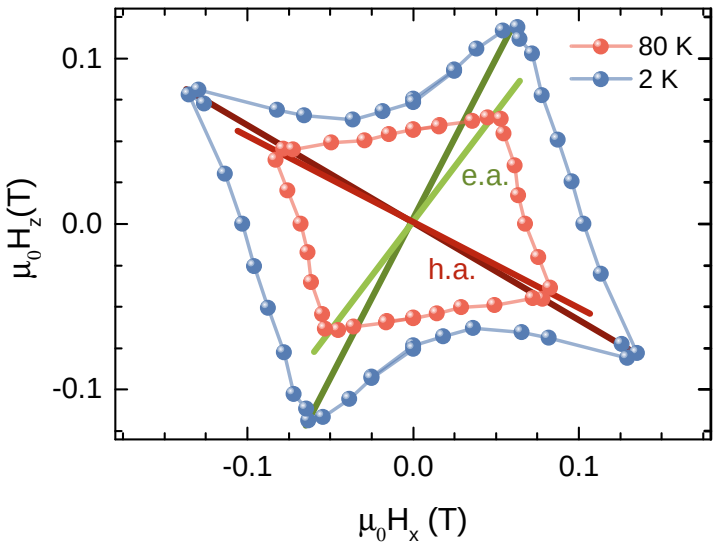

fig 4.6 Astroids of fig 4.5 for 2 K and 80 K. In dark (2 K) and light (80 K) green the easy axis is indicated. The angle of the easy axis changes with temperature. The hard plane (or projected on 2D the hard axis) is indicated in dark (2 K) and lighter (80 K) red, the change of the hard plane is less pronounced. Lines connecting the data points are only straight connections of points for better visibility.

least one of the different contributions (shape, magnetocrystalline or surface) to the effective anisotropy changes with temperature. This temperature dependent contribution is most likely also responsible for the change of the angle of hard and easy axis with temperature in a system with a tilted easy axis.

Calculation of the 3D tilt of the easy axis

The same measurement of the switching field over angle of the applied field at 2 K was repeated in the two other perpendicular planes of space (yz-plane referred to as 90° rotated out-of-plane measurement and xy-plane, which corresponds to the film plane, referred to as in-plane). The resulting three astroids are shown in fig 4.7 and together in 3D in fig 4.8. They are strongly distorted. The out-of-plane (yellow) and in-plane (red) astroid should intersect at one point in the (x,0,0) direction, this point is defined as 'A'. For the 90° rotated out-of-plane astroid (green) and the in-plane (red) the intersection should be in (0,y,0) direction (Point B) and for the out-of-plane (yellow) and the rotated out-of-plane (green) astroid in (0,0,z) direction (point C). (The same applies for -A,-B and -C)

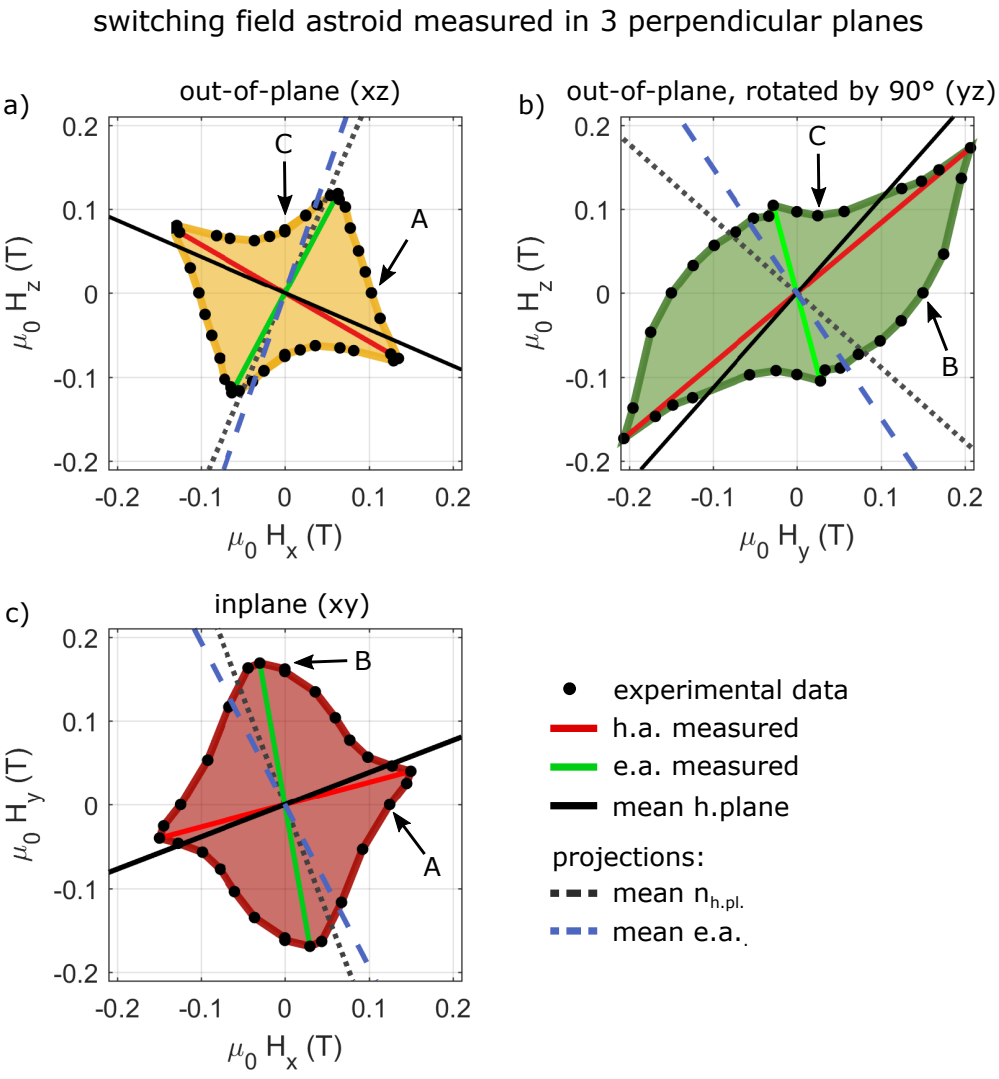

fig 4.7 Switching field astroids measured in 3 perpendicular planes (xz=oop, yz=oop, rotated by 90° and xy=in-plane). The measurements were done at 3 K. a) is the same measurement as shown in 4.6.

However, the astroids do not fit together. The deviations are shown in tab 4.1 and are between 22 mT and 10 mT.

There are several possible reasons for these differences. The first reason is a slight misalignment in the experimental setup. This is very likely but cannot be the only reason. The second reason is that the first measurement (out-of-plane astroid) was done several weeks before the second. By passing a current of 40 µA for many hours through such a small structure certain changes appear. These changes might be stronger at the beginning and smaller after many hours. Also between

intersection point	difference in switching fields
A	22 mT
B	10 mT
C	21 mT

tab 4.1 Difference of the switching fields at the intersections points of the astroids (also shown in 4.7).

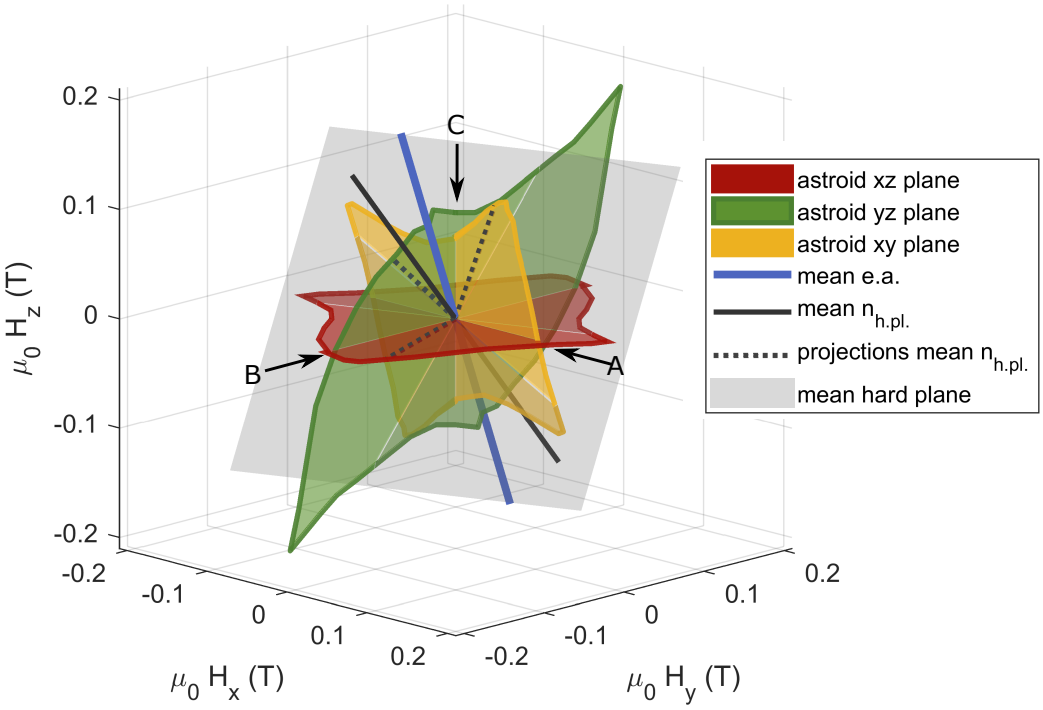

fig 4.8 Measurements, shown in fig 4.7, put together in 3 dimensions. The plane normal is shown as a solid black line.

each measurement the sample has to be removed from the cryostat and great care (and precautions) has to be taken to not destroy it by electrostatic discharge. Probably the crystalline structure of the dot was slightly altered here due to Joule heating by small electrostatic discharge current. In a future experiment those measurement would need to be repeated in a save environment of a 3D vector magnet, where the sample mounting does not need to be changed.
These changes could also alter the easy axis and hard plane directions. But it

is still worth to determine a mean easy axis and hard plane to get an idea of the typical tilting of the anisotropy axis in such a nanodot. Therefore for each astroid the hard axis (intersection of the astroid with the actual hard plane) was determined as described in the previous section. With two h.a. vectors the hard plane can be spanned, the third h.a. vector should then lie in this plane. This is not the case in the results of the measurements presented here. In fact with the three h.a. vectors 3 different hard planes can be received. Reasons for this could be inaccuracy of the setup. However the deviations are too strong to be an inaccuracy only. It is more likely that the predictions of SW model are not applicable for this type of nanodots. This argument is also supported by the fact that the astroids are strongly distorted.
For each hard plane a normal vector can be calculated by $n_{1,2}^{\text{h.plane}} = \frac{v1 \times v2}{|v1 \times v2|}$ (with v_i vectors within the hard planes). From theses 3 normal vectors a mean normal $n_{\text{h.plane}}$ vector is calculated which defines the mean hard plane as an approximation. The angle of $n_{\text{h.plane}}$ with the z-axis is $\theta = 50°$ and $\phi = -69°$ with the x-axis. The resulting mean hard plane can be seen in fig 4.8 (light gray). It becomes clear that the hard plane is strongly tilted from the film plane (= xy-plane). Also the angles between the three hard planes can be calculated through the $\phi_i = \arccos(\frac{n_i \cdot n_j}{|n_i||n_j}$). The angles are shown in table tab 4.2.

astroids defining the hard planes		**angle between**
1st plane	**2nd plane**	$\mathbf{n_{i,j}^{h.pl.}}$
(xz,xy)	(xz,yz)	26°
(xz,xy)	(yz,xy)	25°
(xz,yz)	(yz,xy)	14°

tab 4.2 Angles between the three hard planes found in the measurements.

Likewise a mean easy axis vector can be determined from the 3 easy axis vectors measured in each plane. It is tilted at $\theta = 37°$ from the film plane normal (=z-axis) and $\phi = -63°$ away from the x-axis. Even if we assumed a tilted SW astroid, the easy axis vector and the normal vector of the hard plane should have the same direction. However in our case they have an angle of $\psi = 14°$ between each other. This deviation cannot be entirely explained by inaccuracy of the setup. Together with the fact that 3 different hard planes can be calculated and that the astroids are severely distorted, it gives strong indication that the assumption of coherent rotation of macroscopic magnetization as described by the SW model is indeed not sufficient for this nanodot.

In conclusion it is very important to measure the switching field astroid also in 3D, since only in this way deviations from the SW model can be detected and the switching behavior better understood. The reason for this deviations are the grains of the polycrystalline material the nanodot is made of. A detailed discussion on this topic will be given in chapter 5.

4.2 Ensemble of double layer nanodots

An ensemble of nanodots with a double layer of Co separated by Pt was investigated. The thickness of the Pt middle layer was chosen to be 3 nm to avoid interlayer exchange coupling [65]. The magnetically active Co layers have different thicknesses in order to receive different anisotropies and thus different switching fields. Both layers are expected to exhibit an out-of-plane easy axis. The detailed composition is: Pt 7 nm/Co 0.8 nm/Pt 3 nm/Co 1 nm/Pt 3 nm. The first Pt layer consists of 4 nm fabricated by ECR magnetron sputtering in order to provide good texture, the rest is fabricated by DC magnetron sputtering for smoother interfaces. The top Pt layer serves as a protection for Co oxidation (see also chapter 3 for preparation details).
An SEM image is displayed in fig 4.9. In the crossing area of the Hall bars an ensemble of 240 nanodots can be found. The width of the cross is 3 µm which results in a filling factor of 10%. However, also dots in the legs of the Hall cross contribute to a certain extend to the Hall signal (compare [90, 113, 153, 154] for sensitivity maps of Hall crosses).
In the first part of the section measurements with a magnetic field perpendicular to the sample plane will be shown. In the second part results from measurements with in-plane magnetic fields will be discussed. It will be shown that another signal due to the planar Hall effect contributes to the transversal voltage detected and (super)paramagnetic background influences appear for low temperatures.

4.2.1 Switching fields in out-of-plane ensemble measurements

For measurements with a magnetic field applied perpendicularly to the film plane (out-of-plane) the hysteresis curves depicted in fig 4.10 a) were received. The measurements were done at different temperatures between 3 K and 250 K. Coming from negative field values the signal changes first linearly, than at at $10 - 300$ mT another signal change in positive direction appears. It is not a sudden jump as for individual nanodots. This increase is caused by anomalous Hall effect due to switching of the magnetization of the ensemble of nanodots. Since the nanodots of the ensemble all switch at different fields a more gradual change in the hysteresis curve instead of a defined jump is observed. The switching fields become higher for smaller temperatures. Additionally different slopes are visible in the high field regime. These slopes will be discussed later on in section 4.2.4.
In order to evaluate the mean switching field of the ensemble the derivative of the magnetization regarding the magnetic field was calculated and a Gaussian

function was fitted for both forward and backward branch of the hysteresis curve. As an example the derivative of the 3 K measurement is shown in 4.10 b). The positions of the maxima then give the mean switching field. Any constant additional slope in the hysteresis curve results only in an constant offset in the derivative and is therefore not corrected. In principal the standard deviation of the Gaussian fit σ gives the switching field distribution of the nanodot ensemble. Beside the thermally induced switching field distribution also other reasons have to be considered. It has to be kept in mind that the easy axis of magnetization of at least some of the nanodots can be tilted. Hence the magnetization starts to rotate towards the easy axis direction near zero magnetic field as found also in simulations in sect. 5.2.2 and 5.3. This rotation also contributes to the derivative

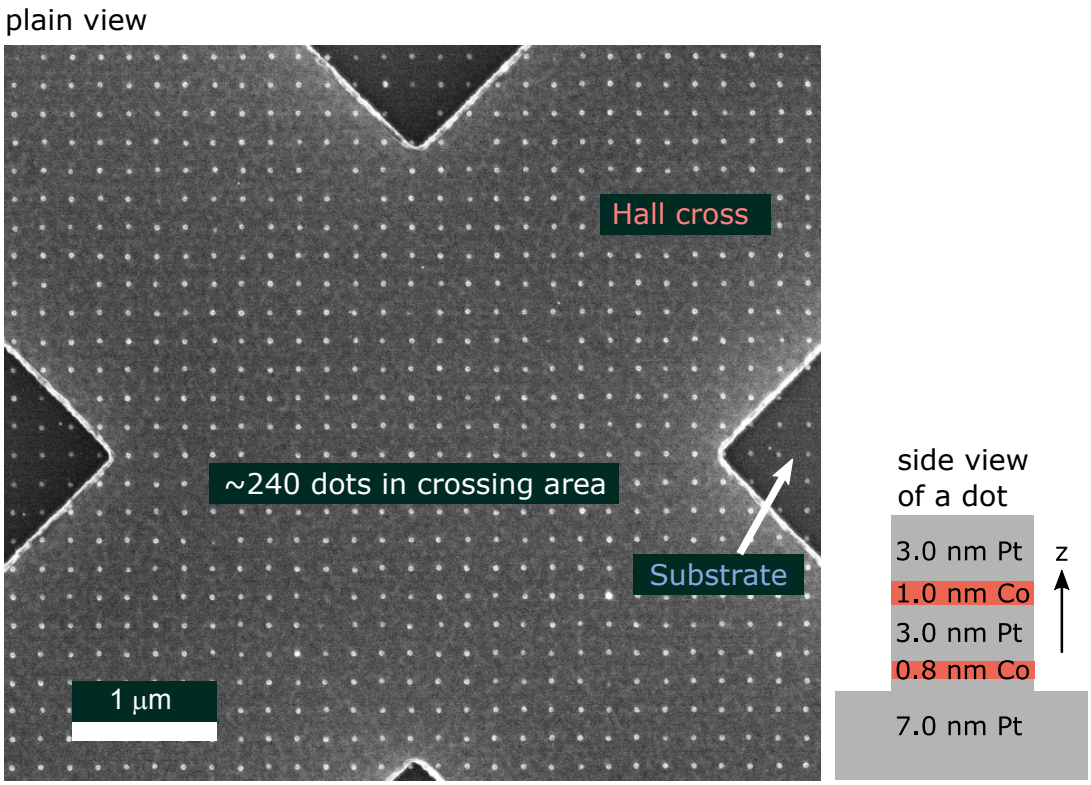

fig 4.9 SEM picture of ensemble sample with double layer nanodots (Pt 7 nm/Co 0.8 nm/Pt 3 nm/Co 1 nm/Pt 3 nm). The width of the cross is 3 µm. Ca. 240 nanodots can be found in the crossing area. The filling factor of the nanodots is 10%. However also dots in the legs of the cross contribute to the Hall signal [90, 113, 153, 154]. A current of 400 µA was applied to two opposite legs of the Hall cross. The dots have a mean radius of (18.80 ± 1.35) nm. On the right side a sketch of the side view with the composition is shown. This sketch is not to scale.

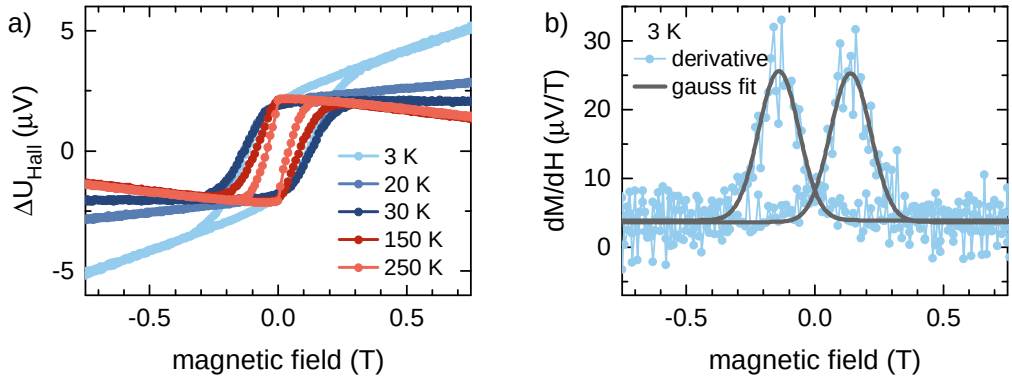

fig 4.10 a) Hysteresis curves for different temperatures with the magnetic field applied perpendicularly to the film plane. In order to evaluate the average switching field and account for the different background signals, the derivative of the magnetization was calculated. In b) the 3 K derivative is shown as an example. Then a gauss function $f(x) = y_0 + \frac{A}{\sqrt{2\pi\sigma^2}} \exp(-\frac{(x-x_0)^2}{2\sigma^2})$ was fitted for the backward and forward branch of the hysteresis curve. The maxima represent the average switching field. The offset in b) is caused by the linear background, visible in a).

and results in an additional increase before zero field. Otherwise one would assume that some of the dots switch already at small fields with the wrong sign, which in principle could be the case for strongly incoherent switching as can be seen in the hysteresis curves of section 5.3.4. But the rotation seems to be more likely. For the measurement at 250 K it was not possible to apply a Gaussian fit. The shape of the derivative was different, probably since some of dots were already in the superparamagnetic state at this temperature.

For all temperatures only one maximum for forward and one for the backward part of the hysteresis loop is found. This indicates that either both layers of the nanodots switch at the same field and therefore are still coupled (either ferromagnetically or from stray field) or that the switching fields for layers with the nominal same properties have such a wide distribution for the different nanodots that it becomes impossible to distinguish top and bottom layer.

The switching fields deduced from the derivative of the hysteresis curves are depicted over the temperature in fig 4.11. The switching fields decrease with increasing temperatures, above 50 K almost linearly, below 50 K the slope becomes steeper. The standard deviation σ of the fitted Gaussian function is depicted as gray shading. In principle 68% of the dots should switch within this area, however since also rotation of the magnetization contributes to the derivative of the hysteresis this value is probably much lower. Half of the width of the Gaussian

fit over temperature is shown in fig 4.12. It decreases for higher temperatures, this is rather unexpected and not observed in other systems [136, 155]. An explanation could be the size distribution of the nanodots and also the fact that the dots consist of two different layers of magnetic material. This aspect will be discussed in detail in sect. 4.2.2. It becomes clear that the nanodots in the ensemble have a wide variation of switching fields and therefore also anisotropies and blocking temperatures. A Sharrock fit (eq. 2.12) can be fitted to the data.

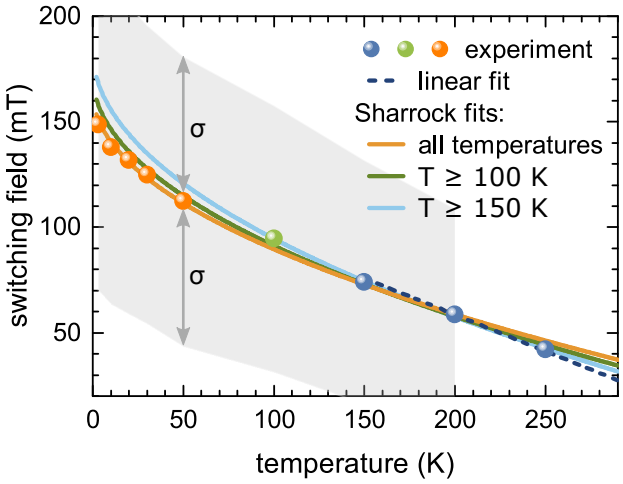

fig 4.11 Mean switching fields extracted from the derivative for different temperatures (balls). The standard deviation is depicted as gray shading, 68% of the dots switch within this area. For 250 K it was not possible to apply a Gaussian fit to the derivative. A Sharrock fit can describe the temperature dependence of the switching field. Here three different fits are shown, first with all temperatures (orange), however the quality of the fit is not very good for high temperatures. The second fit includes only data points ≥ 100 K (green) and the third data points ≥ 150 K (blue). The results of the fits are shown in table 4.3. The more of the lower temperatures are included in the fit, the higher gets the blocking temperature and the lower the anisotropy. From linear fit only including points with ≥ 150 K a blocking temperature of $T_B = 369$ K is received.

Three different data subsets are used for three different Sharrock fits in the diagram and also a linear fit to the data points with $T \geq 150$ K to approximate the blocking temperature. The linear fit gives $T_B = 369$ K. For the first Sharrock fit all temperatures are included (orange). For the second fit only temperatures below or equal 100 K are considered (green) and for the third only data points with ≥ 150 K (blue). The results of the Sharrock fits are shown in table 4.3. The more data points with low temperature are left out, the lower the blocking temperature gets and the higher the anisotropy. In general it is always observed

points included in Sharrock fit	**anisotropy** (kJ/m^3)	**blocking temperature** (K)
all temperatures	120 ±11	485 ±60
T ≥ 100 K	125 ±7	453 ±30
T ≥ 150 K	134 ±2	423 ±7
linear fit, T ≥ 150 K	-	369

tab 4.3 Anisotropies and blocking temperatures from different Sharrock fits and a linear fit in fig 4.11.

that the switching fields for low temperatures lie below the values expected from theory. This is also here the case if only data points of high temperatures are taken into account. The errors in anisotropy and blocking temperature become worse the more points are included. This can be attributed to the fact that the model assumed for the switching field is not consistent over all temperatures. There are several reasons for this. First it was found already from previous work that the anisotropy is not constant over temperature for films [65] and also for the nanodots [131, 132, 134]. More relevant in the case of the ensemble might be that for higher temperatures some of the nanodots are superparamagnetic (especially since the ensemble has a wide SFD) and only the dots with a higher anisotropy contribute. Another factor is that the easy axis of the nanodots is tilted which is not accounted for in the model and furthermore that the switching process might be incoherent to a certain extend as will be discussed by micromagnetic simulations in chapter 5.

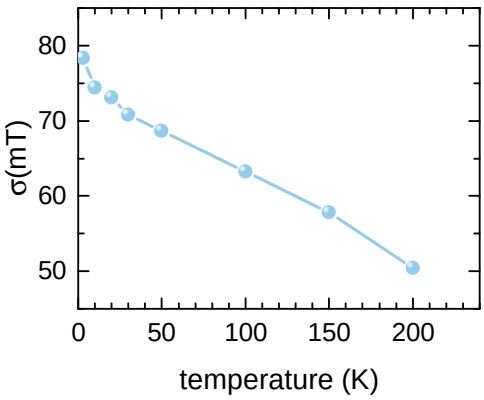

fig 4.12 The width of switching field distributions (2σ) increases with lower temperatures.

4.2.2 Influence of the size distribution on the switching field distribution (SFD)

In principle the two layers of the nanodots should switch separately, since the 0.8 nm thick Co bottom layer has a different anisotropy than the 1 nm thick top layer and exchange coupling between both layers should vanish across the 3 nm thick Pt layer between top and bottom layer. It was therefore expected that the separate switching events are visible in the hysteresis curve or in the switching field distribution. As no separate switching is observed in the hysteresis curves and the measured switching field distributions appear very broad, the influence of the size distribution of the ensemble of nanodots is discussed in the following.
From an SEM micrograph the size distribution of the nanodots can be deduced. The size distribution of 803 nanodots present on the cross (many of them also in the legs of the cross, not visible in fig 4.9) is shown in fig 4.13 a). The mean radius is (18.80 ± 1.35) nm. This size and therefore volume distribution gives different switching fields. This contributes additionally to the usual thermal switching field distribution (SFD) of an otherwise totally uniform ensemble of nanodots.
In order to calculate the influence of the size distribution, an ensemble of 10 000 nanodots with the measured size distribution was assumed. Then for each nanodot the SFD was calculated after eq. 2.19 using Mathematica and all SFDs summed and normalized[5].
In this calculation also the distribution of anisotropy constants was considered due to a distribution of shape anisotropies after Millev et al. [69], also caused by the size distribution. The result of this calculation is presented in fig 4.14. The calculation was done for a nanodot with 1 nm Co thickness and 0.8 nm thickness. The effective anisotropy constants were taken from MOKE measurements of other films with the corresponding thicknesses. The used parameters are $K_{\mathrm{eff}}^{\mathrm{film},\,0.8\mathrm{nm}} = 300\,\mathrm{kJ/m^3}$ measured by S. Freercks [131] and $K_{\mathrm{eff}}^{\mathrm{film},\,1\mathrm{nm}} = 90\,\mathrm{kJ/m^3}$ from P. Staeck [115].
The calculated switching field distributions are shown for 3 K and 300 K with blue and yellow solid lines. For 3 K the maxima of both SFDs are ~ 250 mT apart. Half of the width ($= \sigma$) is 7 mT and 10 mT for the thin and the thick layer[6]. For higher temperatures the position of the maxima move to lower fields and are still ~ 150 mT apart (width 16 mT and 8 mT for thin and thick layer). Additionally

[5] We assume a constant f_0 since the sweep rates in the experiments are rather slow ($\sim 0.1\,\mathrm{mT\,s^{-1}}$) and it was shown that for slow rates all models give the same results [90, 92].

[6] σ is calculated by FWHM $= 2\sqrt{2\ln 2}\sigma$, assuming a normal distribution instead of the calculated SFD. This is not accurate but gives the possibility to compare the values with the actual measured σ, where a Gaussian function was fitted.

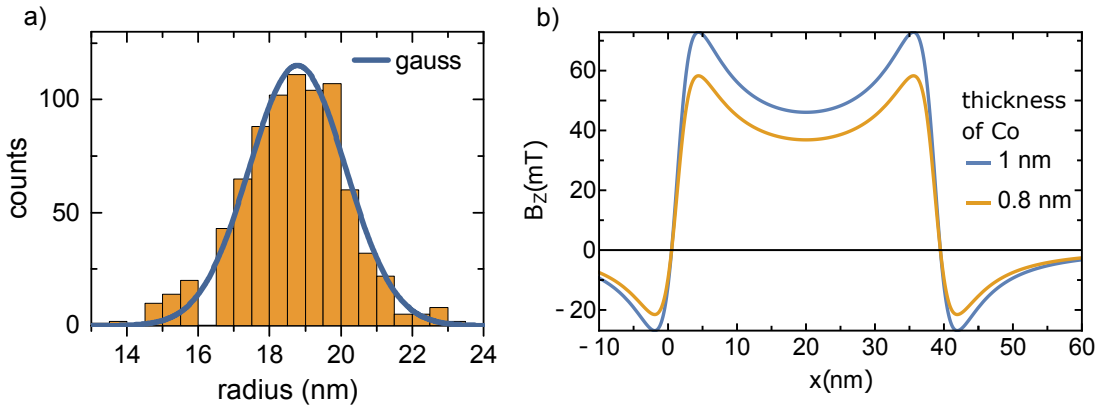

fig 4.13 a) Histogram of the radius of the nanodots as extracted from the SEM image via imageJ. The radius distribution of the nanodots is (18.80 ± 1.35) nm. b) The stray field of the 1 nm and 0.8 nm thick Co layer in a distance of 3 nm is shown.

for comparison the SFD for one individual dot with a radius of $r = 18.8$ nm is shown as a gray curve for both thicknesses. The SFDs for an individual dot are in the center of the size distributed SFDs but much narrower, especially at low temperatures.

As already mentioned since the two Co layers of the dots are separated by a 3 nm

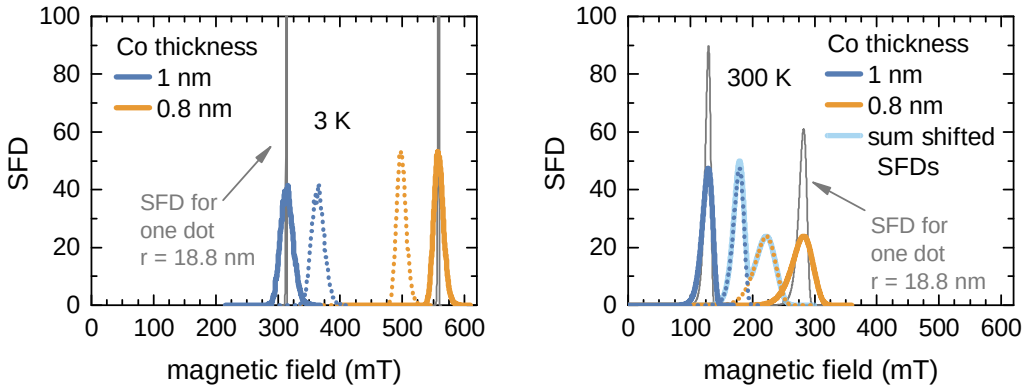

fig 4.14 Calculated switching field distributions (SFDs) for two ensemble of 10 000 nanodots with a 1 nm thick Co layer with $K = 90\,\mathrm{kJ/m^3}$ (blue, solid) and for a 0.8 nm thick Co layer with $K = 300\,\mathrm{kJ/m^3}$ (yellow, solid). In a double layer nanodot both switching fields are shifted by the stray field of the other Co layer, thus the SFD of the thicker layer is shifted by 50 mT and the thinner by 60 mT (as estimated from fig 4.13 b)). The nanodots have a distribution of size as deduced in fig 4.13 a) from SEM measurements. In gray the SFDs for one nanodot with a radius of 18.8 nm is shown. For 3 K both distributions are clearly separated. For 300 K they are slightly overlapping.

thick Pt layer they should be decoupled regarding exchange interaction. However the stray field will still be present and shift the switching fields. The stray fields of both layers at a distance of 3 nm are shown in fig 4.14. An average of $\sim 50\,\mathrm{mT}$ (thinner layer) and $\sim 60\,\mathrm{mT}$ (thicker layer) is assumed. In theory the thicker and magnetically softer layer should switch first. Under the influence of the stray field of the thinner layer the SFD will be shifted by $\sim 50\,\mathrm{mT}$ towards higher fields. As the magnetization of the magnetically harder (here thinner layer) will be in the opposite direction of the external field and the stray field will reduce the effective field at the position of the softer layer. The switching field of the harder layer however will be reduced (by $\sim 60\,\mathrm{mT}$) since the stray field of the already switched layer and the external applied field will add. Both shifted SFDs are shown as dotted lines in fig 4.14.

For the low temperature case still both SFDs of the layers are clearly separated and thus separate switching should appear, while for the higher temperature case a certain overlap appears. But still two separate maxima should be visible (light blue, curve).

If we compare the calculated SFD to the experimental findings in fig 4.10 b) at 3 K, they are clearly different. Only one maximum can be observed. Also a MOKE measurement of another double layer film, fabricated at the same time as the initial film of the dots, shows only one step in the hysteresis curve (see fig 4.15). If one compares the widths of the experimental SFD and the SFD from theoretical calculation, the experimental SFDs are much broader (78 mT) than expected from theory. Most likely the magnetic properties are not as uniform as initially assumed and a local variation gives a much broader SFD.

Similar results were reported by Sun et al. [156]. They also come to the conclusion, that in their system the size distribution is not dominant for the width of the SFD, but the intrinsic anisotropy distribution. Lee et al. [157] find by micromagnetic simulation, that the tilting of the easy axes and a possible anisotropy distribution of their FePtCu dots are the major contributions to the broad SFD. Here the influence of the tilting is even larger than the influence of the anisotropy distribution, while the size distribution only causes a small influence.

Thomson et al. [27] found by simulation that a variation of the anisotropies causes a variation of nucleation fields for their ensembles with larger Co/Pd discs and smaller dots ($\sim l_{\mathrm{ex}}$). They assume that the dots in their measurements switch by nucleation of a small volume, which is the same for all structure sizes, followed by immediate domain wall propagation. Another ensemble of thicker Co/Pt dots with a diameter of 180 nm is studied by Engelen et al. [158]. They also describe

a broad measured SFD and discuss differences in the local switching field and reversal mechanism, but cannot finally pinpoint the origin of their experimental results.

Apart from to the increased width of the SFD, the switching fields are much lower in the experiments shown here, than predicted by the presented model. An explanation for all these deviations might be a variation of the local crystalline structure. This could be a reduced exchange between grains, a distribution of anisotropies in the grains or tilting of the crystalline axes of the grains. All these aspects will be discussed for individual dots in chapter 5.2. Along with structural changes comes a deviation from the model of coherent rotation, which was assumed for the theoretical calculation of the SFDs. It is also possible that the 1 nm thick top layer has slightly different growth properties than when directly grown on a Pt seed layer. This could then also change the anisotropy of the initial film material. Nevertheless the trend of the experiments of a counterintuitive narrower SFDs of the double layer dots with higher temperatures than at lower temperatures, can be reproduced by the theoretical calculations. This trend is caused by the separation of the two maxima in the calculation that becomes smaller with higher temperatures.

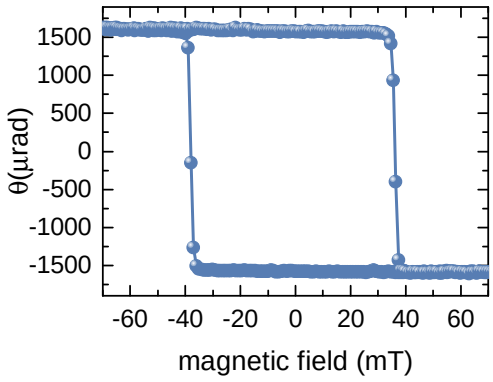

fig 4.15 MOKE measurement of a double layer film. The field is applied perpendicularly to the film plane in the assumed easy axis direction. Sample prepared at the same time as the film of the dot sample. Both layer switch together at the 38 mT.

4.2.3 Individual double layer nanodot

A single nanodot on the same piece of substrate and thus with the same composition and fabrication procedure, was also investigated. The dot has a diameter of 38 nm and thus (almost) the same properties as the ensemble. For this dot also only one

jump in the hysteresis curves could be observed (see fig 4.16 a)). However for very low temperature at 3 K another feature appeared that might be caused by the 1 nm thick and softer layer (see fig 4.16 b)).
The signal heights at zero field for both temperatures are almost the same. The additional feature in the hysteresis curve at 3 K has approximately 1/3 of the total signal height, it appears to be more of a contineous change than a defined jump (also in the single measured loops).

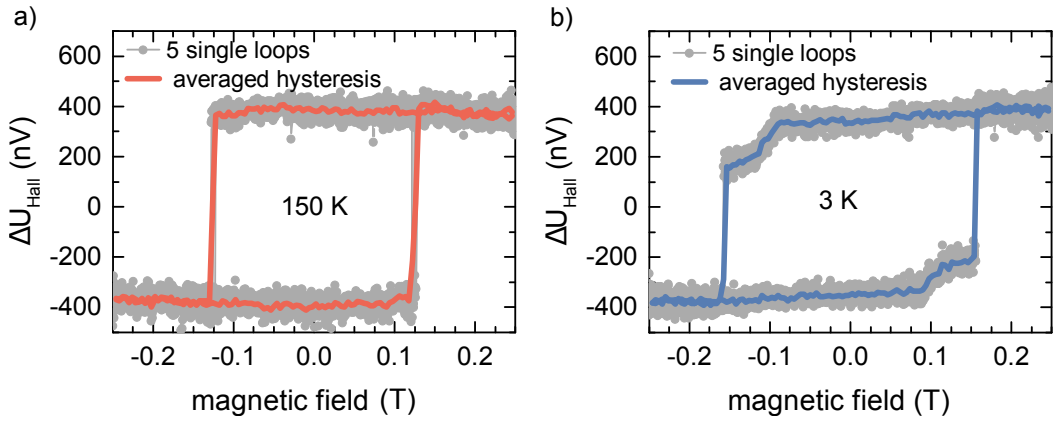

fig 4.16 Hystersis curves of a single nanodot with a Co double layer, with the same properties as the ensemble, fabricated at the same time on the same piece of substrate. For 150 K only one jump can be observed. For 3 K another feature appears which might be caused by the magnetically soft layer. This feature is not a separate jump however.

This additional feature was not visible in the ensemble of nanodots. It would be necessary to measure more double layer dots to verify if this can be observed also in other dots and to decide if it is caused by the second layer or a property of this individual dot. For single layer nanodots such a hysteresis curve was never found. Double layer nanodots with a 1.4 nm thick top layer (not shown here) exhibited a complicated temperature dependent coupling behavior and for some temperatures separate switching. These results could not be explained so far [52, 159]. It was suspected that the thick top layer had a strongly tilted easy axis of magnetization and therefore complicated coupling with the thinner bottom layer. Therefore these type of double layer nanodots with a very thick top layer were not investigated further.

4.2.4 (Super)paramagnetic background in the out-of-plane measurements

In the following section the high field slopes of the hysteresis curves of the double layer ensemble are discussed.
In fig 4.10 a) for 250 K (light red) a negative slope for the high field part is observed. This slope is caused by the normal Hall effect in Pt (negative sign of normal Hall constant, see section 2.2). The normal Hall signal can be mainly attributed to Pt since there is significantly more Pt in the current leads (Hall cross) than Co in the nanodots (nanodots fill only 10% of the crossing area and also the dots consist more than 75% of Pt).
At 30 K and lower temperatures in fig 4.10 a) a change in the sign of the high field regime's slope is observed. In order to study the origin of this effect another set of measurements with magnetic fields up to 6 T was done. The results can be seen in fig 4.17.

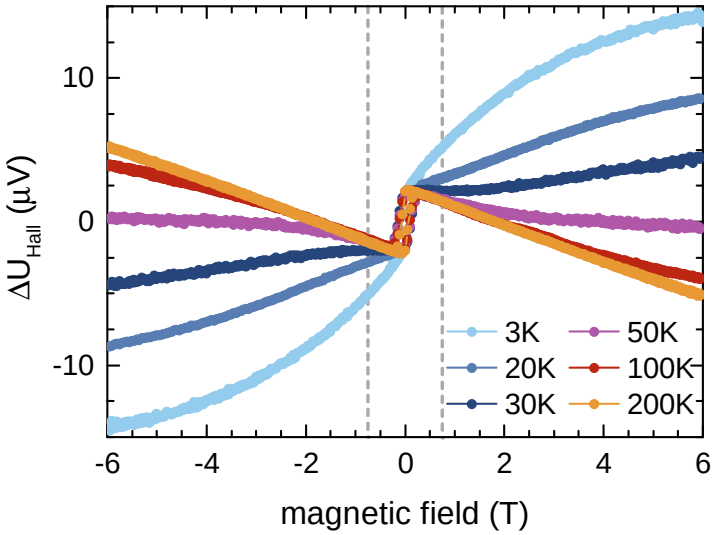

fig 4.17 Hysteresis curves of the double layer ensemble for different temperatures with high magnetic fields up to 6 T applied perpendicularly to the film plane. For temperatures below 100 K a strong (super)paramagnetic background signal occurs. The gray dashed line represents the field range used in the measurement in fig 4.10.

Here it becomes visible that already at 100 K small changes occur above 2 T, which become more significant for temperatures equal or below 50 K. For 3 K a S-shape behavior becomes visible. Comparing this result with previous findings by Neumann [160], the occurrence of the background can be attributed to small

inclusions of one or several Co-Atoms in the Pt material. They become ferromagnetic only below a certain temperature. Since the particles are very small they are not blocked but in the superparamagnetic state. Single Co-Atoms are paramagnetic. Near the Curie temperature they also contribute to the signal of the hysteresis. Both effects causes the typical S-shape [85]. For dilute PtCo alloys the Curie temperature was found to be 39 K for a 2.6 % content of Co and 104 K for 5.2 % of Co [161]. The particles might be of different size with different curie temperatures and also the detailed configuration of the neighbors (or interface configuration) might influence their behavior [162].
It is important to recognize that for the 3 K even at 6 T the (super)paramagnetic background is still not saturated. The origin of this observation is the paramagnetic background. The paramagnetic background is thermally activated and the magnetization of the background aligns with higher fields. Therefore their M_z component increasingly contributes to the Hall signal.
The origin of the background is probably the fabrication of the dots from a Pt/Co/Pt/Co/Pt film. The dots are dry etched with Ar ions and shadow masks produced by e-beam lithography as described before in the chapter 3.2. Stronger etching has already reduced the onset of the (super)paramagnetic background signal compared to previous work [160]. The effect is in this thesis also only visible for this sample. Probably it is enhanced compared to the AHE signal, since the filling factor on the Hall cross is only 10% compared to a filling factor for the single nanodots of 50% or more.
Another influence that cannot entirely be excluded can be magnetic contamination from other materials during the sputtering deposition of the initial films, such as Fe from the sputter chamber.
For the detection of switching fields this (super)paramagnetic background is of minor relevance. For lower magnetic fields ~ 500 mT it gives an almost linear contribution and therefore an offset in the derivative of $M(H)$. If the signal heights are compared, the (super)paramagnetic background has to be considered, especially if one wants to study the temperature dependence of the AHE constant. This applies also for the investigation on the normal Hall effect.
Apart from these more technical aspects, it is not entirely sure if the ferromagnetic material at low temperatures influences the switching behavior of the magnetization of the nanodots.

4.2.5 Planar Hall effect (PHE) contributions to Hall signal of in-plane measurements

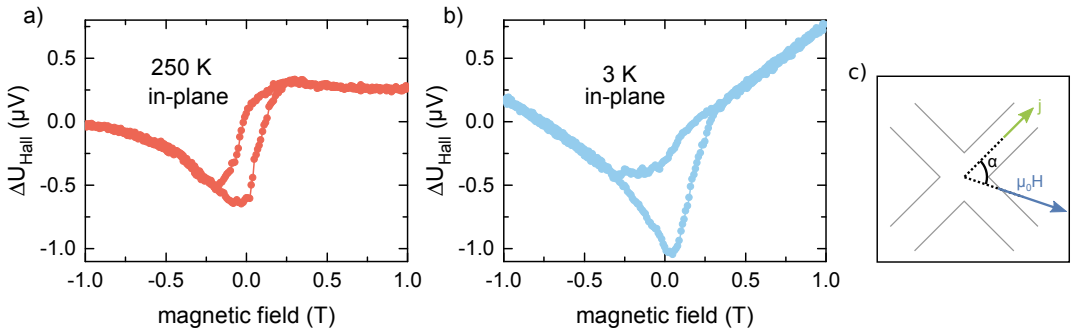

fig 4.18 Hysteresis curves of the ensemble for different temperatures with the magnetic field applied in-plane and with an angle $\alpha = 45°$ towards the current direction. a) At 250 K already differences between backward and forward curve of the hysteresis are visible. b) At 3 K the measured curve does not resemble a hysteresis curve anymore. c) Sketch for the definition of the in-plane angle α.

If the magnetic field was applied in the plane of the ensemble a rather unexpected behavior occurred. In principle the backward and forward part of the hysteresis curves measured by anomalous Hall effect (AHE) are point symmetric with each other as AHE and normal Hall voltages are odd functions of the magnetic field and the magnetization [101][7]. Point symmetry is equivalent to congruence when the curve is rotated by 180° around the symmetry point.
In the measurements, shown in fig 4.18, however forward and backward curves differ from point symmetry for a) 250 K. For the measurement at 3 K, shown in fig 4.18 b), point symmetry seems to disappear entirely. The hysteresis shape can be hardly recognized in the low temperature case and even an axially symmetric contribution to the signal can be observed for magnetic fields above 0.5 T and below −0.5 T.
In order to separate axially and point symmetric signals of forward and backward path of a hysteresis curve, a correction was applied as depicted in fig 4.19.

[7] The generalized resistivity tensor can describe all this magnetoresistance phenomena. A very simple rule applies $\rho_{ik}(H) = \rho_{ki}(-H)$ [163, 164] which is a consequence of the Onsager principle. In simple words it means if the electrons reverse their direction, they follow their former path only if the magnetic field (or magnetization) is also reversed (and dissipation is omitted) [165]. With various symmetry considerations it can be concluded that the AHE and NHE are odd functions of the magnetic field and the magnetization, while the anisotropic magnetoresistance and also the related PHE are even functions in H and M.

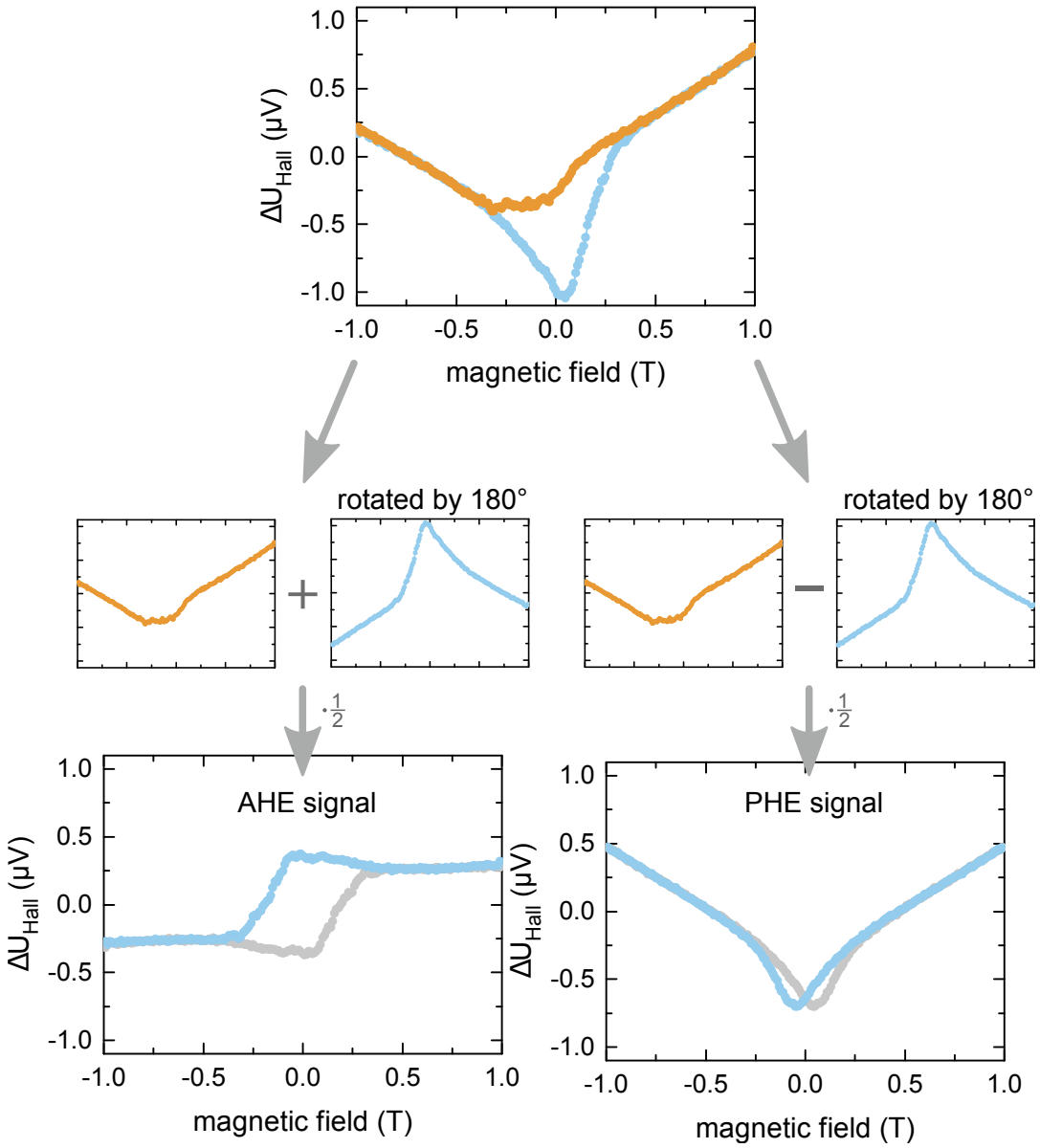

fig 4.19 A correction is applied in order to separate the point symmetric and axially symmetric signal of the forward and backward curves measured with an in-plane magnetic field. The backward branch of the curve (orange) is rotated by 180° and then added to the forward branch. This results in a hysteresis curve with forward and backward path being point symmetric with each other (light blue, bottom left). If the backward branch is subtracted the forward curve is received (light blue, bottom right) which is axially symmetric in the high field regime ($> |0.25\,\mathrm{T}|$). The curves are then mirrored (point or axially) and represent the backward branch of the corrected curves (light gray).

The backward path of the hysteresis curve was rotated by 180° around the axis perpendicular to the paper plane. The average as well as the difference signal between rotated backward and forward part was calculated.
The axially symmetric difference signal corresponds to the magneto resistance effects and the average to the point symmetry of the anomalous and normal Hall effect. In light gray also the towards the point/y-axis mirrored signals are plotted. They represent the backward branch of the curves. The results of the measured data after this correction are shown in fig 4.20 and 4.22. With the correction the hysteresis shape becomes visible also for low temperatures and the even signal can be identified as the Planar Hall effect (PHE section 2.2.3). A more detailed experimental proof that this signal is indeed caused by PHE will be given in section 4.2.6 when the in-plane angle α between applied field and current direction is varied.

Temperature dependence of the in-plane hysteresis curves after PHE correction

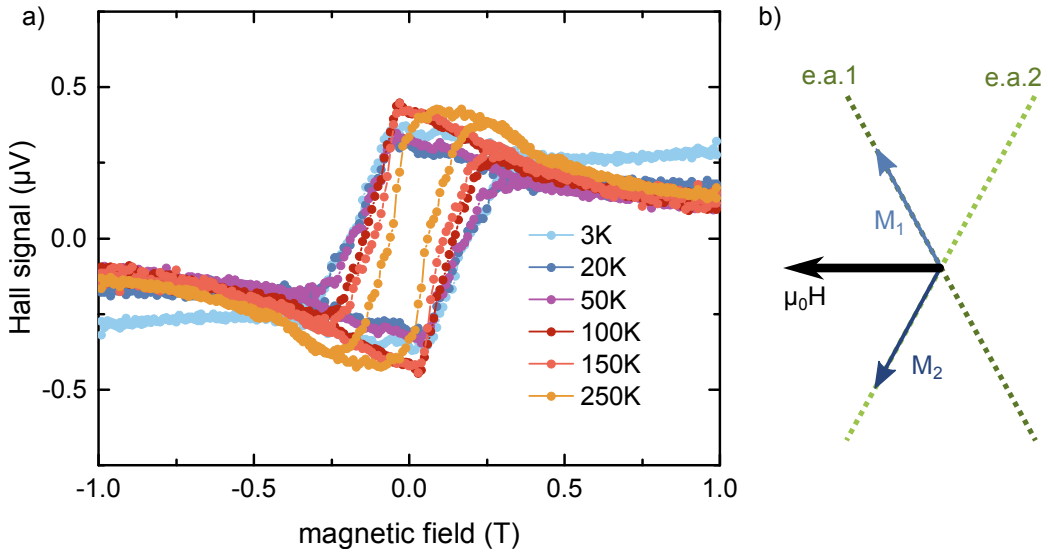

fig 4.20 a) Point symmetric contribution of the signal for different temperatures. They can be interpreted as the AHE signal. The signal is much smaller than in the case of a perpendicular magnetic field (cp fig 4.10a)) since some of nanodots point up and other down and thus their signal cancels out. b) Sketch of projection of the easy axes. Depending on the tilt, in some of the nanodots the magnetization points up or down, when a magnetic in-plane field is applied.

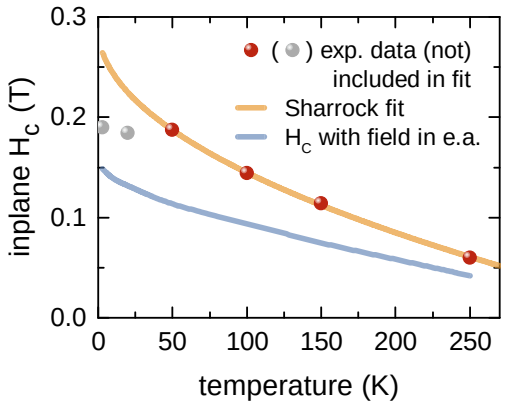

fig 4.21 Switching fields in-plane over temperature. $K = (211 \pm 2)\,\mathrm{kJ}$. $T_B = (400 \pm 6)\,\mathrm{K}$. Grey points are not included in the fit. As a comparison the fit of the data of fig 4.11 for the switching fields in e.a. (out-of-plane) direction are shown.

The results for the corrected hysteresis curves at different temperatures shown in fig 4.20 are discussed in this section in more detail. At 250 K the hysteresis curve has a rounder shape, which is probably caused by some of the dots that are superparamagnetic already. Near 0 T the magnetization of those superparamagnetic dots fluctuates fast and therefore the resulting signal averaged over a certain time becomes zero. These fluctuations might be also enhanced since the magnetic field is applied in-plane direction, which is at least close to the hard axis of of some of the (un)tilted nanodots and thus reduces the energetic barrier. For all temperatures the signal is here about 6 times smaller than when the magnetic field is applied in perpendicular direction. Why this is the case is not entirely clear and needs more verification. One reason could be that some of the nanodots have a $+$ and others a $-z$ component of the magnetization and thus those AHE signals compensate as sketched in fig 4.20 b). Also the maxima in the hysteresis curves which is near 40 mT could be caused by the tilting of the easy axis. When the magnetic field is applied in reverse direction the magnetization of some of the nanodots might rotate towards the z-axis. This case is very complex, since 3 dimensional movement of the magnetization in a tilted system hast to be considered and therefore needs more detailed measurements and calculations. Furthermore another origin could be also misalignment of the applied magnetic field.

The switching fields over temperature are shown in fig 4.21 and a Sharrock fit is applied. For a better comparison the fit of data with the magnetic field applied in

out-of-plane direction (fig 4.11) is also displayed. The switching fields are higher when the magnetic field is applied in in-plane than in out-of-plane direction. Also the increase with lower temperatures is steeper than in the out-of-plane case. As before data at very low temperature is not included in the Sharrock fit. The blocking temperature is 400 K and a little bit lower than in the out-of-plane case. However the anisotropy obtained from the fit is much higher with $K = 211\,\mathrm{kJ/m^3}$ (compare tab 4.3).
For temperatures around 20 K again similar as in the case of (super)paramagnetic background in sec 4.2.4 a different high field behavior appears in the hysteresis curves. In principle the signal should approach zero for very high magnetic fields, since the AHE signal is proportional to the M_z component of the magnetization and the magnetic field is applied in the xy-plane. In saturation however all magnetic moments should be aligned to the field and therefore the z-component of $\mathbf{M}$ becomes zero. This is the case for measurements above 50 K. For 50 K this is still the case, but the approach in the high field regime is slower (not easily visible in the diagram). For 20 K the curves has an almost zero slope and for 3 K it has a non-zero positive slope for high fields.
A first idea could be that as in the out-of-plane measurements (super)paramagnetic background could cause this additional signal. On the other hand this background particles should align in field direction and therefore their magnetization would have no z-component and should not contribute to the AHE signal at high fields. If we consider a certain misalignment of the magnetic field ($H_z \neq 0$) on the other hand, this increase with higher fields could be caused by the gradually alignment of the thermally activated paramagnetic background.

Temperature dependence of the PHE signals

The PHE signals, received from the correction (explained in fig 4.19), are shown in fig 4.22 . For lower temperatures the signals have an increasing higher amplitude than for high temperatures. Regardless the temperature, all curves are almost linear in the high field regime. Linear fits can be applied to this high field regime and the V-shape then subtracted (fig 4.23). The linear high field regime and the low field PHE signal after the V-shape subtraction are discussed in the next two paragraphs.

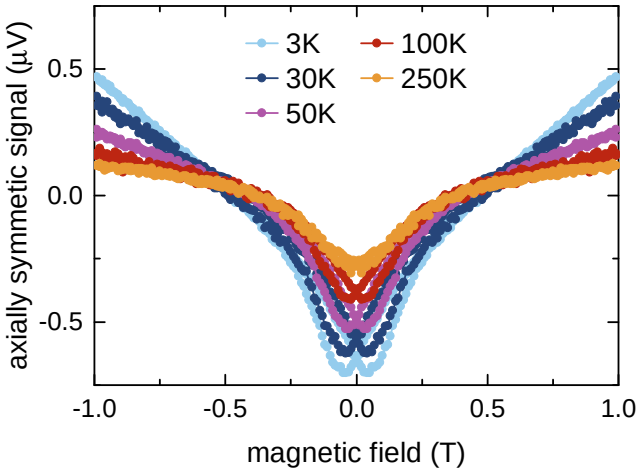

fig 4.22 PHE signal of the ensemble for different temperatures, obtained from the Hall voltage after correction, as explained in fig 4.19.

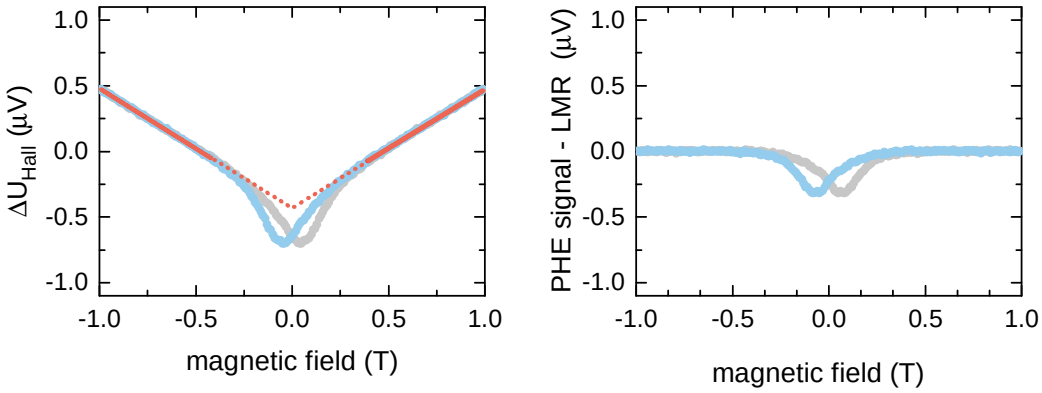

fig 4.23 Subtraction of high field contribution: a) first a linear fit is done for the high field behavior (red solid line). Then a V-shape is subtracted (red solid and dotted line). b) result of correction. The shown example was measured at 3 K.

Low field PHE signal

The resulting signals after subtraction of the V-shape are shown in fig 4.24. They exhibit a minimum close to zero field and the signal saturates for higher applied fields ($\mu_0 H > 0.5\,\mathrm{T}$). The minimum becomes broader with higher temperatures and the exact position moves closer to 0 T. The signal heights change and are displayed in fig .1 in the appendix. A maximum signal height is found for 50 K. Comparison with the Hall signal in fig 4.20 shows that the signal change corresponds to the rotation process of the magnetization of the ensemble of nanodots.

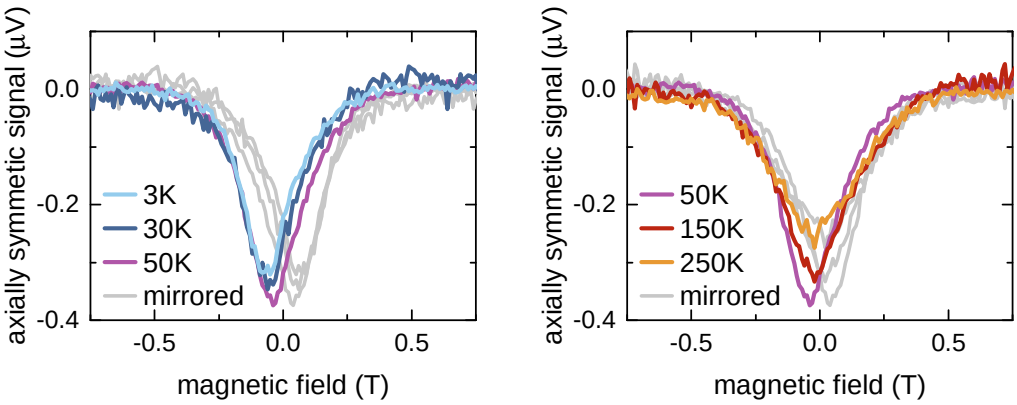

fig 4.24 Axially symmetric signal with subtracted high field contribution. The minima correspond to a maximum alignment parallel or antiparall to z-axis. The PHE is caused by the AMR (and probably AIMR).

From the Hall signal shown in fig 4.20 one can conclude that the magnetization of the nanodots has a certain M_z component at 0 T. It is not fully aligned with the z-axis, since the individual easy axes of the nanodots are tilted from the perfect out-of-plane direction. Some of those dot have a tilted easy axis with an in-plane component that does not point in field direction (compare fig 4.20b)). When a small reversal field is applied the magnetization of some of those dots rotates towards the ± z direction. Some other of those dots may rotate without changing the z-component. Thus the magnetization has a maximum z-component at $\mu_0 H = 40\,\mathrm{mT}$ (for 50 K measurement, the others are shifted slightly to higher or lower values). This corresponds to the minima in the signal of fig 4.24. When more field is applied the magnetization of some dots rotates further to the in-plane direction, other more tilted dots switch, the absolute z-component becomes smaller.

This behavior can be also observed in the longitudinal and transversal resistance of the measurements of Leven et al [166], who measured the longitudinal and transversal magnetoresistance of a single $(\mathrm{Co/Pt})_{10}$ nanowire (width= 110 nm) with out-of-plane anisotropy. When the magnetic field is applied in longitudinal direction, the magnetization rotates from perpendicular to the sample plane to in-plane (in this case longitudinal, that means parallel to the current direction). This is reflected in the longitudinal resistance since the resistance is higher for the moments pointing parallel to the current direction than when they are pointing perpendicular due to the AMR. Kobs showed in his thesis, that an additional effect comes into play when the field is applied in transversal direction (in sample plane,

but perpendicular to the current), the AIMR[8] [65]. From theses measurements and the theory of PHE[9] it can be concluded that the signal shown in fig 4.24 is the difference between longitudinal voltage measured with an applied field and magnetization in longitudinal direction $U_{||}$ and the voltage with applied field and magnetization in transversal direction U_{trans} and that AMR and probably also AIMR play a role here.

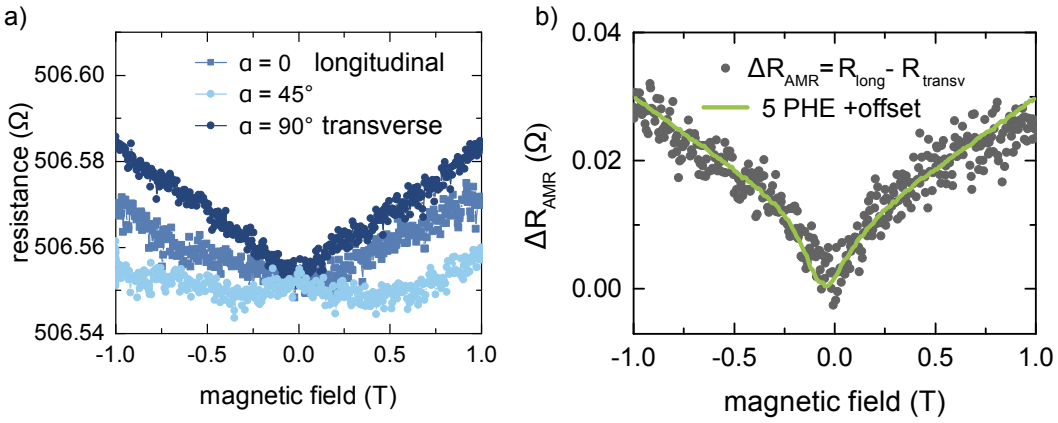

fig 4.25 a) at 3 K longitudinal voltage at 3 different in-plane angles α (angle between applied external field and current $\vec{j}$). In b) the longitudinal resistance measurements for $\alpha = 0°, 90°$ are subtracted. Almost the same signal as in fig 4.22 is received (here shown in green), except of a factor of 5, plus an offset due to different contact resistance in the setup.

Resistivity measurements at 3 K are shown in fig 4.25. $\alpha = 0$ corresponds to the measurements with the magnetic field in current direction (longitudinal) and $\alpha = 90°$ to transversal. The subtraction of both measurements actually corresponds to the PHE measurement, but the PHE signal is a factor of 5 smaller (cp fig 4.25 b)). This can be explained by a close look on the sample design in fig 4.9. For the PHE measurement only dots in the crossing area (or close to the crossing area) of the Hall bar contribute. For the longitudinal resistance signal however also the dots in the current leading bits contribute. Therefore the

[8] Anisotropic interface magnetoresistance. Kobs showed, that the interpretation, that the change in the resistance with a transversally applied field being solely intrinsic domain wall resistance, by Leven et al is actually wrong. Also AIMR gives an additional change in resistance.

[9] $U_{\text{PHE}} = (U_{||} - U_{\text{trans}}) \sin\alpha \cos\alpha$, with $\alpha \sim 45°$ und $\sin\alpha\cos\alpha = \frac{1}{2}$ If the dots are only present in the crossing area of the Hall bar, the proportionality becomes an equality.

resistance signal is much higher. For a new sample a different design would be preferable with dots only in the crossing area of the Hall bar.

High field slope of the PHE signal

While for smaller magnetic fields (250 mT) mainly the change of magnetization in the ensemble of nanodots is responsible for the PHE signal, the high field slope has a different origin. The changes of the high field slope with temperature are shown in fig 4.26. The absolute value of slope of the curves increases for lower temperatures. Most likely the effect is caused by the material of the Hall bars. The filling factor of the nanodots in the ensemble is only 10% but in a sample with an individual nanodot the filling factor is usually 50% or higher. This means that the fraction of the signal coming from the nanodots is lower in the case of the ensemble and here the observed high field PHE effect is much higher than in the samples with an individual nanodot.

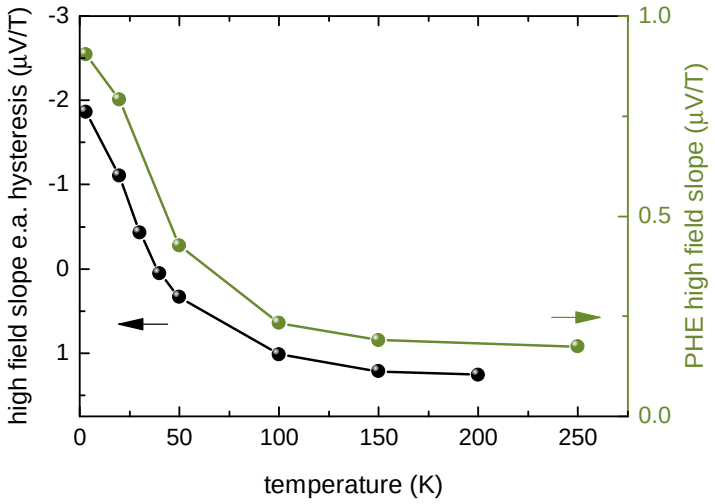

fig 4.26 High field slope of hysteresis curves with field in e.a. direction due to (super)paramagnetic background (black, left y-axis reversed direction) and high field slope of the PHE signal (green, right y-axis) against temperature. Both slopes are almost constant above 100 K and have a strong increase/decrease (black/green). (error bars are very small).

There are several effects that could be the origin of this V-shaped graph which will be discussed in the following:

LMR (Lorentz magneto resistance): The first assumption was that LMR might be the origin. The hypothesis LMR is supported by the fact that the

absolute value of the high field slope of the PHE signal increases with lower temperatures, which corresponds to a larger mean free path of the electrons. The LMR is also anisotropic with the orientation of the magnetic field. In a simple description the LMR is caused by electrons following bent paths in the sample due to the magnetic field and the Lorentz force. The LMR is proportional to B^2 however [167]. LMR is actually observed at 3 K in the longitudinal resistance with a polar magnetic field and in the in-plane ($\alpha = 45°$) measurement in 4.27 a) and b). A function $f(x) = ax^2 + b|x| + c$ can be fitted, where a represents the LMR and c the resistance at zero field. The parameter b gives probably the anisotropic high field contribution that causes the PHE. The results from the fits are:

	a (10^{-7} V/T^2)	**b** (10^{-6} V/T)	**c** (mV)
polar	8.4 ±0.2	8.83 ±0.1	202.67 ±0.1
in-plane, $\alpha = 45°$	20.4 ±0.4	5 ±0.14	203.01±0.01

Unfortunately, no resistance measurements with high fields in longitudinal or transversal direction were done. But from theory, for both directions the LMR contributions have to be different. When the difference is calculated, still a quadratic dependence would result. The observed PHE behavior in fig 4.27 c) however has a clearly linear character also for fields up to 4 T. More experimental data is needed to understand this. The linear contribution, that is represented by the fit parameter b, however is not caused by LMR.

SMR (Spin magneto resistance): SMR would show a linear behavior with the magnetic field. The temperature dependence of the SMR would be opposite to the observed behaviour. The absolute value of the slope of the SMR decreases for lower temperatures, since this effect is caused by electrons being scattered at magnons. However fewer magnons are present at lower temperatures [65, 168]. Also important is that the signal has to be of anisotropic nature in order to appear in the PHE signal. The SMR is in principle isotropic however. One could think maybe of anisotropy caused by the constraint size of the system. But due to the opposite temperature dependence, SMR is most likely not the reason for the high field PHE contribution.

Superparamagnetic background: It is very likely that the (super)paramagnetic background in the Hall bar plays a major role. The reason can be explained by fig 4.26. Here the high field slope in the PHE signal (in green, right

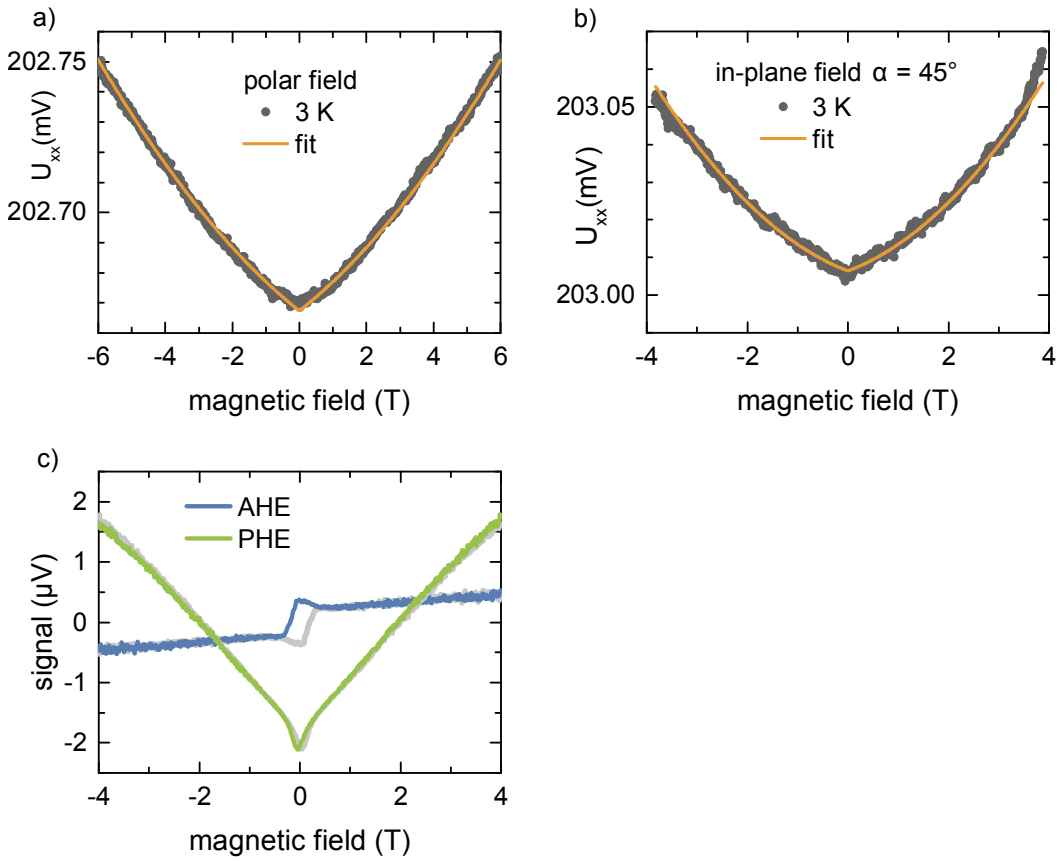

fig 4.27 Voltage in current direction with a magnetic field a) perpendicular to the sample plane (polar) and b) in-plane with the angle $\alpha = 45°$ towards the current direction, both at 3 K. A fit with $f(x) = ax^2 + b|x| + c$ was applied. Clearly a quadratic contribution can be observed for the high field behavior giving indication that LMR is present . c) High field behavior of the PHE and AHE signal at 3 K (calculated from transversal voltage). No quadratic contribution can be observed, but a linear slope also for high fields in the AHE signal.

y-axis) is plotted over temperature. As a comparison the high field slope of the hysteresis curves recorded with a field in out-of-plane direction (see fig 4.17) is also shown (in black, left y-axis). Both slopes exhibit a very similar temperature dependence. Since the (super)paramagnetic background is the origin for the high field slopes of the easy axis hysteresis curves, (super)paramagnetic background might be the reason for the PHE high field slope as well. The exact mechanism how (super)paramagnetic background can cause this kind of signal is unclear however and no further measurements

were done.

other effects: Another high field anisotropy was found by Hille in his PhD thesis [169]. He called it anisotropic high magnetoresistance (AHMR). He found a non linear deviation from the SMR slope in $(Co0.8/Pt0.8)_4$ wires in the transversal magnetoresistance and could verify this effect also for single layers. He found a strong dependence on the Co layer thickness but only a weak dependence on the temperature. Also the difference between longitudinal and transversal voltage was not linear. Therefore the AHMR is probably a different effect, but maybe it also has to be considered in a more detailed investigation of the high field behavior of the here presented nanodots.

Another consideration is that somehow the geometric constriction of the nanodots could also play a role.

Indication that either the geometry or the fabrication process of the nanodots could influence the high field magnetoresistance was found by Ziesmann in his bachelor thesis [170]. For an ensembles of nanodots with thicker Co layer (3.5 and 7 nm) also a high field anisotropy occurred, which was not observed in the corresponding films. The difference between longitudinal and transverse magnetoresistance measurement seemed to be again non linear however and were done at room temperature. Also his initial films were fabricated with slower deposition rates and therefore have in general slightly different properties from our established standard films, used within this thesis. The double layer structure of the nanodots cannot be the origin of the effect, since similar temperature dependence is also observed with individual single layer nanodots.

4.2.6 PHE signals for a magnetic field applied in different in-plane directions

In order to verify the assumed PHE nature of the high and low field signal, that was discussed in the previous section, hysteresis curves in various in-plane angles were measured at 3 K. The axially symmetric signal (PHE) is separated and the point symmetric contribution (PHE) as described in fig 4.19. Then high field and low field contribution of the axially symmetric PHE signal are evaluated. The results are shown in fig 4.28 for the high field slopes a) and the signal height b). The experimental data can be fitted with a $f(\alpha) = A \sin\alpha \cos\alpha$ function (see eq. 2.24) in both cases. This behavior is expected for planar Hall effect (PHE) as

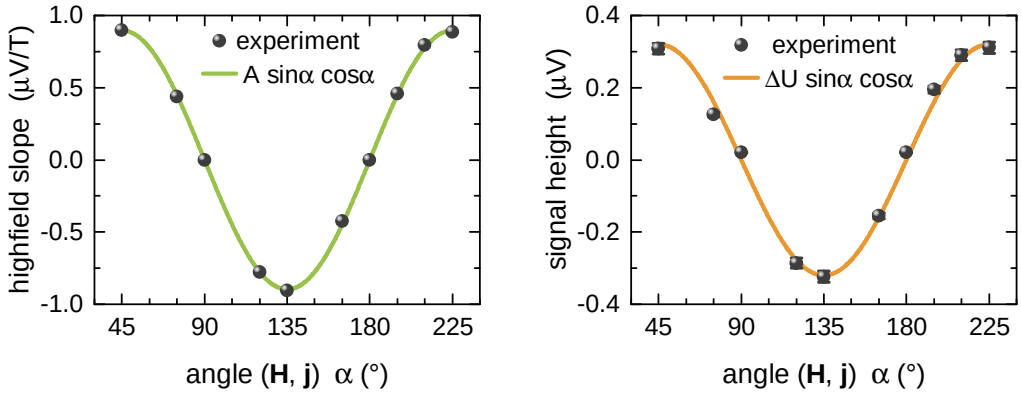

fig 4.28 Experimental data with $f(\alpha) = A \sin\alpha \cos\alpha$ fits for a) high field slope and $A = 1.8\,\mu V/T$ b) signal height $\Delta U = 0.64\,\mu V$. In a) the error bars are invisible, while in b) they are very small.

described in section 2.2.3. This gives proof that indeed both signals are caused by PHE as was only assumed in sec 4.2.5 . Therefore this signal is caused by a difference between the longitudinal voltage when a magnetic field is applied in current direction ($\alpha = 0$) or perpendicular ($\alpha = 90°$) to the current (but still in-plane). The low field signal (fig 4.24) can be attributed to AMR and AIMR of the nanodots due to the reversal of the magnetization (as described in the previous section). The high field signal is most likely related to the superparamagnetic background, but to find out the exact nature more detailed experiments are necessary.
In total the signal height of the high field PHE is at $\alpha = 45°$ $0.9\,\mu V/T$ thus a little lower than $4\,nV/T$ for each dot (240 dots). The total signal height of the low field PHE signal at $\alpha = 45°$ is $0.32\,\mu V$ and thus a little more than $1\,nV$ for each dot.

4.2.7 PHE signal and switching fields with magnetic fields rotated between in-plane and out-of-plane direction

Both the AHE and PHE signal are evaluated from hysteresis curves with fields applied in various directions between in-plane and out-of-plane. Here the in-plane component of the magnetic field always has an angle of $\alpha = 45°$ with the current. First the PHE signal will be discussed.

PHE signal

In fig 4.29 the amplitude of the total (high and low field) PHE signal are shown as the field direction is varied between out-of-plane and in-plane. The maximum field applied was 0.5 T. From theory it can be expected that the PHE signal changes with $\sin^2\theta$ with the angle θ between field direction and sample plane normal (see eq. 2.25). Except from a small deviation at 0° and strong deviations at 60° and 75° the experimental data follows the $\sin^2\theta$ dependency. This is another evidence for PHE and shows that the influence is maximal in in-plane (with α=45°) and vanishing in out-of-plane fields.

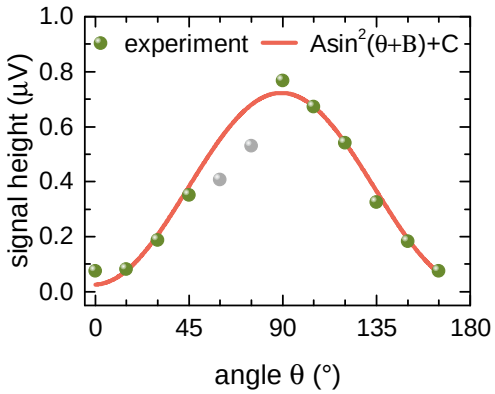

fig 4.29 Signal height over angle between field direction and sample plane normal ($\theta = 0$ corresponds to out-of-plane $\theta = 90°$ to in-plane direction with $\alpha = 45°$) at 3 K. To the data a $\sin^2(\theta)$ fit was applied. The results are $A = 0.7\,\mu V$, $B = 0.7°$ and $C = 0.03\,\mu V$. Gray points are not included in the fit.

The here described PHE signal are also present in the in-plane measurements of individual nanodots (also in single layer nanodots). The temperature dependence was similar, however the signal proportion in the measured transversal voltage was smaller. For low temperatures only a small asymmetry in the hysteresis curves was observed and the effect disappeared for temperatures above 100 K. Two examples are shown in chapter 5.3.4 in the first and second column at ±90°. A separation in high field and low field part was thus not possible for individual nanodots.

Switching field for different angles

The switching field over the angle of the field direction is shown in fig 4.30 at 3 K and at 150 K. At 150 K the maxima near 0° and 180° (correspond to easy axis direction) almost disappear. The field amplitude between maximum and minimum is only 30 mT.

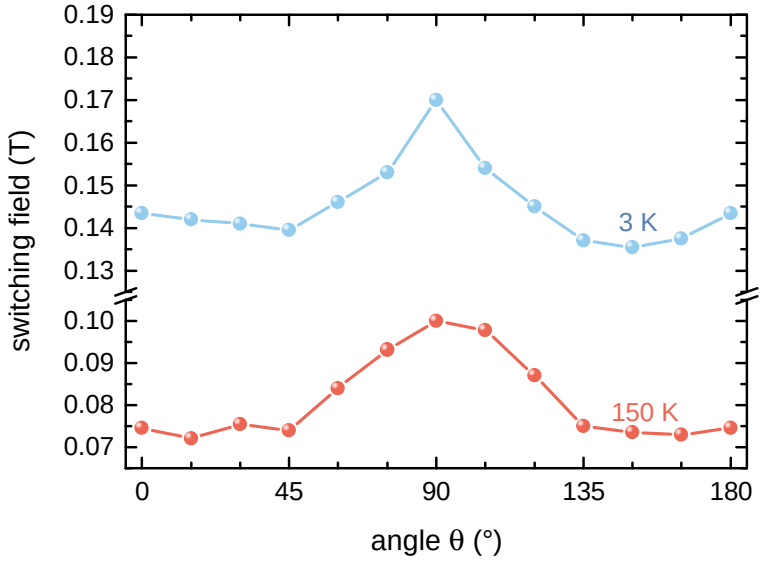

fig 4.30 Switching fields of the ensemble of double layer nanodots with different applied field angles.

For the 3 K measurement a more pronounced but still comparably small local maximum in the easy axis direction can be observed. For both temperatures a high hard axis ($\theta = 90°$) maximum value can be observed. The switching field varies also by 30 mT at 3 K for different angles.
This behavior cannot be described by Stoner-Wohlfarth model even if a second order anisotropy constant is considered. The ensemble of nanodots have most likely tilted easy axes in various different directions.
A very low dependence on the angle of the switching field direction of an array of nanosized bits with tilted anisotropy axes was found in simulations by Krone et al. [171]. They found for tilting angles larger than 25° no dependence on the switching field angle at all. On the other hand the double layer nanodots presented here have a different shape than the bits that were simulated by Krone et al. For our dots the ratio between thickness and lateral dimension is ≈ 0.1, while for the bits investigated by Krone et al. the ratio is 0.5. Furthermore in their simulations all bits have the same angle with the z-axis of their system, while we expect a certain distribution of angles and some of the dots might not be tilted at all. But the trend is of smaller dependence on the switching field direction is similar.
From the switching field dependence also astroids can be calculated. The results are shown in fig 4.31. The astroids have a much rounder shape than expected from the SW model. This round shape is also an indication for a distribution of tilting angles.

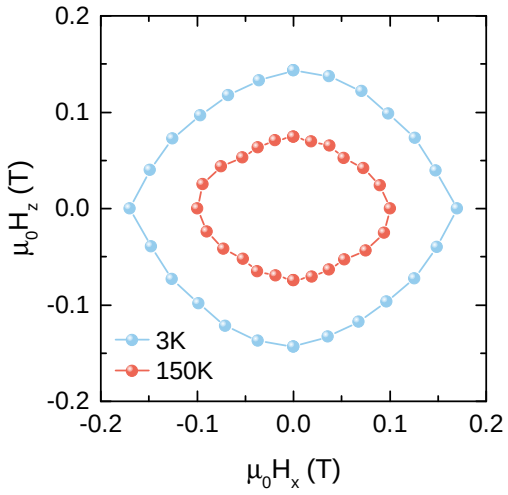

fig 4.31 Angle dependent switching fields in the astroid picture. The ensemble has an average out-of-plane anisotropy. The rounded shape gives indication that the individual dots have a certain tilting of the easy axis.

5 Dots with non-coherent reversal of magnetization

Some of the nanodots with a Co single layer show a rather unexpected behavior at low temperatures. Instead of one defined jump in the hysteresis curve, a second jump appears. It seems like the one jump at higher temperatures splits into two at lower temperatures. This observation cannot be explained by coherent rotation of a macrospin in a uniaxial potential (Stoner-Wohlfarth model). The experimental results will be presented phenomenologically in the next section and in section 5.2 simulation will explore possible reasons for the appearance of a second jump.

5.1 Experimental findings

A dot, with a diameter of 35 nm and a Co thickness of 1 nm, was studied and is compared to the switching behavior of a nanodot with a Co thickness[1] of 1.4 nm and a diameter of 60 nm. The magnetic field was sweeped from positive to negative values and back perpendicular to the sample plane at different temperatures, while the transversal voltage was recorded as described in chapter 4.
The smaller dot is located on the same piece of substrate as the dot in chapter 4.1. It was fabricated from the same film material at the same time with the same procedure. Also for this dot one jump is observed at 80 K (see fig 5.1 a)). The switching fields increase for lower temperatures, but below 50 K a rather unexpected behavior occurs, a second jump appears in the hysteresis curve.
For the bigger nanodot a very similar behavior is observed. A second jump appears already below 160 K (fig 5.1 b)). In both cases the switching field of the first jump varies only little with temperature, while the switching field of the second jump increases for smaller temperatures. The signal height of the first jump is much higher (roughly 2 times) than the signal height of the second jump. The sum of the signal height of the first and second jump are the same as the signal height of

[1] The first Pt layer of this nanodot is 10.6 nm thick, thus the whole composition is: Pt 10.6 nm/Co 1.4 nm/Pt 3 nm

the initial one jump at higher temperatures. Apart from that a slight reduction in signal height with decreasing temperature (220 to 2 K) can be observed in the measurement in fig 5.1 b).

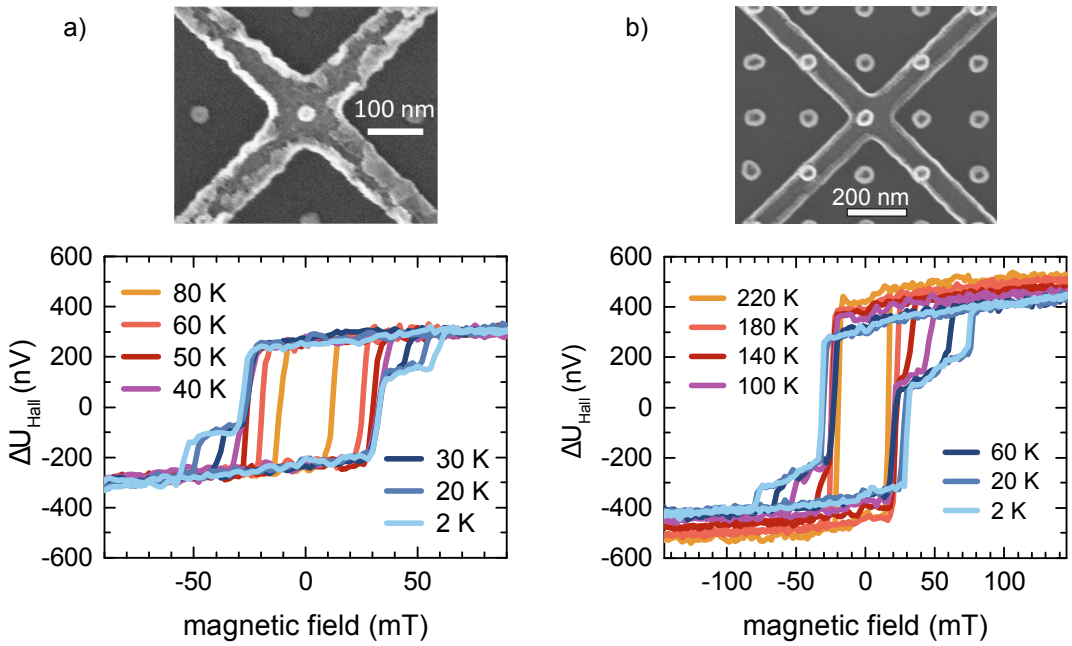

fig 5.1 a) SEM micrograph and hysteresis loops of nanodot with $t_{Co} = 1\,nm$ and a diameter of 35 nm. The dot is located on the same piece of substrate as the dot in section 4.1. Each curve is an average of several (3-8) measurements. The coercive fields increase for decreasing temperatures. Below 40 K a second jump with $\sim \frac{1}{4} - \frac{1}{3}$ height of the total signal appears in the hysteresis curves. The field of the first jump in the hystereses then does not change with temperature, only the field of the second jump increases. There is an additional slope visible in the signal. b) Another nanodot with the following dimensions: $t_{Co} = 1.4\,nm$ and a diameter of 60 nm. The behavior of the switching field is quite similar to the dot in a), except that the second jump appears already below 160 K. Here clearly an additional signal from rotation of the magnetization can be observed, since the field range is also wider than in a).

As in chapter 4 an additional slope is visible in both hysteresis curves and, as before, this slope can be attributed to a rotation of the magnetization due to a tilted easy axis. For the smaller nanodot the rotational character is not visible at first glance (see fig 5.1 a)), but it becomes more obvious if higher fields are applied as in fig 5.2. For the bigger dot in fig 5.1 b) the rotation is more obvious, since the field range is higher. That rotation is indeed the origin of this signal contribution and the simulations in section 5.2 and 5.3 will confirmed that .

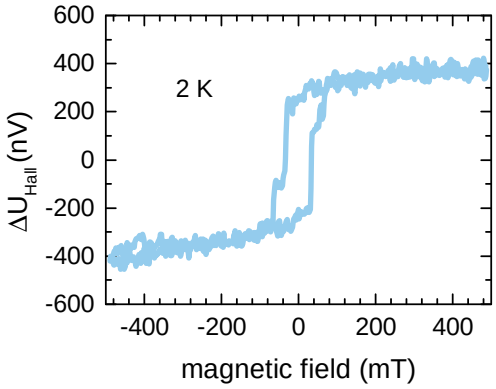

fig 5.2 Hysteresis curve of the dot in fig 5.1 a) with more field applied. Two curves were averaged. Here clearly the rotational contribution in the signal can be observed, that appears in fig 5.1 a) due to the small field range as an almost linear slope.

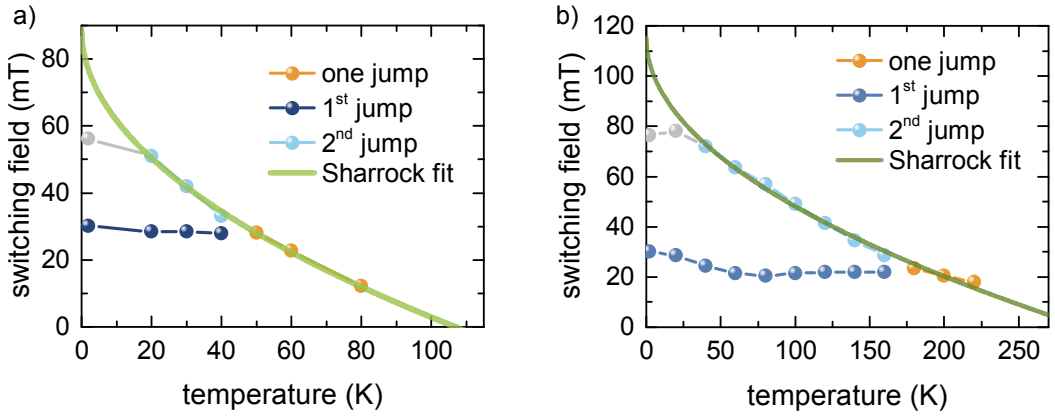

fig 5.3 Switching fields against temperature for both nanodots in fig 5.1. The second jump and the jumps for higher temperature can be fitted according to Sharrock. The first jump stays almost constant for different temperatures. a) The nanodot with $t_{\mathrm{Co}} = 1\,\mathrm{nm}$ and a diameter of 35 nm. From the Sharrock fit: $K = (65 \pm 1)\,\mathrm{kJ/m^3}$ and $T_B = (107 \pm 2)\,\mathrm{K}$ (datapoint in grey for 2 K excluded). b) The nanodot with $t_{\mathrm{Co}} = 1.4\,\mathrm{nm}$ and a diameter of 60 nm. From the Sharrock fit: $(84 \pm 2)\,\mathrm{kJ/m^3}$ and $T_B = (294 \pm 6)\,\mathrm{K}$. (Values for 20 and 2 K, grey datapoints are excluded from fit. In both diagrams straight lines connecting the data points are guides to the eye only.)

In fig 5.3 the switching fields are plotted against temperature for both dots. They show very similar features, though at different temperatures. In the temperature regime with one jump (orange data points) an almost linear change of the switching field can be observed. As already mentioned in the two jump temperature regime the first jump (dark blue data points) varies only little with temperature. The

switching field of the second jump (light blue data points) increases with lower temperatures and levels off for very small temperatures (grey data points). This kind of plateau at $T < 20\,\mathrm{K}$ is also observed and discussed in the previous chapter 4.1.1. To the second jump a fit accordinng to Sharrock's formular (eq. 2.12) can be applied (grey data points are excluded). The data points in the one jump regime agree quite nicely with the fit, they are a continuous extension of the second jump. These features are very similar for both nanodots even though the dot's dimensions are rather different. For the smaller dot with a cobalt thickness of 1 nm the resulting anisotropy constant from the Sharrock fit is $K = (65 \pm 1)\,\mathrm{kJ/m^3}$ and the blocking temperature is $T_B = (107 \pm 2)\,\mathrm{K}$. For the dot with bigger diameter and $t_{\mathrm{Co}} = 1.4\,\mathrm{nm}$ the results are $K = (84 \pm 2)\,\mathrm{kJ/m^3}$ and $T_B = (294 \pm 6)\,\mathrm{K}$. As expected for a larger volume and anisotropy, the blocking temperature is here higher than for the smaller dot.
It has to be considered that a prerequisite for the application of a Sharrock fit is still coherent rotation of a macrospin in a system with uniaxial anisotropy, which is certainly not fulfilled when the hysteresis curve has two jumps. Additionally the field has to be applied in the easy axis direction, which is tilted for both dots as will be discussed in the next section. Therefore the Sharrock fit can give only a rough estimate of the dot's anisotropy constants and the blocking temperature.

5.1.1 Angular dependence of the switching process

As another experiment the magnetic field was applied in different directions and the hysteresis curves were measured. From each curve the switching field was deduced and an average switching field calculated. This was done for the smaller nanodot in fig 5.1 at 2 K and for the bigger dot in fig 5.1 b) at 80 K. Again many curves were averaged to one curve, the shape of these hysteresis curves will be shown and discussed later on in section 5.3.4. In fig 5.4 the switching fields for both nanodots are plotted over the corresponding angle of the applied field direction.
The hard axis (h.a.) direction can be detected from a sign change of the jump in the hysteresis curve (see fig 5.26). The easy axis (e.a.) is then expected 90° apart from the h.a., but many times the measurements show deviations of a couple of degrees. The e.a. can be detected as another maxima of the switching field. In the hard axis (plane) direction always two jumps can be observed (see fig 5.4).

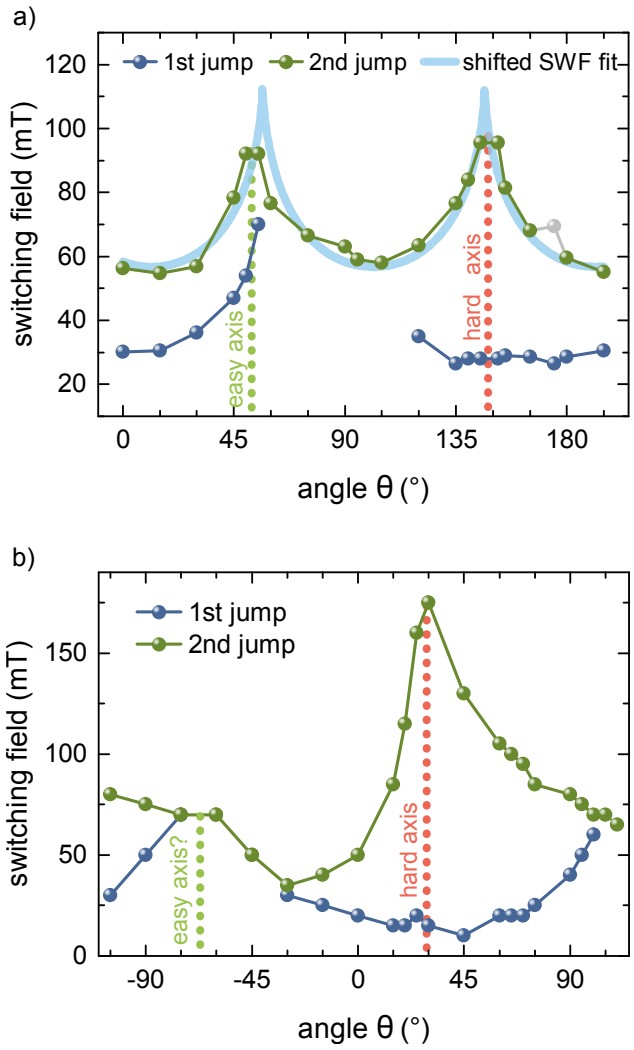

fig 5.4 Switching fields for different field directions. a) The first dot with $t_{\mathrm{Co}} = 1\,\mathrm{nm}$ and a diameter of 35 nm at 2 K. The easy and hard axis are strongly tilted. The hard axis (h.a.) direction is detected from a sign change of the jump in the hysteresis curve. For the easy axis directly from the measurement 53° is received. From a SW fit the easy axis is received at $(56 \pm 0.7)°$. The hard axis has an angle of 150° from measurement and 146° from the fit. The grey data point is not included in the fit. Also from SW fit a value for the anisotropy is received: $K = (104 \pm 2)\,\mathrm{kJ/m^3}$. The angle dependence of the first jump is entirely different. It is almost constant near the hard axis of the second jump and has a maximum near the easy axis of the second jump. Between 60° and 105° no first jump is observed. b) Switching field dependence at 80 K of the second dot with $t_{\mathrm{Co}} = 1.4\,\mathrm{nm}$ and a diameter of 60 nm. The hard axis can be found at 28° from measurement. The position of the easy axis is not clear. From theory another maximum would be expected 90° from the hard axis, near -68°. However there is no second maximum, rather a plateau. Further insight gives the switching field astroid in the next section.

The angular switching field dependence of the first jump has a minimum or kind of plateau and a higher value is detected in or close to the easy axis direction. All these properties occur for both nanodots.
For the smaller dot (shown in fig 5.4 a) at 2 K) a Stoner-Wohlfarth model (SW) (eq. 2.8) can be fitted to the second jump. Small deviations from the measured easy and hard axis are received. Also from this fit an anisotropy constant is obtained: $K = 104\,\mathrm{kJ/m^3}$. This value is much higher than the one from the temperature dependent Sharock fit in fig 5.3 a), where $K = 65\,\mathrm{kJ/m^3}$. At first glance this seems surprising, since the data point for the 2 K measurement in fig 5.3 a) lies $\sim 20\,\mathrm{mT}$ below the actual Sharock fit. Additionally in the SW fit no reduction due to temperature was considered (even though this reduction would be only small at 2 K). The values used for the temperature depended Sharrock fit were measured with field in 0° direction (perpendicular to the Hall bar plane). In the Sharrock fit it was assumed that the easy axis lies in this direction and is not tilted. The dependence of the switching field on the angle, shown in fig 5.4 a), exhibits however a minimum at 0°. The maximum would be at 113 mT and 56° (from the SW fit). The values received from the Sharrock fit are therefore only a lower estimate of the anisotropy. In order to receive a more accurate value for the anisotropy it would be necessary to measure along the easy axis and verify that the tilting angle as well as the switching field dependence changes with temperature. Apart from this experimental improvements it has to be kept in mind that the switching is clearly not coherent and thus models for coherent switching have limited validity.
The switching fields at 80 K of the bigger dot with $t_{\mathrm{Co}} = 1.4\,\mathrm{nm}$ with 60 nm diameter is shown in fig 5.4 b). Near the hard axis at 28° the angle dependence of the first and second jump are qualitatively similar to the smaller dot. 90° from the hard axis no defined maximum can be identified and the direction of the e.a. can be guessed only. No Stoner-Wohfarth model can be applied to this data.

As in chapter 4, a switching field astroid can be calculated from switching fields with eq. 4.1 and the angles (θ) of the applied field. The results for both dots are displayed in fig 5.5. Both astroids are tilted. If we look at the second jump (light blue data points) only for the small dot with 1 nm Co an almost SW like shape can be observed. Furthermore the data points of the first jump (dark blue) can be found inside the astroid.
The lager dot (with 1.4 nm thick Co) exhibits a more distorted shape. The data points from the second jump form here an astroid that looks more like the astroid

in the xy-plane (green color) found for the dot in sec. 4.1.2.

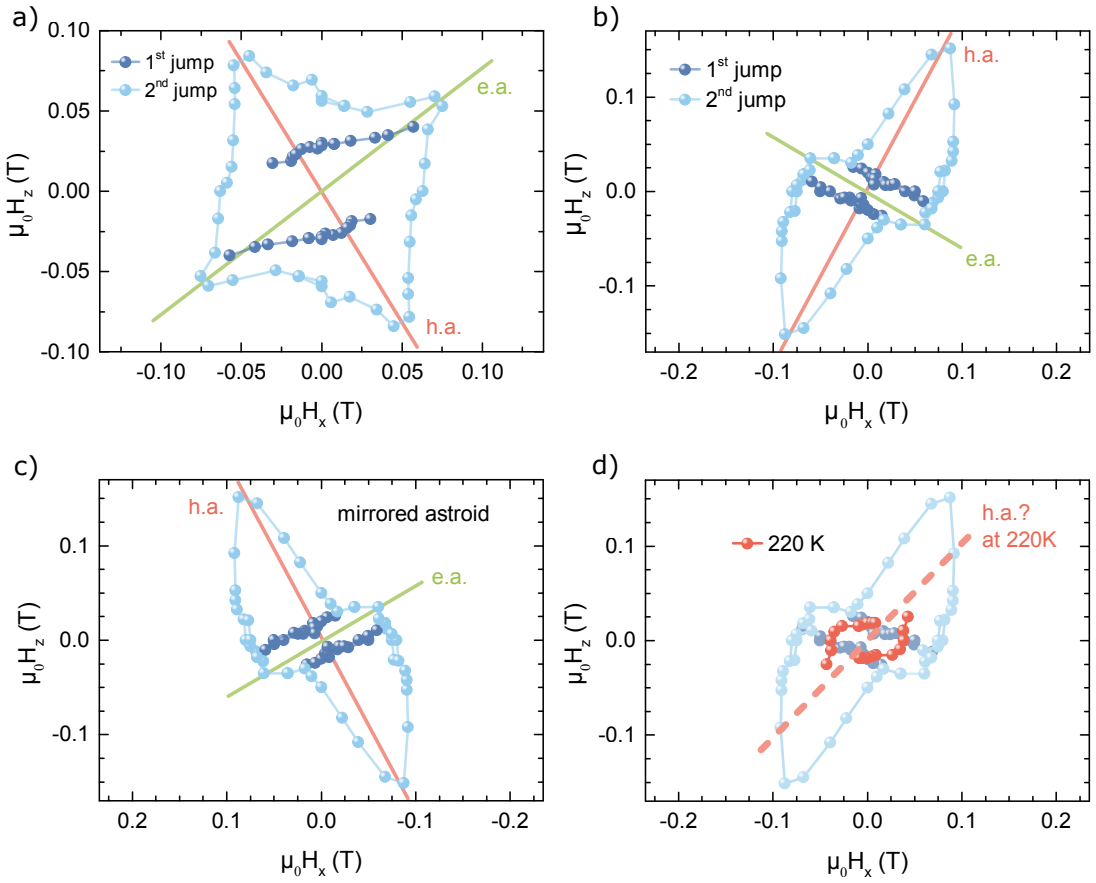

fig 5.5 a) Astroid of the nanodot with 1 nm thick Co calculated from fig 5.4 a) at 2 K. b) Astroid for the dot with 1.4 nm thick Co at 80 K. From this measurement the e.a. can be decided as -60°, while in the diagram of the switching field over angle in fig. 5.4 b) the exact position was not clear. c) Same as b) but the astroid is mirrored at the z-axis. This helps to compare the similarities with the astroid in a). The easy and hard axis have a similar tilt as in a). d) same as in b) but the astroid measured at 220 K is added. Here only one jump is observed. Most likely in 45° direction the hard axis is found. The hysteresis curves exhibits fluctuations in that direction and since only 3 hysteresis curves were recorded, it was not possible to evaluated these curves properly. In all diagramms connecting lines between the data points are guide to the eye only.

From this representation of the switching field the easy axis direction can be deduced as -60°.

Additionally the data points from the first jump (dark blue) appear more clearly

oriented than in a) parallel to the easy axis. In easy axis direction only one jump can be observed, that is referred to as the second jump here, in this way the outer shape of the astroid becomes more visible.
The experiment with the larger dot was also repeated at 220 K (fig 5.5 d)). Here for all directions only one jump could be observed. The astroid lies within the outer shape of the 80 K switching field astroid what is expected since the switching fields should be smaller due to thermal activation. The hysteresis curves of the 45° measurement could not be evaluated, since only 3 curves were recorded and these curves showed fluctuation. It can be concluded that the hard axis must be close to 45°, as a field component in hard axis direction lowers the energetic barrier and at elevated temperatures it is possible for the magnetization to overcome this barrier by thermal activation. This process causes fluctuations in the hysteresis curve. The hard axis at 220 K is less tilted from the ideal 90° than for the 80 K measurement. The direction of the easy axis is also difficult to detect. It seems that it is more or less unchanged. Thus easy axis and hard axis are probably not perpendicular at 220 K. The change in the hard axis direction might be caused also by an increase of the shape anisotropy at lower temperatures as will be discussed in section 5.2.2. But that is in contradiction to the unchanged easy axis of the system.
Another very interesting similarity of both switching field astroids becomes visible if we mirror the astroid of fig 5.5 b) on the $\mu_0 H_z$ axis of the diagram (cp fig 5.5 c)). Like this the similarities become more apparent and it becomes obvious that the angles of the easy and hard axes with the z-axis are actually almost the same.
In summary, clearly non-coherent switching behavior of the magnetization for lower temperatures is found. The easy and hard axis of the smaller and bigger nanodots is strongly tilted and the switching behavior shows many similarities, even though both systems are different in diameter, Co thickness and blocking temperature.

Incoherent switching in literature

Some examples of incoherent switching of nanodots with properties (anisotropy, size, exchange interaction) that are predestined for coherent switching can be found in literature. Here a short overview is given.
Wernsdorfer et al. also found for an elliptical 30 nm thick Co particle with $a = 80$ nm and $b = 50$ nm for certain angles second jumps in the hysteresis curves at low temperatures [172]. Since their particles exhibited only shape anisotropy and some deviations from an ideal ellipse, their found angle dependence was rather

complex however.
Also Ross et al. found indications for non-coherent magnetization reversal in ensembles of Ni cylinders with a diameter of 30 nm, an exchange length of $\lambda_{ex} =$ 20 nm and 40 nm thickness [173]. Through calculations they could describe their experimental results by a model with a switching volume equal the volume of the columnar grains of the cylinders.

Probably one of the first hints that a Stoner-Wohlfarth like switching field dependence on the direction of the applied field is not necessarily caused by coherent rotation of a macrospin was found in simulations by Uesaka et al. [72]. They studied a hexagonal particle with a lower anisotropy region in the middle and at the corner of the hexagon. This low anisotropy region would reverse at lower fields and then a domain wall travels through the rest of the hexagon. The switching field in the easy axis direction was a little lower than the switching field in the hard axis direction, as was observed also in the experiments in sect. 4.1.2.

Experimental evidence was brought when Hu et al. showed that also an array of 5 µm large Co/Pd multilayer islands can exhibit a Stoner-Wohlfarth like dependence of their angular switching behavior, while also a multi domain state can be stabilized in the island [27, 74]. They suggest that this angular switching dependence is caused by smaller nucleation volumes, that switch coherently at the nucleation field H_n. Since the propagation field for domain walls is lower than H_n the domain wall runs immediately through the islands. As a proof they inserted reversed domains by application of an in-plane field, this domains are observed by MFM. With these prereversed domains they find a for domain wall propagation typical $\frac{1}{\cos\theta}$ dependence of the switching field.
In a related paper by Dittrich et al. [73] did micromagnetic finite element simulation and showed that the minimum of the angular dependence is less than 0.5 $H_c(0°)$ (as would be expected by the Stoner-Wohlfarth model), since the easy axes of the grains in the islands have a dispersion in the directions. The domain wall width in the simulated system is $\delta_{DW} = \pi\sqrt{\frac{A}{K}} = 12$ nm and they find non-coherent switching for islands of 70 nm size (nucleation followed by immediate domain wall propagation) and coherent switching for islands with a size smaller than 30 nm. The angular dependence of the switching behavior is almost the same for both cases.
Delalande et al. confirm this findings for individual Co/Pt multilayer dots with a diameter of 250 nm and 350 nm by MFM and AHE measurements [174].
Kikuchi et al. could obtain the nucleation volumes from AHE on arrays of Co/Pt multilayer and hcp CoPt dots from the dependence of the switching field of

the sweep rates [175, 176]. They found similar nucleation volumes for dots with different diameters (30 nm to 200 nm) and could relate these nucleation volumes to the grain size of their dots (11 nm to 17 nm).
In a study by Lau et al. [177] they tried to relate the microstructure of 115 nm (diameter) Co/Pd dots measured by TEM to the switching behavior. By diffraction and dark-field TEM they identified misaligned grains in dots, that switch at lower fields than others. But a similar study by Kikuchi et al. on Co/Pt multilayer dots could not confirm these findings [178].
Thus for many nanodot systems it is suggested, that the switching of the magnetization is initialized by one grain followed by domain wall propagation. Some authors claim that misaligned grains could cause this behavior. It was found, that Stoner-Wohlfarth like behavior is not necessarily caused by coherent rotation of the magnetization of the entire nanodot.

All these results, from literature and from the experiments with non-coherent switching of two different nanodots, are the reason why the influence of the grains in the dots will be studied by micromagnetic simulations in the next chapter.

5.2 Simulations of a multigrain dot

From XRD, high resolution TEM measurements done by Winkler et al. [63] and SEM measurements on thicker Co films, we know of the granular character of the initial film samples (see sect. 3.1 for more details).
In order to investigate the possible influence of the grains, micromagnetic simulations were performed with MuMax3, a GPU-accelerated micromagnetic simulation program [62].
First simulations with many grains were carried out studying the role of exchange interaction between the grains (sec 5.2.1). Then in sec 5.2.2 a random tilting of the anisotropy axis in the individual grains is evaluated. Furthermore in sect. 5.3 a simplified model of two grains is introduced to investigate the magnetization reversal process for several tilting configurations of the anisotropy axes in more detail.
The shape of the dot is approximated by a cylinder with a diameter of $d = 38.4\,\mathrm{nm}$ and Co thickness (height of the cylinder) of 0.8 nm. A grid of 256x256 cells is chosen with a lateral cell size of $0.15\,\mathrm{nm} \times 0.15\,\mathrm{nm}$ and the thickness of the cylinder 0.8 nm. The magnetic parameters for the simulations are chosen like for bulk Co. The saturation magnetization is $M_S = 1440\,\mathrm{kA/m}$ [75][2], the exchange interaction[3] is $A_{\mathrm{ex}} = 31.4\,\mathrm{pJ/m}$. The damping parameter[4] α was set to 0.5. For an easy axis parallel to the cylinder axis (or z-axis), an anisotropy constant of $K_{\mathrm{uniax}} = 1.5\,\mathrm{MJ/m^3}$ is assumed. With a calculated shape anisotropy after Millev et al. [69] of $K_{\mathrm{shape,dot}} = 1.156\,\mathrm{MJ/m^3}$ the effective anisotropy is $K_{1,\mathrm{eff,dot}} = K_{\mathrm{uniax}} - K_{\mathrm{shape,dot}} = 344\,\mathrm{kJ/m^3}$. All simulations were performed without thermal excitations at 0 K. A small field misalignment of 0.2° was assumed in

[2] This is the M_S value for hcp Co at room temperature. In the experiments variable temperatures, mainly below RT were applied. It is not entirely clear how the saturation magnetization is reduced in ultrathin sputtered systems. More detailed discussion can be found in the PhD thesis of J. Wagner [133]. These deviations in M_S will however not change the qualitative results of the simulations.

[3] A_{ex} can be calculated by $A_{\mathrm{ex}} = \frac{DM_S}{2g\mu_B}$ [179], with the spin wave stiffness $D = 490\,\mathrm{meV\AA^2}$ for bulk hcp Co [180]. The value of $A_{\mathrm{ex}} = 31.4\,\mathrm{pJ\,m^{-1}}$ was taken from Stickler [76], he refers to [181] (who gives a value for D) but omits the derivation of A_{ex}. With the values for D for hcp Co given in this reference however $A_{\mathrm{ex}} = 28 - 29\,\mathrm{pJ\,m^{-1}}$ (using $g = 2.21$ [182], $M_S = 1440\,\mathrm{kA\,m^{-1}}$ [75]). The exchange constant for fcc Co [181] and also thin sputtered films will be even smaller. This is a topic of a recent PhD thesis by J. Wagner and discussed there in detail [133]. For the simulations done in the present thesis the accurate value of the exchange constant is not of major importance. For future simulations a reduced exchange constant should be considered however.

[4] A damping parameter of $\alpha = 0.5$ is a little exaggerated, but quasi static states are considered only, which makes it reasonable to assume a high damping parameter in order to achieve a fast relaxation of the LLG equation and thus reduce computation time.

order to prevent the numerical problem of a vanishing torque if magnetization and field are aligned perfectly parallel.
In simulation with many grains an average grain size of 12 nm is assumed. The grains are obtained by Voronoi tessellation [183], similar as in OOMMF [184]. The grain distribution, used for the simulations, is shown in figure 5.6.

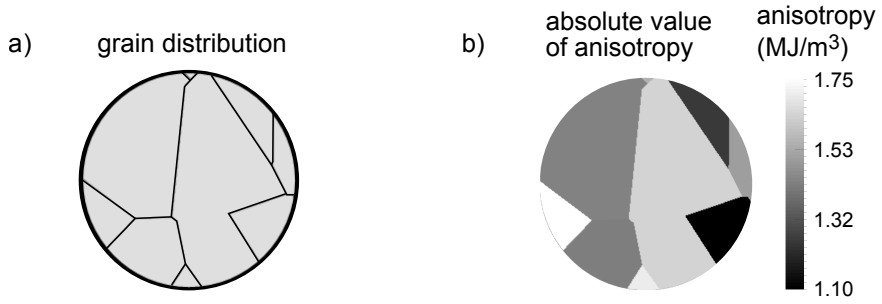

fig 5.6 a) Grain distribution of the simulated dot. The dot consists of 9 grains. The grains are obtained from Voronoi tesselation implemented in MuMax3. The mean grain size is 12 nm. The dot thickness is 0.8 nm and the diameter 38.4 nm. In b) a color code for the absolute value of the anisotropy of the grains is given. The mean anisotropy is $K_{\mathrm{uniax}} = 1.499\,\mathrm{MJ/m^3}$ (the size of each grain is taken into account to calculated this value).

For these multigrain simulations a gaussian distribution of the anisotropy K_{uniax} of the grains with a σ $\pm 10\%$ of the initial value was assumed. A map is shown in fig 5.6 b). A similar approach was followed by Thomson et al. [27], who found that an anisotropy distribution with a σ of 7.6% could explain their experimental SFD data for Co/Pd multilayer islands with different sizes very well. A variation in anisotropy could be caused by variation of the local grain structure, stress or also small local deviations of the interface. It was found, however, that in principle this variation of the anisotropy value did not change the qualitative reversal behavior of the simulated dots. Simulations with a constant anisotropy showed only small quantitative deviations.

5.2.1 Reduced exchange interaction between grains

In this section the influence of exchange interaction between grains will be discussed. The first idea was, that a reduced exchange interaction between the grains of the polycrystalline Co/Pt film could cause uncorrelated switching of the grains in a dot.
Reductions in grain exchange could be caused by another material diffusing into

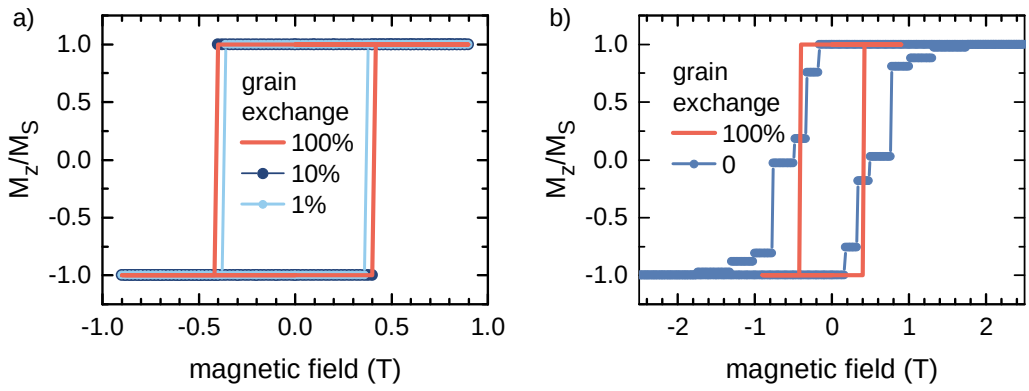

fig 5.7 Hysteresis curves of the simulation with variation of the exchange interaction between grains. a) For 10% of the initial value no changes in the hysteresis curve appear. For 1 % the switching field is reduced by 40 mT. b) Only for 0 grain exchange several small steps in the hysteresis curve can be observed. Much higher fields are required for a fully saturated state (2.5 T). In this simulation only one half of the hysteresis curve (saturation in positive field → saturation in negative field) was simulated. The other half was then complemented for more intuitive comparison to the experimental results. For micromagnetic simulations the result of backward and forward loop is point symmetric at 0 K. A 10% variation of the anisotropy was assumed.

the grain boundaries, e.g. Pt or a certain distance between the Co grains [185]. Therefore simulations of the grain distribution shown in fig 5.6 were done with a variation of the grain exchange between 100% and 0. The magnetization of the dot was first relaxed at 0 T and then saturated at 1 T (or 2.5 T for zero grain exchange). Afterwards the field was decreased in small steps of 20 mT to −1 T (or −2.5 T for zero grain exchange). This was repeated for the other field direction. The resulting hysteresis curves are depicted in fig 5.7. The normalized z-component of the magnetization is plotted over the magnetic field in order to compare the simulation with the Hall measurements. Coming from positive fields and sweeping to negative fields in fig 5.7 a) for 100% and 10% the magnetization switches all at once at −0.41 T. For 1% the switching field is decreased to −0.37 T. This decrease in switching field is accompanied by a very small reduction in the $m_Z = M_Z/M_S$ component (< 1%), that is not visible in the hysteresis of the diagram. The magnetization state is therefore homogeneous for all simulated fields.

The distribution of the anisotropy of the grains gives only a slight reduction[5] of

[5] a few mT, in the corresponding simulation with constant anisotropy. The magnetic field was unfortunately set to very coarse steps (50 mT) and is therefore not comparable with the simulation with a anisotropy variation presented here. In this coarse simulation of a uniform dot the switching field was between 400 and 450 mT

the switching field compared to a dot with grains with uniform anisotropy. This can be explained by an slightly reduced averaged anisotropy below $1.5\,\mathrm{MJ/m^3}$. The variation of the anisotropy does not change the character of the switching process.
If the exchange interaction between the grains is switched off completely (fig 5.7 b)) the first two softer grains switch at $-0.17\,\mathrm{T}$ already, then gradually all other grains switch according to their anisotropy value. Only at $-2.36\,\mathrm{T}$ the dot is fully saturated. The corresponding magnetization configurations are shown in fig 5.8. White areas correspond to the magnetization pointing out-of the plane, defined in here as up and black corresponds to pointing into the plane this is defined as down. No in-plane components are observed here. The switching starts with some of the smaller outer grains, followed by the bigger grains in the middle and in the end the rest of the smaller outer grains switches at rather high fields. In order to understand the influence of the grain exchange in more detail, the contributions of exchange, demagnetization, Zeeman and anisotropy energy are discussed in the following.

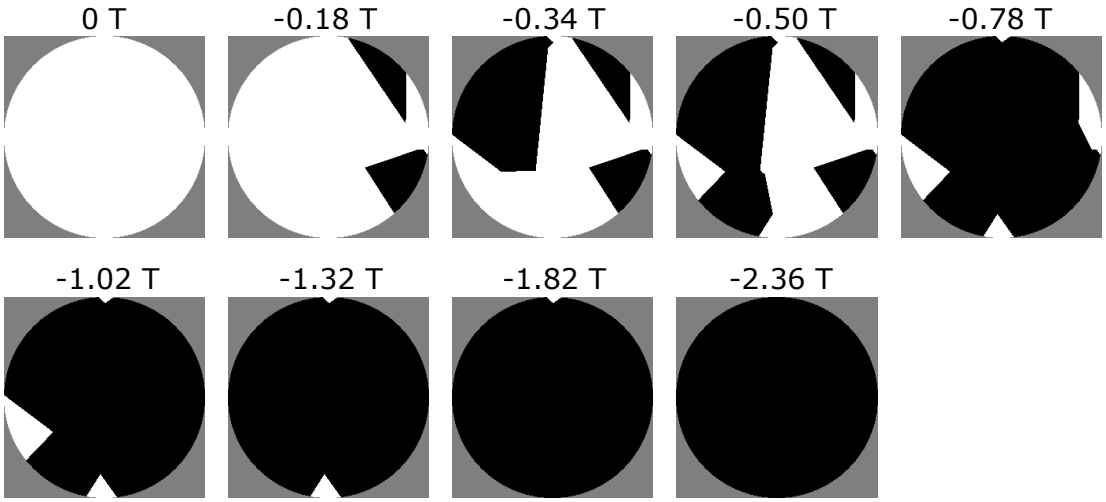

fig 5.8 Switching process for a dot without grain exchange interaction. White represents magnetic moments pointing out-of-plane (up), black represents magnetic moments pointing into the plane (down). No in-plane components are observed. The configuration is shown after each step visible in the hysteresis curve shown in fig 5.7 b). 10% variation of the anisotropy was assumed. From fig 5.9 c) it can be concluded that at $-0.5\,\mathrm{T}$ a minimum in the demagnetization energy is achieved.

Energy contributions

In fig 5.9 the demagnetization, exchange, Zeeman and anisotropy energy are displayed. All these terms determine the equilibrium magnetization state and therefore also the quasi static reversal process (see section 2.1).

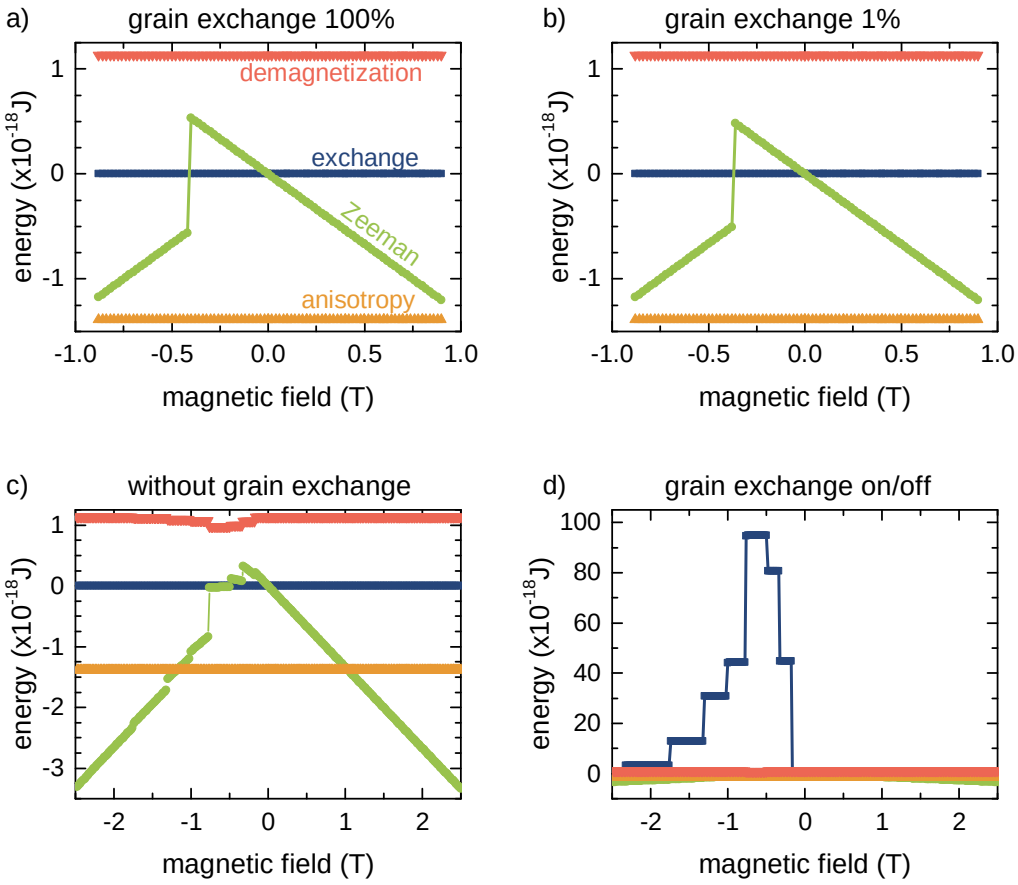

fig 5.9 Energy contributions for different exchange interaction between grains: a) full exchange interaction between grains. b) 1 % grain exchange, almost the same as a). c) no exchange interaction. d) exchange interaction calculated for the magnetization configuration of c) if there was 100% grain exchange. In this simulation after each step of relaxation, the grain exchange was switched on (without relaxing the magnetization further). This way the exchange energy is calculated for this highly inhomogeneous magnetization state if grain exchange was at 100%. For the next relaxation step the grain exchange was switched off again. The exchange interaction energy would be for this configuration about 100 times higher than all other terms. In all cases only half of the full hysteresis loop was calculated.

The dot is saturated first at 1 T or 2.5 T and then the magnetic field is decreased in small steps (20 mT) to −1 T or −2.5 T.

The exchange energy is defined as zero if all magnetic moments align parallel.

For full grain exchange (100%) and 1% exchange the exchange energy is constant at 0 in fig 5.9 a) and b), since the magnetization is homogeneous and pointing either up or down (more precisely out-of the plane or into the plane). Also the demagnetization and anisotropy energy stay constant with varying magnetic fields. For all those energy terms (except Zeeman energy) it does not make any difference if the magnetization of the whole dot is pointing up or down. The Zeeman term however is zero at zero field and decreases linearly with applying a field parallel to the magnetization (positive field values). When reversing the field the Zeeman term is increased linearly until at the switching field the Zeeman term drops from positive to negative values since the magnetization switches from anti-parallel to parallel alignment with the field (compare eq. 2.5). For 1% exchange between the grains the Zeeman energy does not reach the values of the 100 % case since the magnetization of the dot switches at a lower field (fig 5.9 b)). Not visible in the diagram the exchange energy is only very close to zero in the simulation. It ranges from 10^{-23} to 10^{-26} J. The exchange energy is a little higher for a grain exchange of 1%, especially before switching (this is not visible in the diagram). Therefore the degree of incoherence is little higher and this might explain the lower switching field. This differences are very small though. The energy contributions for 10% grain exchange are not shown here, since the difference in energy contributions to the full exchange interaction case is vanishing small.
Without exchange interaction between the grains the demagnetization (equivalent stray field) energy is reduced as soon as some of the grains switch in fig 5.9 c). This switching is also reflected in the Zeeman energy, that decreases as soon as some grains switch. The exchange and anisotropy energy are not affected by zero grain exchange because the magnetization inside the grains is homogeneous, both energy terms remain constant.
The simulation with zero grain exchange was repeated in a modified way. The grain exchange was switched off first for the relaxation. The magnetic field was increased to 2.5 T and relaxed. Then the field was decreased by small steps (20 mT) and after each step of relaxation the grain exchange was switched on to 100%. Then the exchange energy was calculated without relaxing the magnetization. For the next field and relaxation step the grain exchange was set to zero again. This gives the exchange energy needed for all magnetization states shown in fig 5.8, if the grain exchange was set to 100%. It can be seen in fig 5.9 d) that the exchange energy would be up to almost 10^{-16}J for individually switched grains. This means that also with a reduced grain exchange it is energetically favorable for the magnetization to switch coherently, even if the anisotropy is not homogeneous

throughout the dot. The exchange energy is so dominant that a change in grain exchange does not influence the system significantly. Only switching off the grain exchange (or setting to very low values $\sim$0.1%) would result in uncorrelated switching process of the dots. However from film measurements [63, 65] we know that the hysteresis curves have a squared shape and this gives strong indication that a certain degree of grain exchange is present, even though we cannot actually quantify the amount of grain exchange present in the initial film system. Therefore it remains unclear how high the grain exchange in the nanodots is. But also previous measurements [52, 61, 115, 131] and the measured hysteresis curves, presented in chapter 4.1, give due to an almost squared shape indication that also in the nanodots a certain degree of grain exchange has to be expected.

5.2.2 Grains with slightly tilted anisotropy axes

In this section the influence of tilted anisotropy axes in the grains of the nanodot is studied. Therefore first a very short review of tilting in literature is given. In micromagnetic simulations of a Co/Pt multilayer film it was shown that in a polycrystalline film the switching field can be reduced due to decrease in texture [186]. Another micromagnetic FePt simulation with three different degrees of texture confirms that the switching field for such a film is indeed reduced [187]. They find lower nucleation fields for stronger tilting. But they also find stronger pinning of the subsequent domain wall movement for stronger tilting. Therefore the switching field can be similar for different degrees of tilting and even a film with random distribution of grain axes the switching field could be the same as in a film with medium texture. Even though the magnetic parameters used within this simulations are different from the case presented here, they still provide a certain idea on the reversal behavior of polycrystalline films with non-ideal texture.
Some simulations of nanodots were done with low anisotropy inclusion and inclusions, that are tilted [188, 189]. These inclusions are relatively small compared to the diameter (10 nm/50 nm to 2 nm/10 nm) and they do not report on two switching events, that could correspond to two jumps in a hysteresis curve. They also find only a slight reduction of the switching field by an inclusion with a little lower anisotropy. Furthermore there are also micromagnetic simulations on arrays of homogeneous nanodots with tilted easy axis, but they also cannot explain our experimental findings [171].

As we know from former characterization of the Pt/Co/Pt films by XRD rocking scans by Winkler et al. [63], there is certain degree of texture. Some of the crystallite axes of the polycrystalline film are tilted from the out-of-plane direction. They found for a Pt(5 nm)/Co(3.5 nm/Pt(3 nm) film system on SiO_2 in a rocking scan of a Pt peak that can be fitted by a Gaussian function with a full width of half maximum of $b_\omega = 23(\pm 2)^\circ$ [63–65]. From this an upper limit of $\sigma = 10^\circ$ can be estimated for the mean tilting angle of the crystallographic axes of the grains. With calculations from P. Staeck [115] it can be concluded that a tilting of the crystal anisotropy axis could cause a much higher tilting in the effective anisotropy axis of the dot. He found for a tilting of 4° of the crystalline anisotropy a tilting of the easy axis by 26.5°. He assumed a dot with a diameter of 50 nm, a Co thickness of 1 nm, an anisotropy of $K_{1,V} + 2K_S/t_{\mathrm{Co}} = 1.316\,\mathrm{MJ/m^3}$ and a shape anisotropy of $K_{\mathrm{shape,dot}} = 1.516\,\mathrm{MJ/m^3}$. He also assumed that the crystalline contribution and the surface contribution of the anisotropy are tilted in the same direction.

The resulting angle θ for the easy axis was then obtained from a minimization of the total energy with a tilted volume and surface anisotropy regarding to θ (at $\mu_0 H = 0$).
In a simulation of a homogeneous dot (without grains) with tilted anisotropy axis of 8° and the standard simulation parameters, described in the section before, a tilting of the easy axis of 23° was found. Both results can be understood also intuitively in the following way. If all anisotropies except the shape anisotropy were very small, the dot (or grain) magnetization would point in-plane (in equilibrium state without magnetic field). In a system with a stronger perpendicular surface (or crystalline) anisotropy the magnetization points out-of-plane, but it is not possible for the shape anisotropy to induce torque on the magnetization. The situation changes when the crystalline or surface anisotropy axis is tilted. Then it is possible to induce torque by the shape anisotropy, which results in a more tilted easy axis of the combined shape and crystalline (or surface) anisotropy.
The actual value of the tilting of the easy axis depends on the ratio of shape anisotropy and the tilted anisotropy, as well as if it is assumed that the surface anisotropy is tilted in the same way or remains perpendicular to the dot plane. A strong tilting is received for the case of a tilted surface anisotropy and the tilting increases with a higher shape anisotropy contribution [115].
For simplification it is assumed that in all simulations surface and crystalline (volume) anisotropy point in the same direction. This seems also reasonable to enhance the tilting of the easy axis, since strong tilting was found in the experiments. It could be even observed that in some cases the easy axis of the system is tilted by more than 45° as was shown in sect. 5.1.1.

The next step was to implement grains with tilted anisotropy axis with different directions in the simulations. Here it was assumed that the angle in the xy-plane (the plane of the Hall cross) was totally random. The angle with the z-axis, also referred to as θ, was simulated for three different mean values of $8.1(\pm 2.9)°$, $15.7(\pm 5.4)°$ and $22.7(\pm 7.5)°$. They will be referred to as 8°, 16° and 23° since the exact value of tilting does not influence the result significantly. For the 23° case the directions of the anisotropy tilting is depicted in fig 5.10 a). The grain exchange was set to 100% and the anisotropy is distributed as described in the section 5.2.
The resulting hysteresis curves for 8° and 23° are shown in fig 5.10 b). A second jump is clearly visible for 23°. For smaller tilting like 8° and 16° (not shown here) no second jump could be observed, but a certain rotation of the magnetization resulting in a decrease of the m_z component could be seen even in the 8° case.
At 8° tilting the magnetization has a mean angle with the z-axis of 18° ($\mu_0 H = 0$).

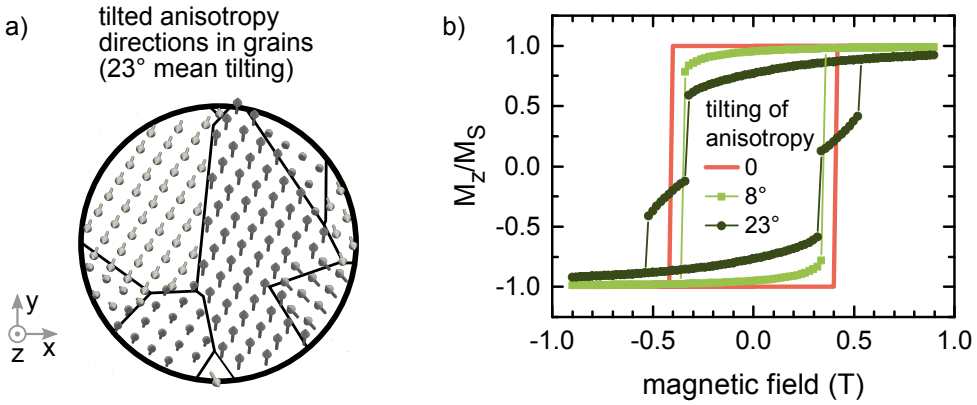

fig 5.10 a) Tilted anisotropy directions in grains of the strong tilting case (23° mean angle with the z-axis). The arrows represent every 350th data point. b) Hysteresis of dot with tilted grain anisotropy, with full grain exchange. The absolute value for the anisotropy has a normal distribution with a width of 10% of the initial value. Two different degrees of tilting are shown and compared to a hysteresis without tilting. The switching fields are 0.41 T for no tilting. For 8° tilting of the anisotropy from the z-axis the switching field is ±0.35 T. For an mean tilting of 23° a second jump in the hysteresis curves occurs. The first is at ±0.33 T and the second at ±0.53 T. The corresponding magnetization states are shown in fig 5.11.

The magnetization is not entirely uniform at zero field. The absolute value of the averaged normalized magnetization, which is a measure for the conformation of the magnetization, is 0.97 [6] at zero field. This non-uniformity increases before the switching as can be seen in fig 5.11.

With a mean tilting of the anisotropy axes in the grains of 23°, the magnetization has a mean angle of 29° (at $\mu_0 H = 0$). The absolute value of the averaged normalized magnetization is 0.85, which is, as expected, smaller than in the 8° case. When a field is applied in opposite direction of the m_z component, the magnetization rotates also in-plane and first switches at 0.33 T (see fig 5.10 b) and fig 5.11). The signal height is roughly $\frac{1}{3}$ of the total amplitude. Then in the intermediate state, before the second jump, a further rotation becomes visible in the hysteresis curve. The second jump at 0.53 T has only $\frac{1}{4}$ of the total m_z amplitude. After the second jump the z-component of the magnetization is still not entirely saturated and rotates further as the magnetic field is increased.

In the next section the energy contributions received from the simulation and the magnetization states of the weak and strong tilting case will be discussed in more detail.

[6] When all magnetic moments are parallel, the normalized magnetization is 1. Different angles between the magnetic moments result in a reduced absolute value of the averaged dot magnetization.

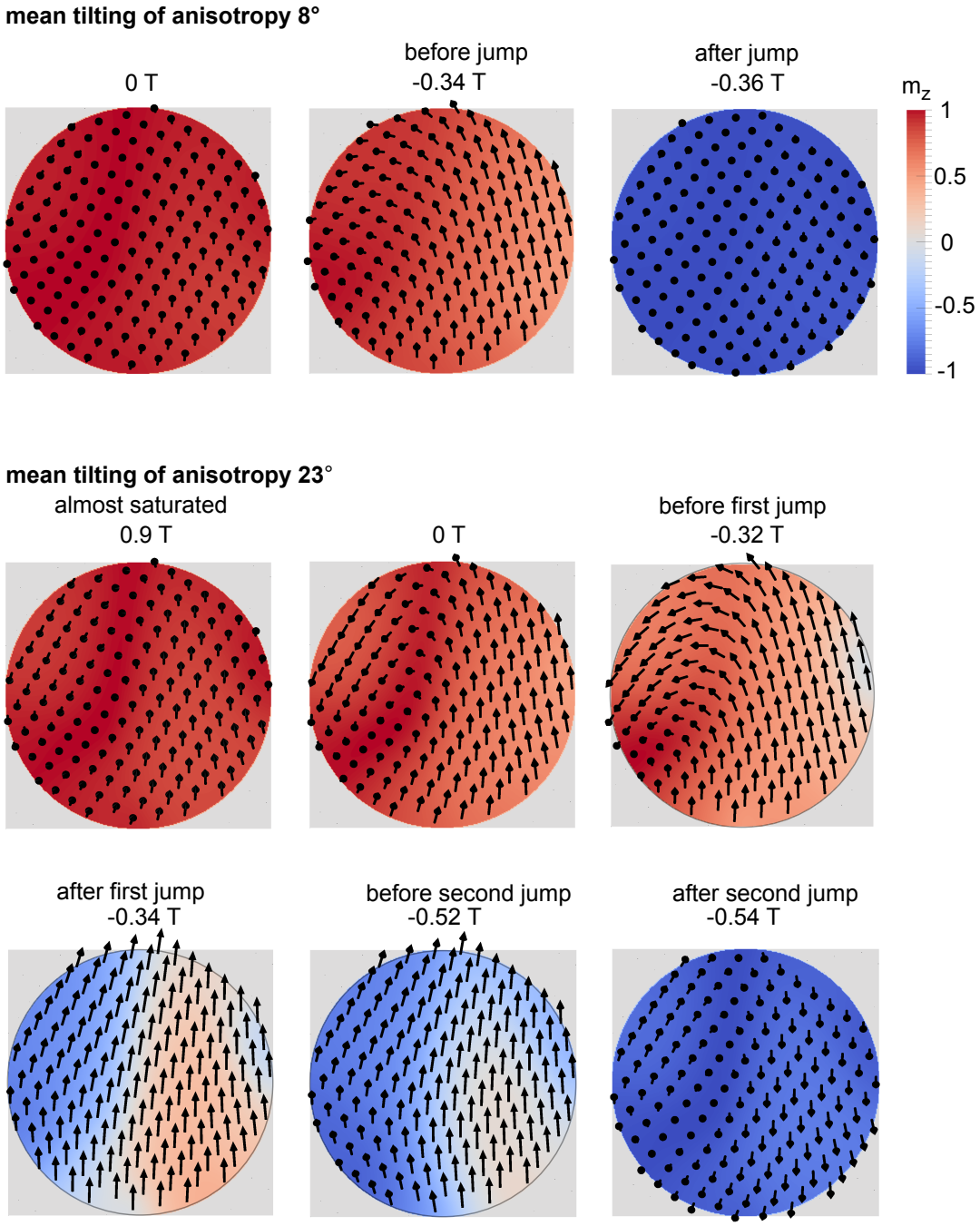

fig 5.11 Magnetization states of a dot with 9 grains. Two different tilting cases are shown. The m_Z component is given as a color code. Red corresponds to +1 and blue to -1. Grey areas represent an $m_Z = 0$. The full magnetization vector is depicted as 3 dimensional black arrows. Every 350th data point is represented by one arrow. If the magnetization is pointing entirely up or down, the two dimensional image of the 3D arrows gives circles. The arrows begin in the area they represent, resulting in a rather odd behavior of arrow tips ending outside the simulated structure. This is an artifact of the used visualization software and has to be kept in mind when interpreting the magnetization, but will not influence any conclusions drawn. For some of the configurations with strong in-plane component a small dark gray ring is added, in order to separate the dot shape from the gray background. The anisotropy directions in the grains are shown in fig 5.10 a) and the strength of the anisotropy distribution in fig 5.6.

Energy contributions

The energy contributions are displayed in fig 5.12. The magnetic field is set to 1 T and then decreased in small steps to −1 T, only half of the magnetic field loop is depicted. The demagnetization and anisotropy energy are no longer constant for the tilted grains. As the easy axis of the grains is no longer perpendicular to the film plane and thus not collinear with the applied magnetic field.

When the magnetic field is decreased from 1 T, the magnetic moments start to rotate slowly towards their local easy axis. When negative fields are applied, they start to rotate away again from the local easy axis. This rotation away from the local easy axis causes a change in the anisotropy energy. For the low tilting case (8°) the anisotropy energy has a maximum right before the jump in the hysteresis curve in fig 5.10 b). Here the magnetization has a maximum angle from the local easy axis. After the jump this angle is very small again. Throughout this rotation also the demagnetization energy is reduced, since the in-plane component of the magnetization becomes much larger and less (virtual) magnetic surface charge is produced (cp fig 5.11). After the jump the magnetization has a larger z-component again, thus the demagnetization is almost to back to the intial value. Furthermore the magnetization component anti-parallel to the field becomes smaller in this rotation. Thus also the Zeeman energy is not linear anymore and slightly smaller right before the jump than in the case without tilted grains. Only very small increases appear in the exchange energy. In total for smaller fields (opposite to the magnetization) the sum of all energies (fig 5.13) is slightly reduced compared to a uniform magnetization state.
For the stronger tilting case (23°), a second jump becomes also visible in all energy terms. Before the first jump the situation is very similar to the low tilting case. The deviations from a dot with entirely perpendicular anisotropy axis are more pronounced since the magnetization has a higher in-plane component. The demagnetization energy is a little more decreased, probably due to a certain degree of flux closure that can be observed in fig 5.11. After the first jump and before the second jump the demagnetization energy is further reduced, because the magnetization has a very strong in-plane component (see fig 5.11, gray implies total in-plane magnetization, light red and light blue almost in-plane). Also the Zeeman energy is reduced after the first jump, since some part of the magnetization has a component in field direction (blue area in fig 5.11). The magnetization rotates further between first and second jump into the field direction, which can be seen in the decreased red and increased blue area.

The exchange energy is slightly increased before the first jump and surprisingly decreased afterwards. It would be expected that a nonuniform state between first and second jump would lead to a further increase, but a look at the magnetization state in fig 5.11 shows, that in both tilting cases the magnetization actually appears more uniform after the first jump in the hysteresis curve.
However for the strong tilting case the more coherent states costs anisotropy energy, since the magnetic moments are forced to rotate the most away from their local easy axis. A further decrease of the field then results in a second jump and a switched magnetization, but not fully saturated configuration, some moments are still slightly rotated away from the direction of the applied magnetic field.
The total energy of the strong tilting case in fig 5.13) appears before the first jump (in negative fields) lower than in the cases with small or no tilting. However the intermediate state between the two jumps requires more energy. Also after the second jump the energy is slightly above the other curve, since the magnetization is rotated away from the local easy axis.

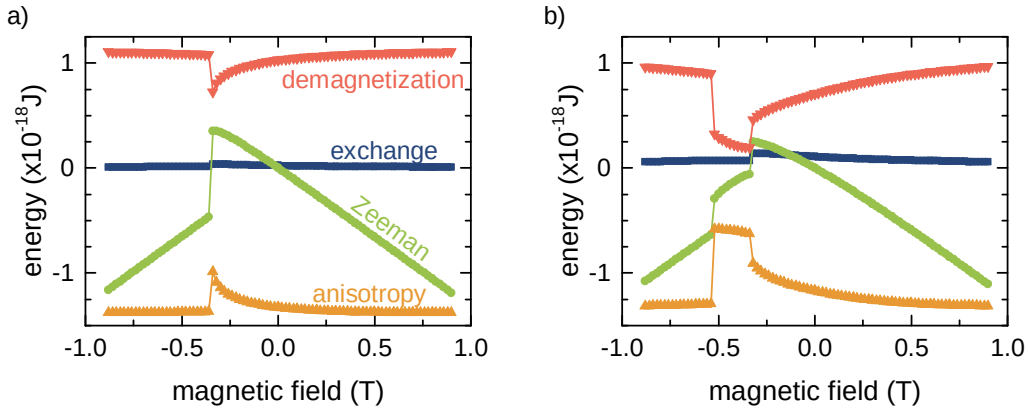

fig 5.12 Energy contributions for different tilting angles of the anisotropy axes. Exchange, anisotropy and demagnetization energy are not constant anymore as in the case of a dot without tilted grains (fig 5.9). a) At a tilting of 8° the hysteresis curve shows one jump. But the reversal process is already incoherent. This is visible also in small changes of the exchange energy. Anisotropy and demagnetization energy change due to rotation of the magnetization towards in-plane direction. b) At 23° a second jump occurs in the hysteresis curve. The exchange energy increases a little. The changes in anisotropy and demagnetization energy are more significant. The Zeeman energy is reduced within the reversal process.

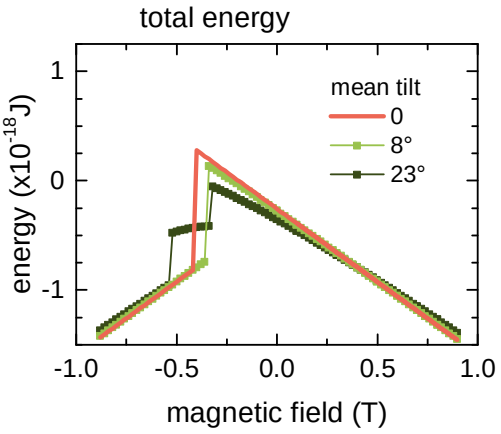

fig 5.13 Total energy of the weak tilting, strong tilt case and without tilt. The curves are the sum of the curves in fig 5.12 a) and b) and fig 5.9 a).

In this section it was shown, that indeed a tilting of the anisotropy axes in different directions in the grains of the nanodot can result in non-coherent switching with two jumps in the hysteresis curve, even with full exchange interaction between the grains. The resulting magnetization states and the energy terms were shown and discussed. As a next step a simplified two grain model will be introduced in the following section to learn more about the non-coherent reversal process.

5.3 Simulations with a simplified two grain model

In order to better understand the appearance of a second jump in the hysteresis curves a more simple model with 2 grains is introduced. The geometry is shown in fig 5.14. The dot is divided in two regions with different size. These regions represent two large grains. Three different main configurations (1-3) for the direction of the anisotropy in the grains are assumed, each of them with different degrees of tilting. The exchange interaction between the grains was set to 10%. In contrast to the multigrain simulation here a constant anisotropy value was assumed, since no qualitative differences in the switching behavior could be observed in the multigrain simulation.

5.3.1 Opposite tilting directions: configuration 1

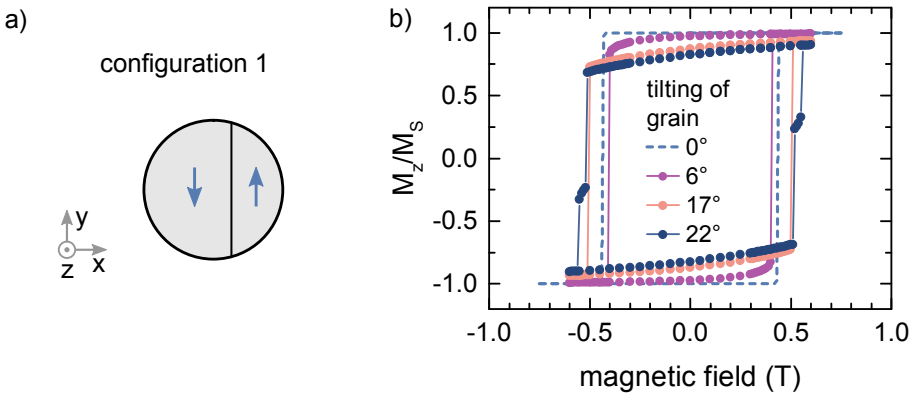

fig 5.14 Simplified two grain model. a) tilting in configuration 1. The anisotropy axes are tilted in two opposite directions parallel to the grain boundary. b) resulting hysteresis curves for different tilting angles. For a tilting of 22° a second jump appears in the hysteresis. The magnetization states for 6° and 22° are shown in fig 5.15.

In a first attempt the magnetocrystalline axis was tilted from the out-of-plane direction by 6° in opposite directions as depicted in fig 5.14 a). The tilt was increased for each simulation up to 22°. Already for 6° a deviation from the ideal squared SW hysteresis shape can be observed. The z-component of the magnetization at 0 T becomes smaller for stronger tilting and it decreases if a magnetic field is applied in opposite direction of the magnetization, which is characteristic for a rotation of the magnetization. At a certain field a jump appears in the hysteresis curve, which corresponds to the actual switching of the magnetization.

At a tilting of 22° a second jump appears in the hysteresis curve, the first jump becomes smaller and in between the two jumps another intermediate magnetization state occurs. The relaxed magnetization states and the states right before and after the jumps are displayed in fig 5.15 for small tilting (6°) and strong tilting with two jumps (22°).
Here it becomes visible, that the rotation, observed in the hysteresis curve before switching of the small tilting case, is mainly a rotation of the left grain. Actually in the relaxed state (with $\mu_0 H = 0$) the magnetization in the left grain has an angle 19° with the z-axis on the left edge and it rotates to 4° at the grain boundary. In the right grain the magnetization is perpendicular near the boundary and rotates to 12° at the right edge. Right before the jump in the hysteresis curve, the tilting in the left grain increases to 51° on the left edge. The magnetization of the rigth grain is almost unaltered. After the switching the magnetization is almost saturated and aligned with the field.
For the strongly tilted case (22°), the actual tilting of the average magnetization, after relaxation in zero field, is 38° in the left and 27° in the right region of the dot. But the magnetization in each region is far from uniform (see fig 5.15). The maximum angle of the magnetization is 46° at the left and 39° at the right edge of the dot. In between a kind of Bloch domain wall[7] is formed with a reduced angle of 85° (instead of 180°). Due to the reduced grain exchange, the wall does not exhibit a continuous rotation of the moments. The highest angles between the moments are concentrated near the grain boundary (±10 nm). Wall profiles corresponding to the magnetization states in fig 5.15 (for 22°) are shown in fig 5.16. Here a clear discontinuity can be seen at the grain boundary.
The maximum angle between the moments increases as a negative magnetic field is applied (see — curve fig 5.16). At a certain field strength it is more favorable for the magnetization of the right grain to switch to a negative m_z value and therefore decrease the angle with the left domain (— wall profile). Then the magnetization of the left grain rotates further in-plane until with a more increased field also the left grain switches, which gives the second jump in the hysteresis curve. If we interpret this configuration as a Bloch wall with reduced angle, the applied field increases the angle of the two ends of the Bloch wall. The Bloch wall is strongly pinned at the grain boundary due to local configuration of the anisotropy directions.

[7] the magnetization rotates around the domain wall direction (here in x-axis), it is always perpendicular to this direction [66].

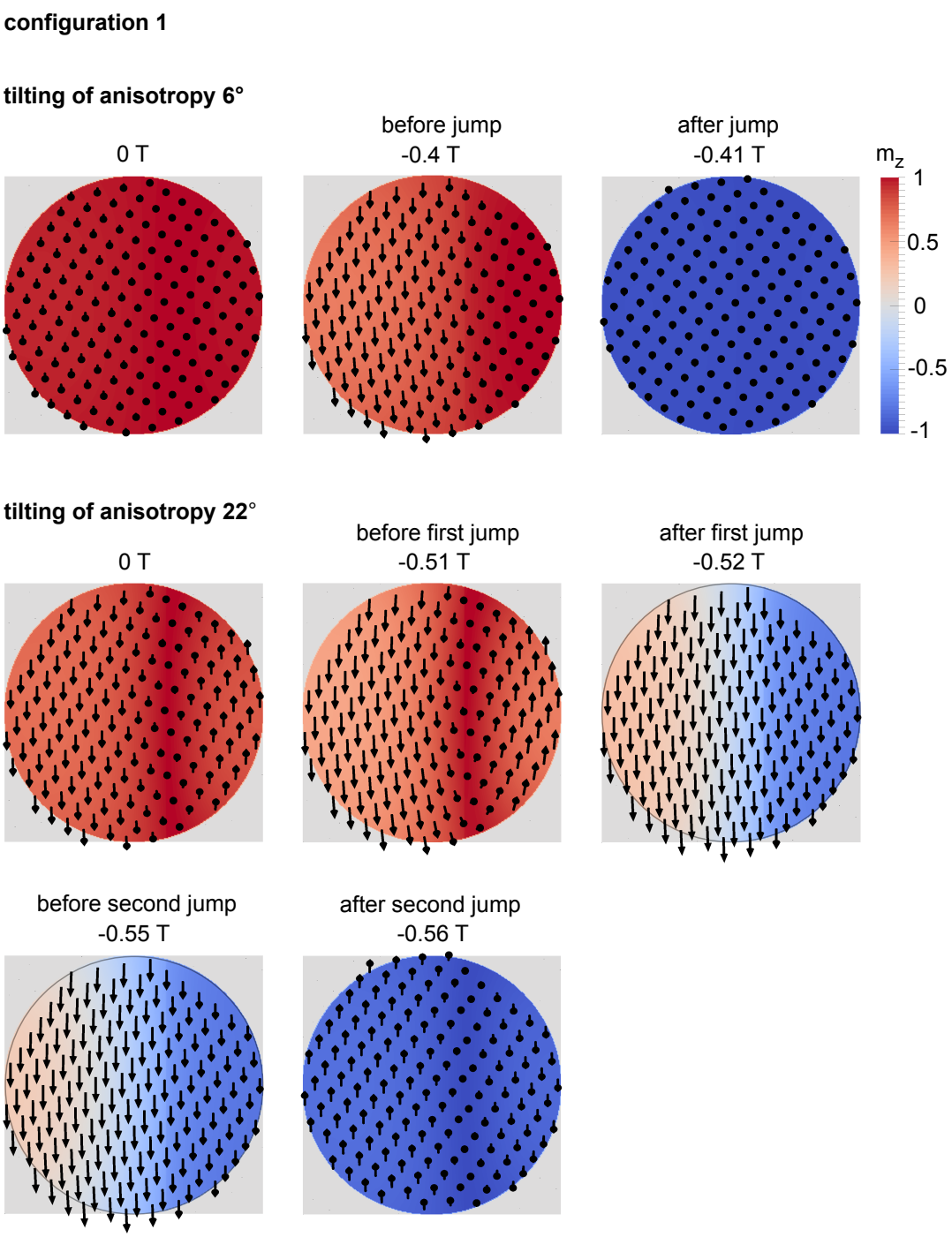

fig 5.15 Magnetization of a simplified two grain model with configuration 1. Two different tilts of the anisotropy axes are shown. A weak tilting case (6°) and the stronger tilting case (23°) for which a second jump in the hysteresis curve is found. The red blue color code represents the normalized m_z component. The black arrows represent the 3D magnetization vector. More detailed description about the illustrations can be found in fig 5.11.

At certain fields (which correspond to the jumps in the hysteresis curves) a change of one end of the domain wall results in a different twisting direction of the Bloch wall. Only in very high fields (not shown here) a uniform magnetization is expected.

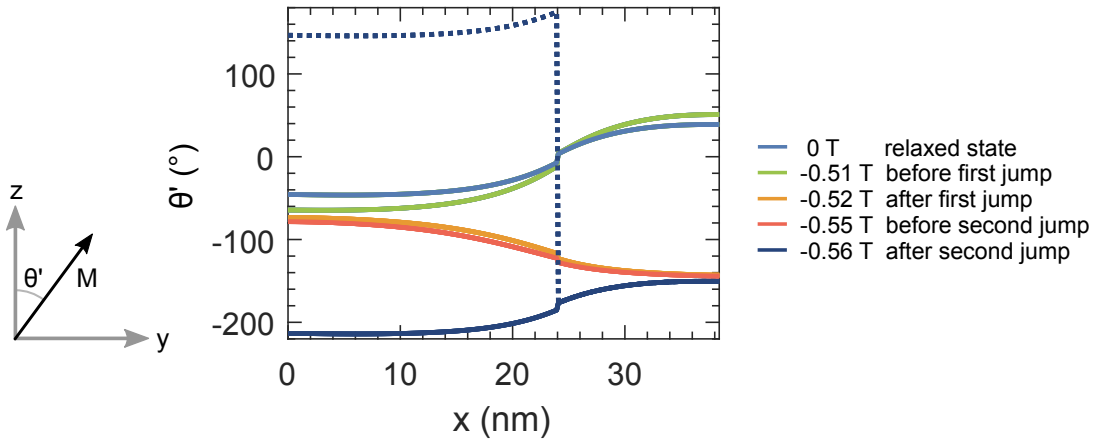

fig 5.16 Domain wall profiles of the magnetization states depicted in 5.15 with configuration 1 and 22° tilting of the anisotropy axes. The profiles are taken along the x-axis through the middle of the dot. The profiles show the relaxed state, as well as before and after the first and second jump in the corresponding hysteresis curve of fig 5.14. At the grain boundary a discontinuity appears in all profiles. The wall is pinned. The dotted line represents the original data after the second jump with the conventions for the angle θ' shown in the sketch on the left. However it is advantageous here to switch to another equivalent representation by subtracting 360° of the data for the left grain (continuous dark blue line).

Variation of exchange

In order to study the discontinuities of the angles (of the magnetization with the z-axis), which were observed at the grain boundary in fig 5.16, simulations with different grain exchange are discussed here. Only domain wall profiles of the relaxed magnetization are shown in fig 5.17 a). The switching process is for all grain exchange values very similar to the process discussed in the previous section, except of the case with zero grain exchange, which is not very likely for the measured nanodots. The grain exchange influences the angle of the magnetization in the right grain. The angle with the z-axis becomes slightly increased with smaller grain exchange. The discontinuity in the magnetization angle near the grain boundary increases with smaller grain exchange. The extension of the wall however becomes smaller with reduced grain exchange and infinite narrow at zero

grain exchange.
The wall profile for full grain exchange can be described by a Bloch wall model [66] which is modified:

$$\theta'(x) = a \cdot \arctan\left[\sinh\left(\frac{\pi(x - x_0)}{\delta_{\mathrm{DW}}}\right)\right] + \theta_0 \tag{5.1}$$

$a \cdot 180°$ gives the maximum angle of the domain wall (in °), x_0 the position of the wall middle (which is shifted from x=0) and θ_0 is a measure for the asymmetry and necessary since the size of the grains is not equal and thus the system not symmetric to the z-axis. The Bloch wall width $\delta_{\mathrm{DW}} = \pi\sqrt{\frac{A}{K}}$ with A the exchange constant in the grains and K which is the anisotropy constant. δ_{DW} is taken here as a fit parameter however and the actual domain wall width is smaller in the systems with reduced grain exchange due to the discontinuity at the grain boundary.

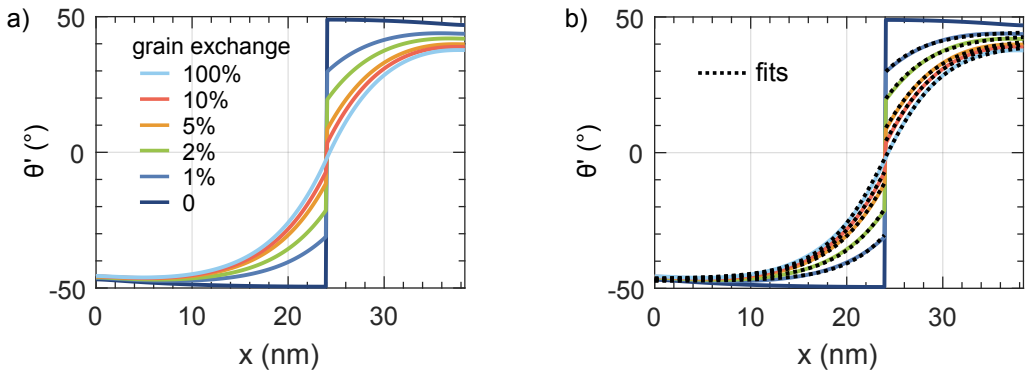

fig 5.17 a) Domain wall profiles of configuration 1 with a tilting of 22° at 0 T along the x-axis in the middle of the dot with different values for the grain exchange. The angle θ' is defined in the yz-plane as depicted in 5.16. For full grain exchange the wall profile is smooth. While for smaller grain exchange the angle variation is not continuous anymore. With the decrease in grain exchange the discontinuity at the grain boundary becomes higher. Without grain exchange however θ' is also not constant within the grains. This is caused most likely by stray field optimization. The 10% data is from the same simulation as in 5.15, all other data is from simulations not discussed further. b) The domain wall profiles can be fitted with modified Bloch wall profiles as described by equation 5.2.

It is also a bit unclear how K is defined in the fit, since the direction of the anisotropy is not constant throughout the extension of the Bloch wall.
For all fits with reduced grain exchange the domain wall profile is fitted piecewise in the following way: The values of the left grain were shifted in the x-direction

by x_1. The values of the right grain were also shifted by another value x_2. Both shifts were used as additional fit parameter and then compensated in the actual plot. All other parameters were applied to the whole x range:

$$\theta'(x) = \begin{cases} a \cdot \arctan\left[\sinh\left(\frac{\pi(x-x_1)}{\delta_{\mathrm{DW}}}\right)\right] + \theta_0 & x < \text{grain boundary} \\ a \cdot \arctan\left[\sinh\left(\frac{\pi(x-x_2)}{\delta_{\mathrm{DW}}}\right)\right] + \theta_0 & x > \text{grain boundary} \end{cases} \tag{5.2}$$

The fits are shown in fig 5.17 b). The system can be described very well by the modified Bloch wall profile. Only for zero grain exchange it is not possible to achieve a good fit.
A similar discontinuity in domain walls was found also by Skomski et al. in an analytical calculation of two grains with reduced grain boundary exchange [190]. No further details will be discussed here however, as configuration 3 seemed to be more promising since these hysteresis curves resembled the most to the measurements. Before we come to configuration 3, configuration 2 will be discussed for completeness. However no second jump could be observed in the hysteresis curves of this configuration.

5.3.2 Right angle tilting: configuration 2

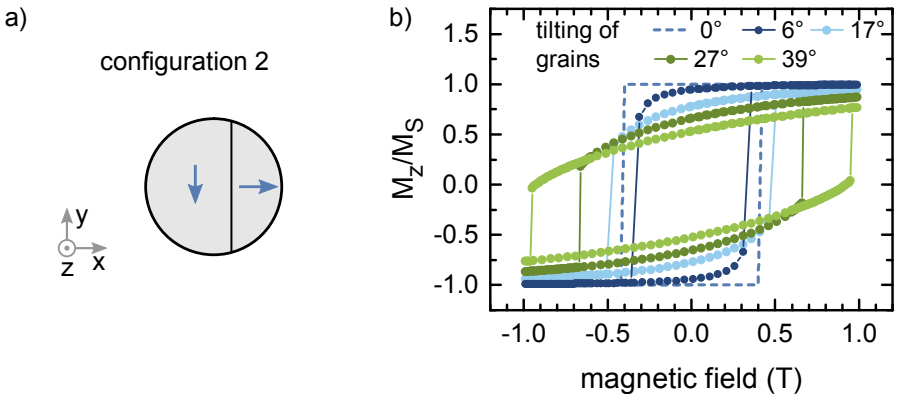

fig 5.18 Simplified two grain model, a) tilting configuration 2. The anisotropy axes are tilted in perpendicular directions. The left grain has an in-plane component parallel to the grain boundary. b) Resulting hysteresis curves for different tilting angles. Even for strong tilting, such as 39° only strong rotation and one jump appeared. The magnetization states for weak and strong tilting can be found in fig 5.19.

A second approach was to alter the tilting direction of the magnetocrystalline anisotropy of the right grain by 90° (fig 5.18 a)). Here the magnetization is also tilted at zero field and rotates further when a field is applied in the opposite direction (fig 5.18 b) and fig 5.19). In this case also for very strong tilting of 39° with the z-axis no second jump could be observed in the hysteresis curves (fig 5.18 b)), but the hysteresis curves are strongly distorted.
The magnetization states are depicted in fig 5.19. The magnetization is not uniform but the angles between the magnetic moments of the left and right grain stay more or less constant through the switching process. The 39° tilt resulted in an angle of the relaxed magnetization with the z-axis of 57° for the left and 58° for right grain (fig 5.19). Also this angle with the z-axis increases with an applied field and remains almost constant within the dot.
The example of configuration 2 shows that it is relevant in which directions the anisotropy axes are tilted. Here the angles between the moments seems to stay almost constant, the magnetization of the two regions is not twisted against each other by the applied magnetic field and thus the field induced torque acts on both grains equally. Compared to configuration 1 the magnetization rotates more and both grains switch together.

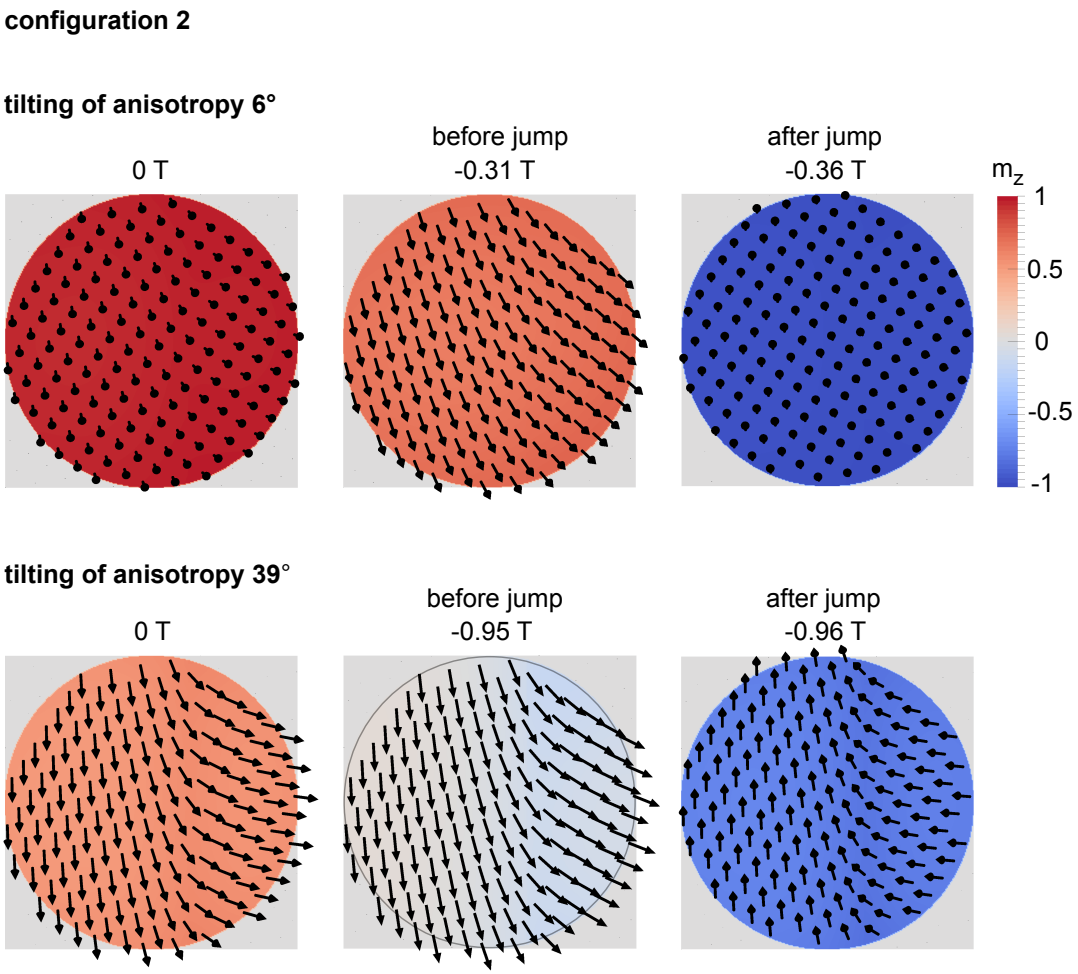

fig 5.19 Magnetization for a simplified two grain model with configuration 2. A weak and a very strong tilting case are depicted. Both show incoherent switching but this non-uniformity of the magnetization remains almost the same and rotates only. No second jump appears in the hysteresis curves of fig 5.18 b). The weak tilting case shows a more coherent magnetization than the the strong tilting case. The red blue color code represents the normalized m_z component, the black arrows the 3D magnetization vector. More detailed description about the illustrations of the magnetization states in general can be found in fig 5.11

5.3.3 One tilted grain: configuration 3

In the configuration 3 only the anisotropy direction of the right smaller grain of the dot was tilted as shown in fig 5.20 a). This configuration is a simplified model for a dot with one or more grains that have a tilted anisotropy axis and other grains with a magnetocrystalline axis in z-direction. The resulting hysteresis curves are displayed in fig 5.20 b) and c).

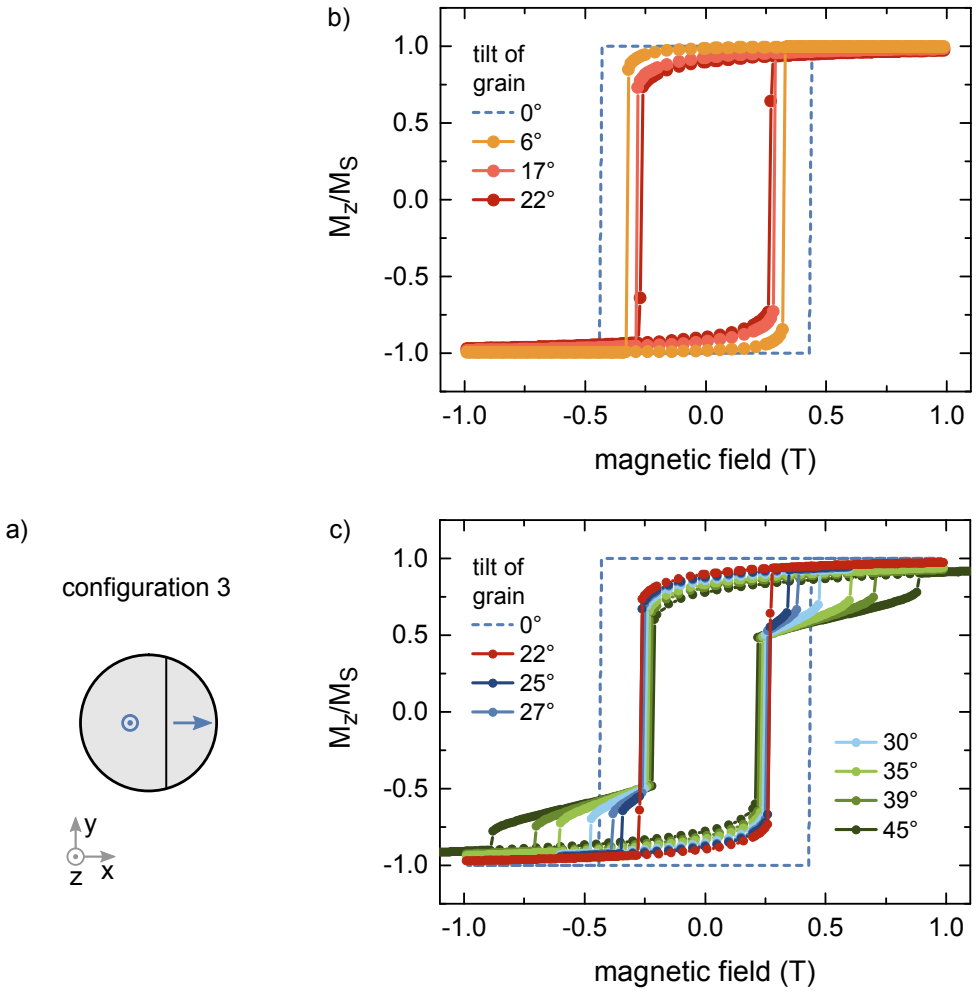

fig 5.20 Simplified two grain model with one tilted grain: configuration 3. a) sketch of the tilting direction. The anisotropy axes of the right grain are tilted in x-direction. b) Hysteresis curves for smaller tilting angles. At 22° a second jump appears in the hysteresis curve. c) For more tilting the switching field of the the first jump decreases slightly and the switching field of the second jump increases significantly.

For increasing tilt the z-component of the remanent magnetization is reduced and with the applied opposite magnetic field the m_z component of magnetization decreases further. At the steepest point the magnetization switches and a jump occurs in the hysteresis curve. The switching fields become lower with higher tilting.
Until at 22° an intermediate configuration appears at 0.27 T, that divides the jump into two parts. For further tilting the switching field of the first jump becomes slightly smaller and the second jump appears at increasing fields. For tilting of 30° and more, the second jump happens even at higher fields (0.475 T) than in the system without tilting (0.435 T). In the intermediate state between the two jumps a further rotational change in the magnetization takes place.

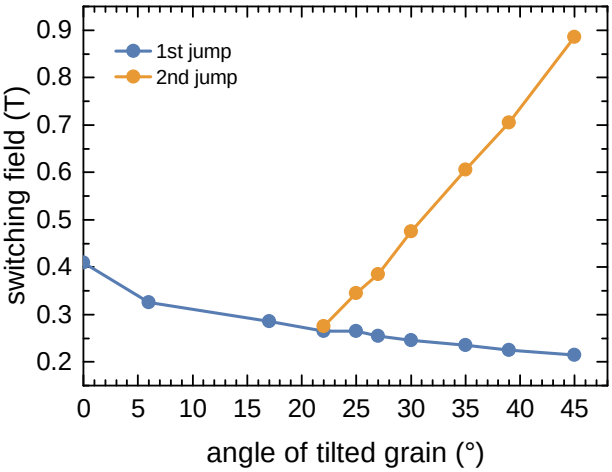

fig 5.21 Switching field of the first and second jump of the simulated hysteresis curves in fig 5.20 b) and c).

The switching field of the first and second jump over the tilting angle of the anisotropy are shown in fig 5.21. The switching field decreases with increasing tilting angle until at 22° a second jump appears that increases with the tilting angle.
A similar behaviour was found in the experiments for the switching field over temperature (fig 5.3). First at higher temperatures only one jump can be observed. Then with lower temperatures a second jump appears in the hysteresis curve. Decreasing the temperatures further a strong increase of the second jump switching field (except for values below 20 K) was found. The first jump however shows only a slight increase in the measurements. This comparison of the simulated hysteresis

curves with increasing tilting with the measured hysteresis curves in fig 5.1 gives rise to the assumption that a decrease in temperature might increase the tilting of the anisotropy axes. The only deviation from the simulation is the small increase with lower temperatures of the first switching field in the measurements. Probably this increase can be explained by the change in temperature that dominates over the small decrease that would be caused by the higher tilting of the magnetization. Also temperature is not included in the simulation, since they all assume $T = 0\,\mathrm{K}$.
A good explanation for the stronger tilting of the anisotropy axis could be the increase of the amount of magnetic material contributing with lower temperatures. This effect is discussed in detail in the PhD thesis of Freercks [131] and an article in preparation [132]. Here a quick summary will be given:
The interface in the film system and therefore also in the dots is not discrete but a inter-diffusive zone where an alloy of Co and Pt forms. This alloy has a continuous change in Co concentration. In a PtCo alloy the Curie temperature is reduced with decreasing Co concentration [161]. That is the reason why as soon as the temperature is decreased also the parts of the alloy with a lower Co concentration become ferromagnetic and thus the effective magnetic material of the dot becomes thicker.
In other words, the film system consists of a Co layer and two inter-diffusive zones. The effective Co layer is thinner than the nominal Co thickness of the sputtered film. Additionally a part of the inter-diffusive zones contributes to the magnetization, the thickness of this part is temperature dependent. With higher temperatures it becomes thinner. Then also the saturation magnetization of that part of the inter-diffusive zone becomes smaller for higher temperatures. This decrease in saturation magnetization is much higher than expected from Bloch's $T^{3/2}$ law. As a consequence also the shape anisotropy is reduced significantly for higher temperatures (it depends on M_S^2). Therefore if we go to lower temperatures the influence of the shape anisotropy increases. If the local anisotropy axis in a grain is already tilted this might result in even stronger tilting for lower temperatures, which would explain the experimental results very well.
Indeed there is a change of the angle of the hard axis in fig 5.5. It is less tilted for higher temperatures. But the direction of the easy axis is not entirely clear. And in the case of more coherent switching in fig 4.6 the easy axis is even more tilted for 80 K than 2 K. On the other hand the hard axis is slightly less tilted for higher temperatures of that dot, which results in deviation of the expected 90° angle between hard and easy axis.

One can imagine that also elevated temperature might provide enough thermal energy to overcome the energetic barrier between first and second jump.

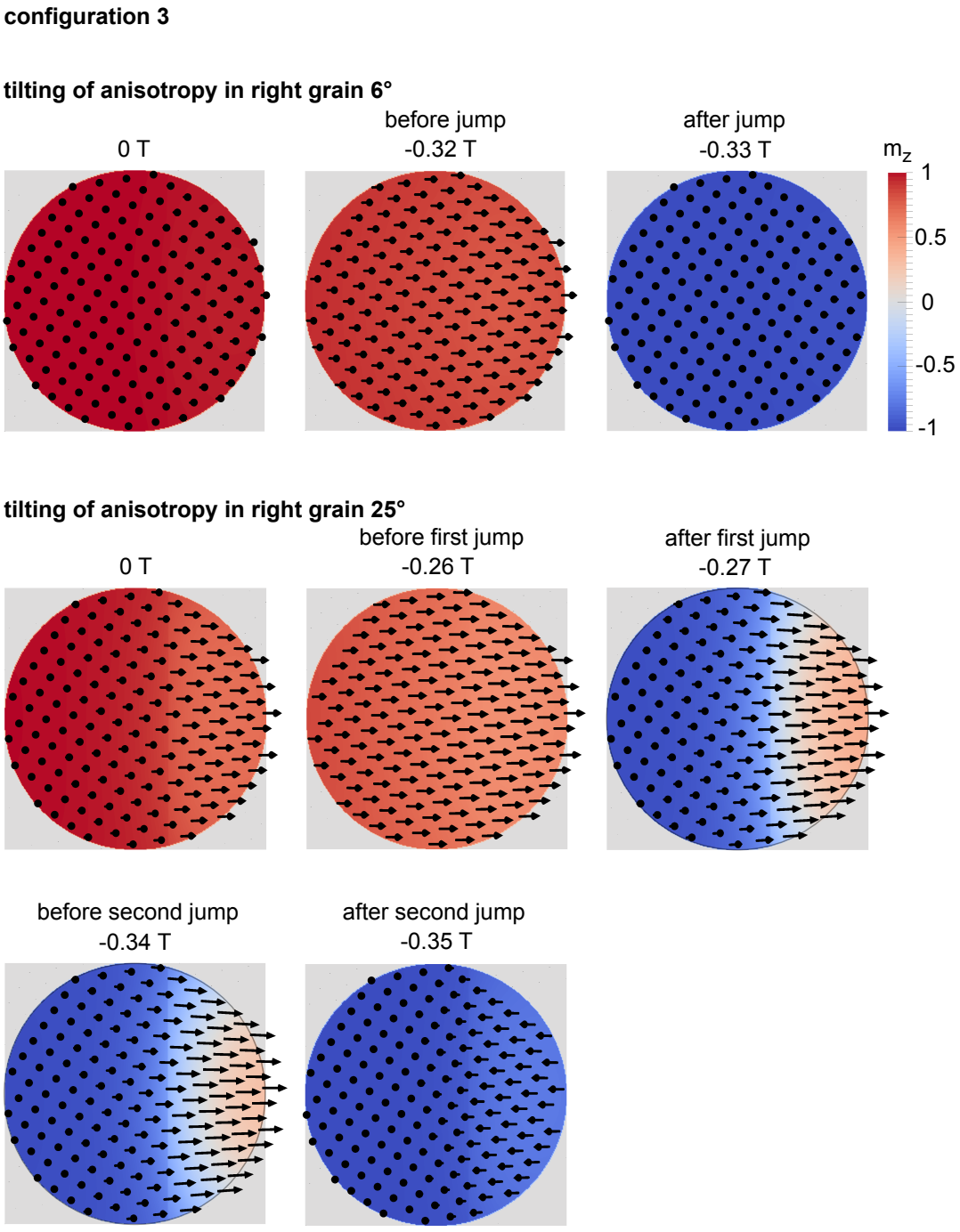

fig 5.22 Magnetization states of two examples with slight and strong tilting of the simulated hysteresis curves in 5.20 (configuration 3). The red blue color code represents the normalized m_z component, the black arrows the 3D magnetization vector. More detailed description about the illustrations can be found in fig 5.11. The first example is a tilting of the anisotropy of 6° in the right grain (and no tilting in the left grain). The magnetization appears almost coherent throughout the switching process at a closer look it becomes visible that there is slight a gradient in size of the in-plane component. It is larger on the right of the dot than on the left.

continuing caption fig 5.22: For a stronger tilting of 25° of the right grain the magnetization is less coherent. In the relaxed state at 0 T the right grain has a much stronger in-plane component pointing in x-direction (cp conventions in fig 5.20 a)) while the left grain remains almost perpendicular. Near the grain boundary an almost continuous transition appears. When a field is applied the configuration becomes more coherent, the moments of the left grain rotate into the direction of the right grain, that also rotate more in x-direction. Still a gradient is visible though. Between −0.26 T and −0.27 T the first jump in the hysteresis curve appears and the magnetization of the left grain switches in field direction. The magnetization of the right grain is still in-plane with an out-of-plane direction anti-parallel to the field. With increasing fields the magnetization of the right grain rotates further in-plane. Between −0.34 T and −0.35 T the second jump appears and, in contrary to configuration 1, the left grain switches first. An in-plane component remains after the second jump, that is now reversed to before. In order to enhance the dot shape from the background in images with strong in-plane component, a small gray ring is added to the drawing in two of the images.

The magnetization states of configuration 3 are depicted in fig 5.22. After relaxation of the magnetization at 0 T, the magnetization appears almost uniform in z-direction for the low tilting case of 6°. But the magnetization has a slightly bigger in-plane component on the outer edge of the tilted grain (on the right) than the left grain. With a magnetic field applied in -z-direction the magnetization rotates towards in-plane and is still almost coherent before the switching at −0.32 T. The magnetization of the tilted grain has still a slightly larger in-plane component. After the switching the magnetization is saturated and entirely pointing along the magnetic field direction. This can be brought in accordance with the hysteresis curve in fig 5.20 b) where the magnetization is almost saturated after the switching.

For stronger tilting like the 25° case the reversal of the magnetization is different. The directions of the relaxed magnetization at 0 T is clearly inhomogeneous. In the left grain the magnetic moments point up, but reveal a gradually growing in-plane component close to the grain boundary. The magnetization in the right grain has a clear in-plane component.
As in the case of configuration 1 this magnetization transition near the grain boundary can be interpreted as domain wall with strongly reduced angle. The corresponding wall profile of the simulation is shown in fig 5.23 (▬ curve). At the left edge of the grain the angle of the magnetization with the z-axis is 7°. The y-component of the magnetization is negligible, thus the angle θ'' is defined now as the angle with the z-axis in the xz-plane (see sketch in fig 5.23). It rotates than to 32.5° at the grain boundary. Here as in configuration 1 a discontinuity

due to the reduced grain exchange is found. The angle jumps by 4° to 36.5° and rotates then further to 47° in the right grain. A very small decrease (<1°) can be observed at the very right edge. It is not entirely clear why this is the case, maybe this change is caused by stray field optimization and the circular shape of the dot. If we treat this magnetization state as a domain wall, we have a wall angle of 40°. Since the magnetization rotates towards the direction perpendicular to the domain wall (here the x-axis) we could interpret this as a Néel wall with a reduced angle [66].

With an applied magnetic field also the magnetization of the left grain rotates towards the magnetization of the right grain. Right before the first jump the magnetization looks rather homogeneous, but a gradual transition in the strength of the in-plane component remains. The (wall) profile (curve, fig 5.23) reveals at the left edge an angle of $\theta'' = 33°$ between the magnetization and the z-axis. The magnetization then rotates to 54° near the grain boundary, a small discontinuity of ∼1° can be observed at the grain boundary and stays then almost constant at 55°. Thus the total angle variation is 22°.

After the first jump in the hysteresis curve at −0.27 T the magnetization of the left grain points down (-z-direction) with an increasing in-plane component near the grain boundary. In the right grain the magnetization near the boundary is almost in-plane with a growing up component towards the outer right edge of the dot. From the domain wall profile (curve, fig 5.23) the angles can be deduced. At the left grain edge the angle is 172°, the magnetization is close to -z-direction and the magnetization rotates to 117° at the grain boundary. The discontinuity is 10° and the magnetization of the right grain near the grain boundary has an angle of 107° and rotates to 66° at the right edge of the dot. In total the angle of this wall is 106°.

With increasing magnetic fields the magnetization in the tilted right grain rotates further in-plane. The total angle of the wall reduces than to 100° (curve, fig 5.23). This rotation is observed in the hysteresis curves in fig 5.20 c) too. Finally also the right grain switches and right after the last switching at −0.35 T the magnetization points down but is still tilted in the right grain. The magnetization state is very similar to the state at the beginning, but rotated by 175° (see curve, fig 5.23) and the total variation of the angle from left to right is 36° only due to the applied field.

Also in the intermediate (between the two jumps in the hysteresis) and in the final state the magnetization state can be interpreted as a Néel type wall with an reduced rotation angle of 36° up to 106° and an angle discontinuity at the grain

boundary.
Compared to the Bloch wall type in configuration 1 the Néel wall is slightly wider. The reason for this are volume charges which the systems tries to spread over a wider area. In configuration 1 the anisotropy axes in both grains are tilted. Therefore 22° tilting of the anisotropy axis gives a total angle of 44° between the axes. In configuration 3 only the right grain is tilted. Therefore the total angle between left and right grain is only 25° in the case described here. The tilting angles should not be confused with the wall angles however. The angle of the Bloch wall in configuration 1 is 85° in zero field and thus also double of the angle in configuration 3.
As in configuration 1 the Néel wall is strongly pinned to the grain boundary where the anisotropy landscape changes. In configuration 3 the left grain with a perpendicular local anisotropy axis switches before the tilted right grain. In configuration 1 the situation is opposite, the smaller right grain switches first. But in both cases the grain, whose magnetization has also a smaller tilting angle with the z-axis, switches first.

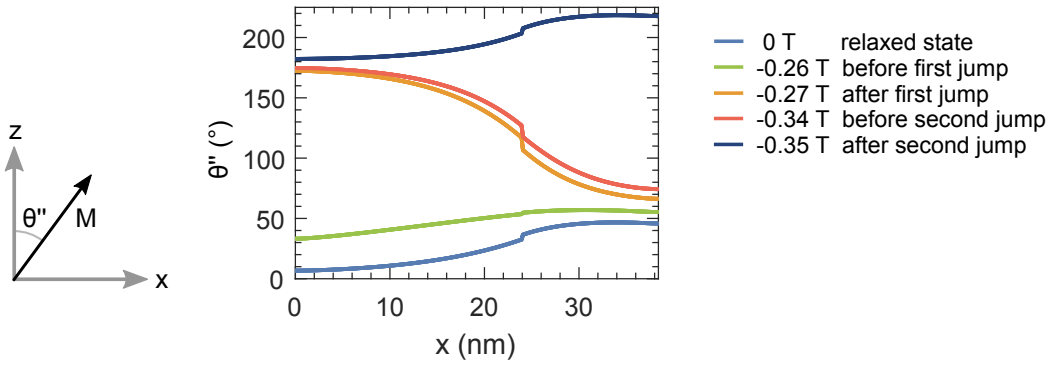

fig 5.23 Wall profiles for the magnetization states of the 25° tilting case of configuration 3 shown in fig 5.22. The angle of the magnetization in the xz-plane is plotted over the x-coordinate. The y-component of the magnetization is negligible. Again as in the case of configuration 1 (fig 5.16) discontinuities are visible at the grain boundary. Before the first jump the magnetization is the most coherent.

Energy terms

In fig 5.24 the demagnetization, exchange, Zeeman and anisotropy energy are plotted over the magnetic field for 4 increasing tilts of the anisotropy axis in configuration 3.
For small tilting the exchange energy seems to be constant near zero. With the appearance of a second jump in the hysteresis curves (fig 5.20 b) and c)) and therefore an intermediate magnetization state, an increase in exchange occurs. This is also in accordance with magnetization states, depicted in fig 5.22, and the wall profiles in fig 5.23, described in the previous paragraph, where a high total change in the angle of the magnetization from left to right of $\sim$100° is found.
The demagnetization energy is reduced with an applied magnetic field (in opposite direction to the magnetization) until the first jump, this corresponds to the magnetization rotating towards in-plane direction. After the first jump the demagnetization energy increases in the small tilting case to the initial value of an almost entirely perpendicularly magnetized dot.
In the case of two jumps a slow rise happens, while the magnetization is in the intermediate state. This corresponds to the magnetization of the left grain near the grain boundary that rotates more to the perpendicular direction. The change to more in-plane direction in the right grain probably partly compensates for this contribution from the left grain. After the second jump the demagnetization energy is strongly increased. A slow rise with higher field then corresponds to the saturation in perpendicular direction.
The Zeeman energy increases with an applied magnetic field, coming from positive field. It shows steps to lower values for each jump in the hysteresis. After the first jump the total mean z-component of the magnetization points parallel to the magnetic field, because the bigger left grain has switched and thus the Zeeman energy decreases.
The anisotropy energy shows a steep increase before the first jump. This must be caused by the magnetization of left grain being drawn into in-plane direction. In the intermediate state the anisotropy energy change is small, only after the last jump it is at the minimum value.
The total energy in fig 5.25 shows that between 0 T and the first jump the energies are reduced for stronger tilting. In the intermediate state the energy is lower, but higher than in the final state, which is almost the same for all cases.

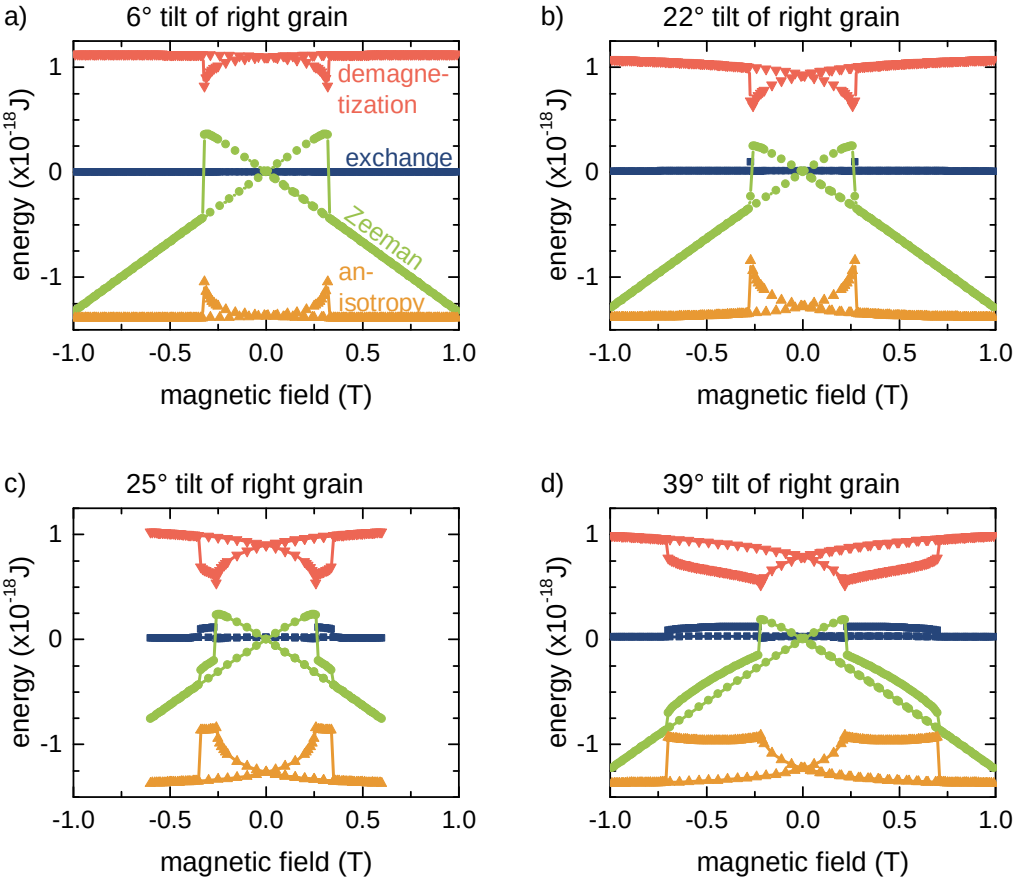

fig 5.24 Energy terms for the simulation of configuration 3. a) For small tilting of 6° of the anisotropy axis the Zeeman contribution changes slightly from what is expected from a homogeneous dot without tilted grains (compare fig 5.9 a)). The exchange energy is constant. However demagnetization and anisotropy energy show a change. The demagnetization energy is slightly lower at 0 T since the magnetization is not entirely pointing perpendicular. Towards higher fields the magnetization rotates further towards the in-plane direction and therefore demagnetization energy is further reduced. After the switching the magnetization is pointing more perpendicular again and so is the demagnetization energy almost back to the old value. This rotation process causes also a change in the anisotropy energy, the energy is increased for higher fields since the magnetization is not pointing in anisotropy axis. b) For 22° the situation is similar as with 6°, but already a second jump in the hysteresis (comp 5.20) and therefore another intermediate state of the magnetization appears. This can be seen also by the small peak of the exchange energy. c) For 25° tilt of the anisotropy axis the intermediate state between the two jumps is more stable. The Zeeman energy is reduced due to the partly switched magnetization, however the exchange energy is increased, the angles between the magnetic moments are larger here. After the second jump all energies are back to the values similar to the low tilting cases. d) Extreme tilting case with very stable intermediate magnetization state with increasing field strength.

In comparison with the simulation with many grains in the previous section 5.2.2, the energy terms of configuration 3 seem very similar. But several differences become apparent at a closer look. The increase in exchange energy in the two grain model is restricted to the intermediate magnetization state between the two jumps in the hysteresis curve. The different sections of the Zeeman term appear here also more linear. Furthermore in the strong tilting case with two jumps there is no discontinuity in the demagnetization and anisotropy energy at the first jump of the hysteresis curve. The increase is steep here but continuous and the changes in both terms are also smaller than in a simulation with many grains.
In principle the two grain simulations show that the grain structure does not need to be very complicated in order to result in two jumps in the hysteresis curves. Only the crystalline axes of one or several grains need to be tilted. It becomes apparent that due to rather small angles between the magnetic moments, the exchange energy increases only a little. The exchange interaction dominates in such a way that 180° wall angles would cost a high amount of energy. Thus a non-vanishing grain exchange is important but, apart from that, the actual strength of the grain exchange does not alter the character of the reversal mode. More relevant is actually the local anisotropy landscape. The anisotropy energy together with Zeeman and demagnetization energy give a complicated interplay to optimize the total energy of the non-uniform magnetization states.

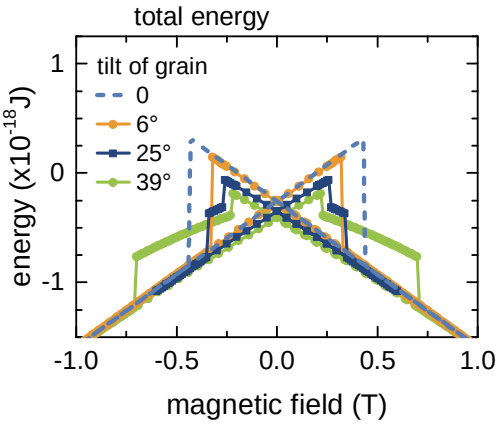

fig 5.25 Total energies for three different tilting angles of configuration 3. Between 0 T and the first jumps the energies are reduced for increased tilting. In the intermediate state the energy is reduced but higher than in the final state, which is almost the same for all cases.

5.3.4 Comparison of measurements and simulations of configuration 3: angular dependence of the switching field

Another aspect was to do simulations of configuration 3 with a tilting angle of the right grain of 31° and the magnetic field applied in various angles. These simulations are now compared with the corresponding measurements of dots with two jumps in the hysteresis curves. An overview is shown in fig 5.26.
On the left, hysteresis curves of the smaller dot, that was discussed in sect. 5.1, are shown. The dot has a diameter of 35 nm and a Co thickness of 1 nm. The measurements, displayed in the overview, were done at 2 K. The angles are measured between the z-axis and the applied field, thus 0° field angle corresponds to a field perpendicular to the plane defined by the Hall cross and 90° corresponds to a field in this plane.
Between 0° and 45° two jumps occur in the hysteresis curves (yellow shaded area). After the easy axis (at 53°) the character changes at a field angle of 60° to hysteresis curves with one jump whose shape could also occur in systems with a perfect Stoner-Wohlfarth behavior (cp fig 2.1 b)).
At a field angle near 105° a second jump at 50 mT appears (violet shading). It seems to form from the rotational part that is visible in the hysteresis curves of the 90° measurement. The sign of the switching field and also the signal change is opposite to the other jump at negative fields. The height ratio of first and second jump (upper half of the hysteresis curves, coming from positive fields, going to negative fields) changes with increasing field angle, until at the hard axis at 150° the magnetization fluctuates between two states at higher fields (only one measurement is shown here). After the hard axis the character of the hysteresis is as in the beginning (yellow shading). Two jumps are visible with the same sign in signal change (or jump direction). The first jump carries roughly $\frac{2}{3}$ of the total signal change and the second jump (together with a small rotational part) the other $\frac{1}{3}$.
The measurements in the second column were done at 80 K. They were done with the bigger dot discussed already in sect. 5.1. The diameter is 60 nm and the Co layer is 1.4 nm thick. The character of the hysteresis curves is very similar to the other dot, there are some minor deviations and the position of the easy and hard axes are slightly shifted. At 45° it seems like maybe an additional jump is present, in fact that is an artifact from the averaging process. The variance of the switching field is rather high here.

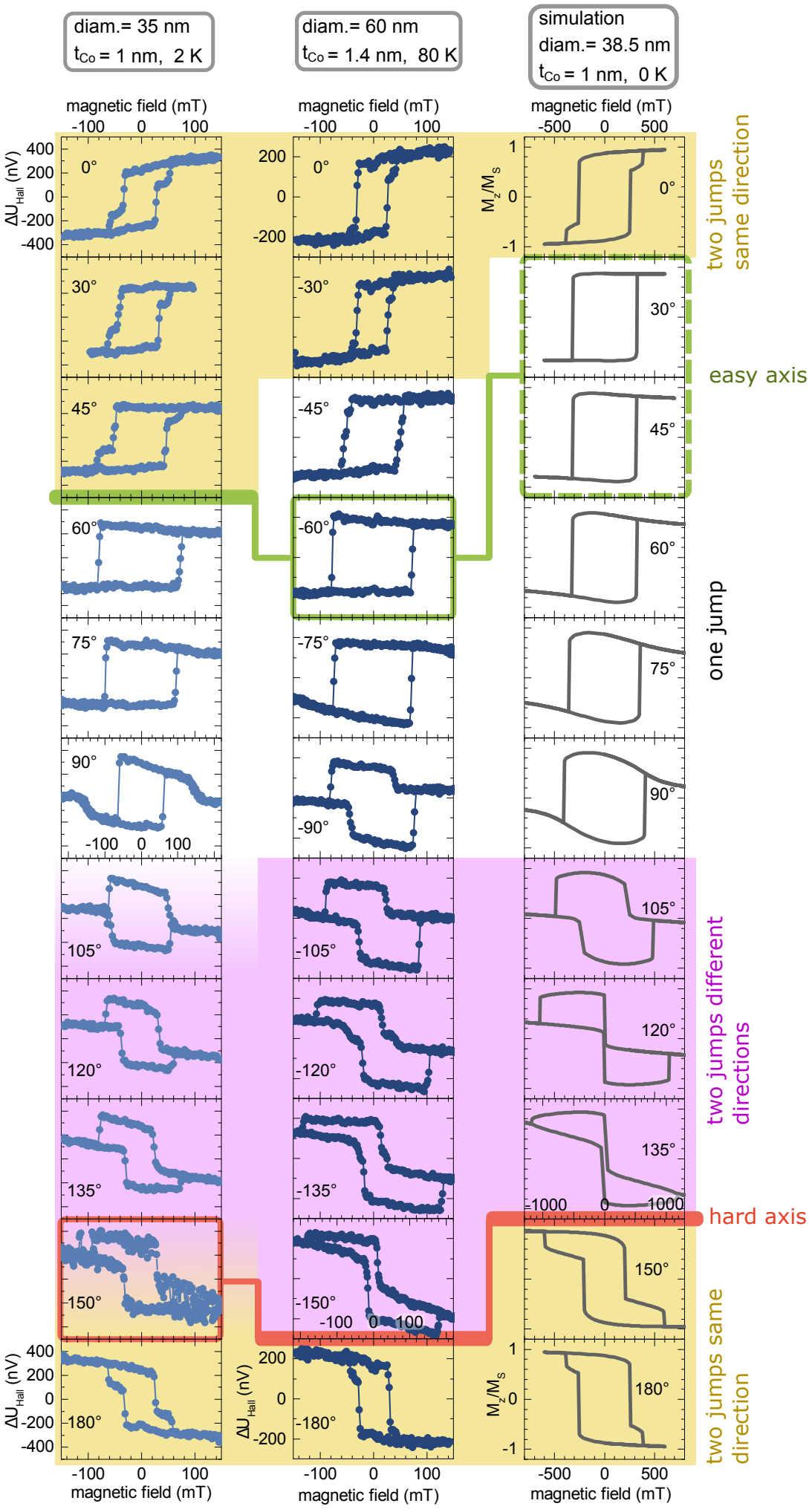
diam.= 35 nm
t_{Co} = 1 nm, 2 K
diam.= 60 nm
t_{Co} = 1.4 nm, 80 K
simulation
diam.= 38.5 nm
t_{Co} = 1 nm, 0 K
magnetic field (mT)
ΔU_{Hall} (nV)
M_z/M_S
two jumps same direction
easy axis
one jump
two jumps different directions
hard axis
two jumps same direction

fig 5.26 (Previous page.) Hysteresis curves with the magnetic field applied in different angles. The two measurements, that were presented in 5.1, are compared with simulations of configuration 3 (tilting of anisotropy 31°).
For better comparison the signals of the first measurement are multiplied by -1, since the voltage leads of the Hall signal were altered compared to the second measurement. For the second measurement the hysteresis curves between -75° and 180° were measured at +105° to 0°. But the magnetic field of the measurement can be multiplied by -1, since a positive field at -75° is the same as a negative field at +105° and vice versa due to symmetry. The -180° measurement is thus the mirrored 0° measurement. All measurements have the same scale except otherwise indicated (90° for the first measurement, -150° for the second measurement and 135° for the simulation).
Over all the characteristics of the hysteresis curves are rather similar. When the magnetic field is perpendicularly applied (0°), all curves show two jumps in the same direction (yellow shaded area). Between 30° and 60° the two jumps converge in the measurements. The simulation exhibits a different behavior here, it shows only one jump at 15° already (hysteresis curve not shown here). At 90° for all three a strong rotation is visible which becomes a second jump with a different sign in signal change and also a different sign in switching field (violet shaded area).
At the hard axis near 150° (150° for the smaller dot, $(28° - 180°) = -153°$ for the larger dot and a few degrees above 135° for the simulation) the hysteresis character changes again to the first type with two jumps having the same sign in signal change and switching field. The angles of the easy axes are all in the same range between for the experiment (53° dot B, -60 dot C), albeit the exact position of the easy axis remains unclear for the simulations (somewhere between 20° and 50°).

The field was applied in the opposite direction (negative angle values) but in principle this should not make any difference for the physics.
In the third column the results of the simulations of configuration 3 (31° tilt) are depicted. The direction of the field is applied with an in-plane angle of 30° as shown in fig 5.28. The character of the simulated hysteresis curves is very similar to the measurements, there are some minor deviations regarding the position of the hard axis and the rotational aspects of the hysteresis between 60° and 105° are more pronounced.
For 90°, 105° and 135° the corresponding magnetization states before and after the jumps are depicted in fig 5.27. In the following only the upper half of the hysteresis curve (fig 5.26, right column) is discussed and the field changed from high positive to negative fields (the other half of hysteresis is point symmetric).

At 90° with high positive fields the magnetization of the left grain is almost in-plane, the magnetization of the right grain still has a certain positive z-component (see fig 5.27). By reducing the field both rotate towards their local easy axis and therefore the m_z is increasing.

The negative applied field rotates them again until at $-0.405\,\mathrm{T}$ they both switch together. Increasing the field further results in a further rotation towards in-plane of (mainly) the right grain. With a field in 105° direction, the rotation, that was visible for 90°, changes into another jump.

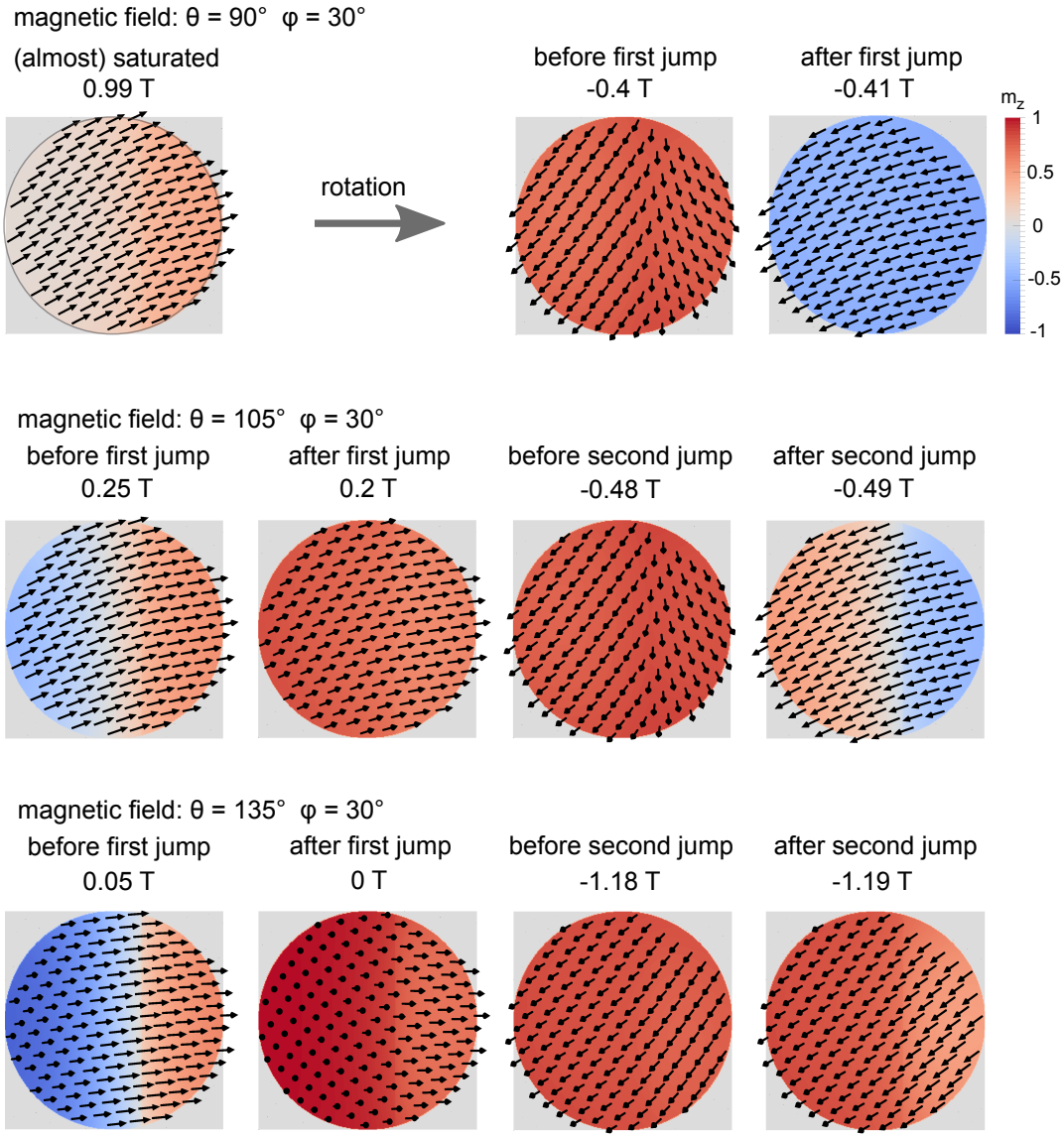

fig 5.27 Some magnetization states of the simulations shown in fig 5.26 (configuration 3, with 31° tilting) for magnetic fields with an angle of $\theta = 90°$ with the z-axis (and 30° with the x-axis), $\theta = 105°$ and $\theta = 135°$. The red blue color code represents the normalized m_z component. The black arrows represent the 3D magnetization vector. More detailed description about the illustrations can be found in fig 5.11.

This jump at 0.225 T is caused by the change in the z-component of the left grain (see fig 5.27). The sign of the switching field and also the signal change is opposite to the other jump at negative field (−0.485 T), which is mainly caused by the right grain. Between 0.2 T and −0.48 T the z-component of the magnetization points in positive direction, some rotation in the in-plane component occurs. Before 0.2 T and at fields higher than −0.48 T the in-plane component is quite homogeneous, but the z-component of the right and left grain point in different directions.
With a field in 135° direction the situation has changed slightly. The first jump at very low fields (0.025 T) has an increased amplitude, since the -z-component of the left grain is higher before the jump. The second jump appears at very high fields (−1.185 T) and is very small. It is still caused by the right grain, but the z-component does not change to negative values, but more to an in-plane direction.
The position of the hard axis was verified also with the help of the astroid calculated from the switching fields of the simulations.

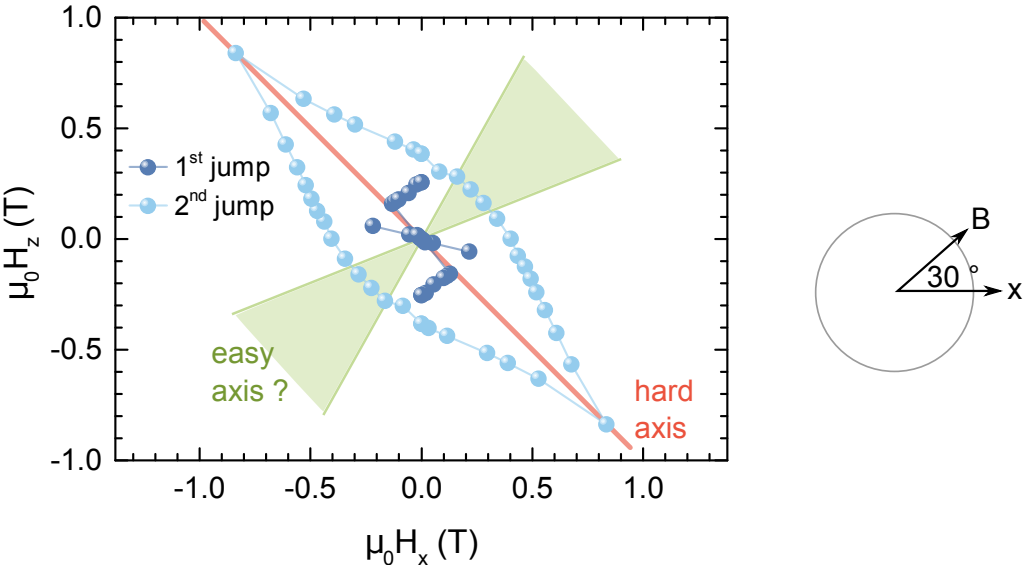

fig 5.28 Switching field astroid from the hysteresis curves of the simulations (configuration 3, 31° tilting) with different field directions shown in fig 5.26. The shape resembles slightly the measured astroid shown in fig 5.5 b). The astroid is also tilted. The shape in the hard axis direction is elongated while in the easy axis direction it is shrunk compared to a SW astroid. The hard axis is near 135°. In the hard axis direction two switching fields occur. An additional feature in the middle of the astroid appears, that is not observed in the measurements. The angle of the plane in which the switching fields were applied is depicted in the sketch on the right hand side.

The astroid is shown fig 5.28. From the magnetization states shown in fig 5.27 (bottom row) it can be concluded, that this is mainly the hard axis of the left small grain. The violet shaded area in fig 5.26 could be interpreted then as the angle range of the magnetic field direction between the hard axis of the left (untilted) and the right grain.
In the astroid it is also visible that the exact position of the easy axis remains unclear since there is no pronounced maximum observed in the astroid. The astroid can be compared to the ones obtained from measurements in fig 5.5. The simulated astroid also has an elongated outer shape in the hard axis direction as the measurement of the dot with larger diameter. The inner data points that correspond to the first jump also form a line perpendicular to the hard axis. However additional features occur in the simulations near zero field, that are not observed in the measurements and might be caused by the simplifications of the two grain model.
It also has to be kept in mind, that the plane for the variation of the field direction of the simulation is not chosen entirely random but not necessarily the same as in the measurements. The angle of 30° was chosen since it is neither parallel nor perpendicular to the grain boundary and also not symmetric like an angle of 45°. But apart from these considerations it was chosen arbitrarily.
It is also very surprising that the two measured examples exhibit such similar hysteresis curves with different field angles. Certainly the switching fields will change when another plane for the variation of the magnetic field is chosen and probably also the details in the shape of the astroids. In principle it would be more favorable to measure in a 3D vector magnet to obtain a 3 dimensional switching field astroid and be able to truly detect the easy axes and the distortions. Then extended simulations with magnetic field in all directions could give more detailed insight into the switching behavior. But still, the simulations presented in this chapter give strong indication that the coherence of the reversal process can be significantly influenced by the change in anisotropy direction of nanodots grain structure. The similarity of configuration 3 with the measurements give rise to the assumption that one bigger or several grains of the dot are tilted in one direction while the rest of the dot has a less tilted anisotropy axis. The domain wall with reduced angle that forms has a Neél character. The tilt of the anisotropy axes might increase with smaller temperatures (as discussed above).
These findings are different from the reversal mechanism of a small nucleation volume followed by immediate propagation of a domain wall which was suggested in literature [27, 72–74, 174]. The dots studied in this thesis are smaller than

those which have been published in literature, thus a strong tilting of one or more grains results in a strongly nonuniform magnetization state. Additionally the grain boundary is the origin of pinning for a domain wall with reduced angle. More detailed and systematic investigation could be interesting to further rule out the exact nature of the incoherent switching process, observed in the experiments. It could be also interesting to simulate other influences, such as a second order anisotropy (K_2).

6 Conclusion and outlook

The switching behavior of the magnetization in individual Co/Pt nanodots and an ensemble of double layer nanodots is studied in this thesis. First a nanodot with almost or quasi coherent switching behavior is presented. The switching field over temperature is fitted with a Sharrock equation and the anisotropy and blocking temperature are estimated from the fit. Also the angular dependence of the switching field is discussed and compared to the Stoner-Wohlfarth model. From measured astroids in three directions it can be concluded that the easy axis of the nanodot is strongly tilted. In the second part of chapter 4 an ensemble of nanodots with a Co double layer is presented. The Co layers are fabricated with different thicknesses and thus anisotropies. They are separated by 3 nm Pt interlayer and in theory this layer should provide for an exchange decoupled switching of the layers. The switching field distributions for the layers in the nanodots are calculated for an ensemble of 10 000 dots with a size distribution deduced from a SEM micrograph of the measured sample. The calculation at 3K shows that the switching fields should be clearly separated. For 300 K a certain overlap can be found, but still the maxima of the distributions can be clearly separated. This theoretical finding does not reflect the experimental results though. Only one maximum can be observed in the derivative of the magnetization to the field, that is equivalent to the swichting field distribution of the ensemble. This gives indication that the switching behavior found is more complicated than expected. Since the experimental switching field distributions are very broad, it is assumed that the local granular structure has a strong influence.
Another interesting effect that was investigated with the ensemble of nanodots is the planar Hall effect (PHE). In individual nanodots at the first glance strange asymmetry of the hysteresis curves was observed when the magnetic field was applied in in-plane direction. This asymmetry increased for lower temperatures. For the ensemble this effect was even more evident. At 3 K the $M(H)$ curves would not resemble a typical hysteresis curve anymore. Via calculation of the point symmetric and axially symmetric signal contribution, the AHE and NHE

signals could be separated from the axially symmetric PHE signal. The origin of PHE is always an anisotropy in the resistance regarding the magnetic field. Here two different contributions could be identified. One contribution is strongly temperature dependent, and proportional to the absolute magnetic field (high field contribution). It is most likely related to the (super)paramagnetic inclusions, since the temperature dependence of this signal corresponds clearly to the temperature dependence of (super)paramagnetic background when the magnetic field is applied perpendicularly to the Hall bar plane. The exact nature of this signal could not be explained however. The other (low field) contribution seems to have a weak temperature dependence only. It can be attributed to the anisotropic magneto resistance caused by the magnetization of the nanodots.
Non-coherent magnetic switching is discussed in chapter 5. First, two examples of measurements with strong non-coherent switching are shown. For both samples with very different properties a second jump appeared in the hysteresis curves for lower temperatures. Even though the temperatures are different where the second jump appeared both hysteresis curves show very similar characteristics when the magnetic field is applied in different angles.
The assumption that this non-coherent switching is caused by the local granular structure is then in the second part of chapter 5 verified by micromagnetic simulations using mumax3. First, a reduced intergranular exchange interaction could be excluded as the origin. Only below 1% of the bulk exchange non-coherence might be expected. From the hysteresis curves of previous film measurements however it is apparent that a certain grain exchange has to be present in the sample system. Therefore the second possibility, a tilting of the grain's easy axis, was explored. First, an example with 9 grains was simulated and promising hysteresis curves were received. Then a two grain model was used to explore three different examples of tilted grain configurations. Especially the third configuration, where only one grain was tilted while the easy axis of the other was still perpendicular, appeared promising. The dependence of switching field with increased tilting could be related to the temperature dependence of the experimental switching fields. A good explanation could be found by a related PhD thesis of S. Freercks. He found that due to interdiffusive interfaces between Co and Pt, with lower temperatures some additional material contributes to the magnetization thus increasing the total saturation magnetization. This increase causes an increase in shape anisotropy and thus a decrease of the total perpendicular anisotropy or an increase of the angle of an already tilted easy axis. The corresponding magnetization state could be related to a Néel wall with reduced wall angle. Also the general variation of the

hysteresis shape with the direction of the applied magnetic field was surprisingly similar to the measured examples. In another configuration where both grains were tilted a Bloch-like wall could be found with a maximum angle of 106° (at a certain magnetic field). Here also a second jump in the hysteresis curve could be observed, but the overall characteristics of the hysteresis appeared different from the experiments. Another configuration showed non-uniform magnetization but quasi-coherent switching behavior. Over all it can be concluded, that the switching can strongly depend on the local granular structure even in systems where coherent switching of the magnetization according to the Stoner-Wohlfarth model is expected from theory. Here it is indeed possible that domain walls with a reduced angle form at the vicinity of grain boundaries. Also an investigation of the magnetization state with varying grain exchange interaction was done, but again only for vanishing exchange a change in the qualitative magnetization configuration could be found. A reduced grain exchange would result only in a reduced Bloch wall width. Evidence is strong that the incoherence is caused by a local variation of the magnetic anisotropy direction, while granular exchange and anisotropy strength play only minor roles.

In future it would be very promising to explore this field in more detail and connect the experiments even more closely to the simulations. Several steps would be crucial for this. First, it would be nice to have quantitative values for the grain exchange interaction. There is also indication that the exchange in the grains of ultrathin films might be reduced as suggested by Wagner [133]. It would be required to know if the grain exchange (between the grains) is homogeneous through the sample or varies locally. Furthermore, it would be interesting to have more detailed structural investigations on the interdiffusive layer by energy dispersive TEM for example and X-ray diffraction experiments with monochromatic X-rays. Magnetic imaging techniques such as high resolution Lorentz microscopy, SEM with polarization analysis (SEMPA) or soft X-ray holographic microscopy (XHM) could give direct insight in the realistic magnetization states. In order to observe the non-coherent switching behavior, it would be necessary to cool down the samples to at least liquid nitrogen temperature and apply fields up to approx. 200 mT. Preparation of the nanodots on very thin membranes (such as done in [177, 178]) would be necessary (except for SEMPA measurements, here it would be necessary to remove some of the Pt top layer). With, for example, dark field TEM, this could give more insight into the local grain structure and one could relate this directly to measurements of non-coherent switching of the magnetization. It would

be preferable to do in situ Hall measurements on that dot and compare both. This increases the difficulties in the E-beam fabrication procedure however, since as in the samples presented here, a second fabrication step is required.
For a better understanding of the unexpected coupling of the double layer dots one could do experiments with a little increased interlayer thickness. It would be also beneficial to do micromagnetic simulations of two dots separated by an interlayer and to investigate the exchange interaction and stray field interaction of the system.
Furthermore, more detailed experiments are necessary to understand what effect is the origin of the high field temperature dependent linear contribution to the planar Hall effect. Here it would be also very interesting to do more investigations on the longitudinal resistivity to study AMR on ensembles and also with a modified sample layout where the nanodots are present only in the crossing area to compare if the relation $(\rho_{\parallel} - \rho_{\perp})/2 = \Delta\rho_{\mathrm{PHE}}$ is fulfilled. Since the contacted dots on the Hall bars are very sensitive, it would be also preferable to do 3D AHE measurements in a specialized cryostat with a 3D magnet in order to avoid changes in the magnetic properties due to electrostatic discharge in the sample while changing the mounting.
Another exciting topic is the investigation of double layer nanodots with antiferromagnetic coupling, since they have an extremely reduced stray field. Antiferromagnetic coupling could be provided by an Ir interlayer for example. These systems are also strongly influenced on growth conditions and layer composition however, as was found out recently in the thesis of Wagner [133].
Additionally, currently very interesting measurements are done by the collaborating Group of Prof. Blick that are investigating the interaction of the nanodots with graphene via electron spin resonance. The stray field of the nanodots influences the measured transport of the graphene on top of the nanodots [191].

Appendix

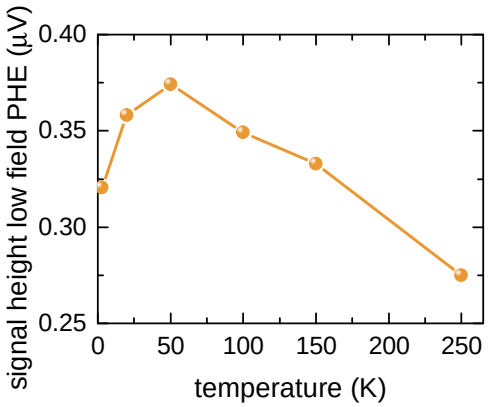

fig .1 Signalheigth of the low field PHE signal in fig 4.24 over temperature (lines are streight connections of the data points and guide to the eye only).

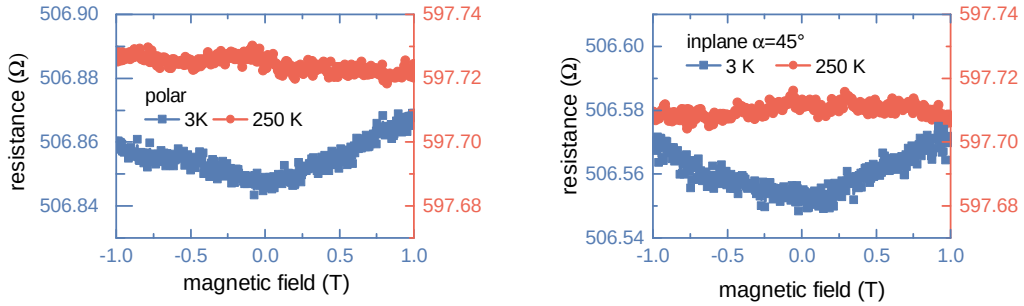

fig .2 double layer nanodots: a) polar b) in-plane. In a measurement at 200K however still a small change in the resistance is observed.

Bibliography

[1] A. Andrae and T. Edler, «On Global Electricity Usage of Communication Technology: Trends to 2030», Challenges pp. 117–157 (2015) (cit. on p. 9).

[2] N. Jones, «How to stop data centres from gobbling up the world's electricity», Nature, News feature **Vol. 561**, 163 (2018) (cit. on p. 9).

[3] J. Malmodin and D. Lundén, «The Energy and Carbon Footprint of the Global ICT and E&M Sectors 2010–2015», Sustainability p. 3027 (2018) (cit. on p. 9).

[4] J. Dulac, T. Abergel, and C. Delmastro, *Data centres and data transmission networks, tracking report*, Tech. rep., International Energy Agency IEA (2019) (cit. on p. 9).

[5] L. Stobbe, M. Proske, H. Zedel, R. Hintemann, J. Clausen, and S. Beucker, *Entwicklung des IKT-bedingten Strombedarfs in Deutschland. Abschlussbericht, Studie im Auftrag des Bundesministeriums für Wirtschaft und Energie*, Tech. rep., Fraunhofer-Institut für Zuverlässigkeit und Mikrointegration, IZM, Berlin und Borderstep Institut für Innovation und Nachhaltigkeit gemeinnützige GmbH (cit. on p. 9).

[6] A. Moser, K. Takano, D. T. Margulies, M. Albrecht, Y. Sonobe, Y. Ikeda, S. Sun, and E. E. Fullerton, «Magnetic recording: advancing into the future», J. Phys. D: Appl. Phys. **35**, R157 (2002) (cit. on p. 9).

[7] Western Digital, *Data sheet Ultrastar DC HC620* (2019) (cit. on p. 10).

[8] *Data Sheet, Exos X16* (2019) (cit. on p. 10).

[9] M. Kief and R. Victora, «Materials for heat-assisted magnetic recording», MRS Bulletin **43**, 87–92 (2018) (cit. on p. 10).

[10] D. Weller and A. Moser, «Thermal effect limits in ultrahigh-density magnetic recording», IEEE Trans. Magn. **35**, 4423 (1999) (cit. on p. 10).

[11] D. E. Speliotis, «Magnetic recording beyond the first 100 Years», J. Magn. Magn. Mater. **193**, 29 (1999) (cit. on p. 10).

[12] C. Chappert, A. Fert, and F. N. Van Dau, «The emergence of spin electronics in data storage», Nature materials **6**, 813—823 (2007) (cit. on p. 10).

[13] C. Ross, «Patterned Magnetic Recording Media», Annual Review of Materials Research **31**, 203 (2001) (cit. on p. 10).

[14] J. Zhu, X. Zhu, and Y. Tang, «Microwave Assisted Magnetic Recording», IEEE Transactions on Magnetics **44**, 125 (2008) (cit. on p. 10).

[15] S. Okamoto, N. Kikuchi, M. Furuta, O. Kitakami, and T. Shimatsu, «Microwave assisted magnetic recording technologies and related physics», Journal of Physics D: Applied Physics **48**, 353001 (2015) (cit. on p. 10).

[16] D. Weller, G. Parker, O. Mosendz, E. Champion, B. Stipe, X. Wang, T. Klemmer, G. Ju, and A. Ajan, «A HAMR Media Technology Roadmap to an Areal Density of 4 Tb/in^2», IEEE Transactions on Magnetics **50**, 1 (2014) (cit. on p. 10).

[17] K. Hono, Y. Takahashi, G. Ju, J.-U. Thiele, A. Ajan, X. Yang, R. Ruiz, and L. Wan, «Heat-assisted magnetic recording media materials», MRS Bulletin **43**, 93–99 (2018) (cit. on p. 10).

[18] R. L. White, R. M. H. Newt, and R. F. W. Pease, «Patterned media: a viable route to 50 Gbit/in/sup 2/ and up for magnetic recording?», IEEE Transactions on Magnetics **33**, 990 (1997) (cit. on p. 10).

[19] C. Ross, «Patterned Magnetic Recording Media», Annual Review of Materials Research **31**, 203 (2001) (cit. on p. 10).

[20] B. Terris and T. Thomson, «Nanofabricated and self-assembled magnetic structures as data storage media», J. Phys. D: Appl. Phys. **38**, R199 (2005) (cit. on p. 10).

[21] A. Kikitsu, Y. Kamata, M. Sakurai, and K. Naito, «Recent Progress of Patterned Media», IEEE Transactions on Magnetics **43**, 3685 (2007) (cit. on p. 10).

[22] X. Yang, Y. Xu, K. Lee, S. Xiao, D. Kuo, and D. Weller, «Advanced Lithography for Bit Patterned Media», IEEE Trans. Magn. **45**, 833 (2009) (cit. on p. 10).

[23] X. Yang, S. Xiao, W. Hu, J. Hwu, R. van de Veerdonk, K. Wago, K. Lee, and D. Kuo, «Integration of nanoimprint lithography with block copolymer directed self-assembly for fabrication of a sub-20 nm template for bit-patterned media», Nanotechnology **25**, 395301 (2014) (cit. on p. 10).

[24] T. R. Albrecht, H. Arora, V. Ayanoor-Vitikkate, J. Beaujour, D. Bedau, D. Berman, A. L. Bogdanov, Y. Chapuis, J. Cushen, E. E. Dobisz, G. Doerk, H. Gao, M. Grobis, B. Gurney, W. Hanson, O. Hellwig, T. Hirano, P. Jubert, D. Kercher, J. Lille, Z. Liu, C. M. Mate, Y. Obukhov, K. C. Patel, K. Rubin, R. Ruiz, M. Schabes, L. Wan, D. Weller, T. Wu, and E. Yang, «Bit-Patterned Magnetic Recording: Theory, Media Fabrication, and Recording Performance», IEEE Transactions on Magnetics **51**, 1 (2015) (cit. on p. 10).

[25] Z. Meng, G. Li, H.-F. Wong, S.-M. Ng, S.-C. Yiu, C.-L. Ho, C.-W. Leung, I. Manners, and W.-Y. Wong, «Patterning of L10 FePt nanoparticles with ultra-high coercivity for bit-patterned media», Nanoscale **9**, 731—738 (2017) (cit. on p. 10).

[26] «Advanced Storage Technology Consortium, ASTC Technology Roadmap», http : //idema.org/?page_id = 5868 (2016) (cit. on p. 10).

[27] T. Thomson, G. Hu, and B. D. Terris, «Intrinsic Distribution of Magnetic Anisotropy in Thin Films Probed by Patterned Nanostructures», Phys. Rev. Lett. **96**, 257204 (2006) (cit. on pp. 10, 11, 15, 58, 87, 90, 126).

[28] O. Hellwig, A. Berger, T. Thomson, E. Dobisz, Z. Z. Bandic, H. Yang, D. S. Kercher, and E. E. Fullerton, «Separating dipolar broadening from the intrinsic switching field distribution in perpendicular patterned media», Appl. Phys. Lett. **90**, 162516 (2007) (cit. on p. 10).

[29] B. Pfau, C. M. Günther, E. Guehrs, T. Hauet, H. Yang, L. Vinh, X. Xu, D. Yaney, R. Rick, S. Eisebitt, and O. Hellwig, «Origin of magnetic switching field distribution in bit patterned media based on pre-patterned substrates», Appl. Phys. Lett. **99**, 062502 (2011) (cit. on p. 10).

[30] T. Hauet, L. Piraux, S. K. Srivastava, V. A. Antohe, D. Lacour, M. Hehn, F. Montaigne, J. Schwenk, M. A. Marioni, H. J. Hug, O. Hovorka, A. Berger, S. Mangin, and F. Abreu Araujo, «Reversal mechanism, switching field distribution, and dipolar frustrations in Co/Pt bit pattern media based on auto-assembled anodic alumina hexagonal nanobump arrays», Phys. Rev. B **89**, 174421 (2014) (cit. on pp. 10, 11).

[31] B. Gleich and J. Weizenecker, «Tomographic imaging using the nonlinearresponse of magnetic particles», Nature **435**, 1214–1217 (2005) (cit. on p. 10).

[32] C. Sun, J. S. Lee, and M. Zhang, «Magnetic nanoparticles in MR imaging and drug delivery», Advanced Drug Delivery Reviews **60**, 1252 (2008), inorganic Nanoparticles in Drug Delivery (cit. on p. 10).

[33] M. Graeser, F. Thieben, P. Szwargulski, F. Werner, N. Gdaniec, M. Boberg, F. Griese, M. Möddel, P. Ludewig, D. van de Ven, O. M. Weber, O. Woywode, B. Gleich, and T. Knopp, «Human-sized magnetic particle imaging for brain applications», Nature Communications p. 1936 (2019) (cit. on p. 10).

[34] E. C. Stoner and E. P. Wohlfarth, «A Mechanism of Magnetic Hysteresis in Heterogeneous Alloys», Philosophical Transactions of the Royal Society of London. Series A, Mathematical and Physical Sciences **240**, 599 (1948) (cit. on pp. 11, 15, 16, 19).

[35] C. Ross, T. Savas, H. Smith, M. Hwang, and R. Chantrell, «Modelling of hysteresis loops of arrays of 100 nm period nanomagnets», IEEE Trans. Magn. **35**, 3781 (1999) (cit. on p. 11).

[36] D. Makarov, E. Bermudez-Urena, O. G. Schmidt, F. Liscio, M. Maret, C. Brombacher, S. Schulze, M. Hietschold, and M. Albrecht, «Nanopatterned CoPt alloys with perpendicular magnetic anisotropy», Appl. Phys. Lett. **93**, 153112 (2008) (cit. on p. 11).

[37] J. Jamet, S. Lemerle, P. Meyer, J. Ferre, B. Bartenlian, N. Bardou, C. Chappert, P. Veillet, F. Rousseaux, D. Decanini, and H. Launois, «Dynamics of the magnetization reversal in Au/Co/Au micrometer-size dot arrays», Phys. Rev. B **57**, 14320 (1998) (cit. on p. 11).

[38] D. Allwood, G. Xiong, M. Cooke, and R. Cowburn, «Magneto-optical Kerr effect analysis of magnetic nanostructures», J. Phys. D: Appl. Phys. **36**, 2175 (2003) (cit. on p. 11).

[39] J. M. Shaw, H. T. Nembach, T. J. Silva, S. E. Russek, R. Geiss, C. Jones, N. Clark, T. Leo, and D. J. Smith, «Effect of microstructure on magnetic properties and anisotropy distributions in Co/Pd thin films and nanostructures», Phys. Rev. B **80**, 184419 (2009) (cit. on p. 11).

[40] A. Neumann, A. Frauen, J. Vollmers, A. Meyer, and H. P. Oepen, «Structure-induced spin reorientation in magnetic nanostructures», Phys. Rev. B **94**, 094430 (2016) (cit. on p. 11).

[41] M. Pardavi-Horvath, «Switching properties of a regular two-dimensional array of small uniaxial particles», IEEE Trans. Magn. **32**, 4458 (1996) (cit. on p. 11).

[42] M. Haast, I. Heskamp, L. Abelmann, J. Lodder, and T. Popma, «Magnetic characterization of large area arrays of single and multi domain CoNi/Pt multilayer dots», J. Magn. Magn. Mater. **193**, 511 (1999) (cit. on p. 11).

[43] M. Bode, «Spin-polarized scanning tunnelling microscopy», Rep. Prog. Phys. **66**, 523 (2003) (cit. on p. 11).

[44] S. Krause, L. Berbil-Bautista, G. Herzog, M. Bode, and R. Wiesendanger, «Current-Induced Magnetization Switching with a Spin-Polarized Scanning Tunneling Microscope», Science **317**, 1537 (2007) (cit. on p. 11).

[45] K. Koike, «Spin-polarized scanning electron microscopy», Microscopy **62**, 177 (2013) (cit. on p. 11).

[46] R. Frömter, R.mter, F. Kloodt, S. Rößler, A. Frauen, P. Staeck, D. R. Cavicchia, L. Bocklage, V. Röbisch, E. Quandt, and H. P. Oepen, «Time-resolved scanning electron microscopy with polarization analysis», Applied Physics Letters **108**, 142401 (2016) (cit. on p. 11).

[47] F. Kloodt-Twesten, S. Kuhrau, P. Staeck, D. R. Cavicchia, F. Lofink, H. P. Oepen, and R. Frömter, «Coupling between vortices and antivortices in a cross-tie wall studied by time-resolved SEMPA», Phys. Rev. B **97**, 024426 (2018) (cit. on p. 11).

[48] K. J. Kirk, J. N. Chapman, and C. D. W. Wilkinson, «Lorentz microscopy of small magnetic structures (invited)», J. Appl. Phys. **85**, 5237 (1999) (cit. on p. 11).

[49] K. J. Kirk, S. McVitie, A. R. Long, and E. Skuras, «Magnetization of Co elements sensed by semiconductor transport magnetometry and transmission electron microscopy», J. Appl. Phys. **93**, 7906 (2003) (cit. on p. 11).

[50] S. Eisebitt, J. Lüning, W. F. Schlotter, M. Lörgen, O. Hellwig, W. Eberhardt, and J. Stöhr, «Lensless imaging of magnetic nanostructures by X-ray spectroholography», Nature **432**, 885 (2004) (cit. on p. 11).

[51] D. Stickler, R. Frömter, H. Stillrich, C. Menk, C. Tieg, S. Streit-Nierobisch, M. Sprung, C. Gutt, L.-M. Stadler, O. Leupold, G. Grübel, and H. P. Oepen, «Soft x-ray holographic microscopy», Applied Physics Letters **96**, 042501 (2010) (cit. on p. 11).

[52] C. Thönnißen, *Magnetische Eigenschaften von einzelnen Co/Pt- und Co-Nanostrukturen*, Ph.D. thesis (2018) (cit. on pp. 11, 32, 43, 44, 60, 95).

[53] W. Wernsdorfer, K. Hasselbach, A. Benoit, W. Wernsdorfer, B. Barbara, D. Mailly, J. Tuaillon, J. P. Perez, V. Dupuis, J. P. Dupin, G. Guiraud, and A. Perex, «High sensitivity magnetization measurements of nanoscale cobalt clusters», J. Appl. Phys. **78**, 7192 (1995) (cit. on p. 11).

[54] K. Hasselbach, W. Wernsdorfer, D. Mailly, B. Barbara, and A. Benoit, «Magnetization reversal in single ferromagnetic Ni and Co particles», Czech. J. Phys. **46**, 2137 (1996) (cit. on pp. 11, 44).

[55] E. Bonet, W. Wernsdorfer, B. Barbara, A. Benoit, D. Mailly, and A. Thiaville, «Three-dimensional magnetization reversal measurements in nanoparticles», Phys. Rev. Lett. **83**, 4188 (1999) (cit. on pp. 11, 45).

[56] D. Schuh, J. Biberger, A. Bauer, W. Breuer, and D. Weiss, «Hall-magnetometry on ferromagnetic dots and dot arrays», IEEE Transactions on Magnetics **37**, 2091 (2001) (cit. on p. 11).

[57] N. Kikuchi, S. Okamoto, O. Kitakami, Y. Shimada, and K. Fukamichi, «Sensitive detection of irreversible switching in a single FePt nanosized dot», Appl. Phys. Lett. **82**, 4313 (2003) (cit. on p. 11).

[58] N. Kikuchi, R. Murillo, and J. Lodder, «Anomalous Hall-effect measurement study on Co/Pt nanosized dot», J. Appl. Phys. **97**, 10J713 (2005) (cit. on p. 11).

[59] S. Okamoto, T. Kato, N. Kikuchi, O. Kitakami, N. Tezuka, and S. Sugimoto, «Energy barrier and reversal mechanism in Co/Pt multilayer nanodot», J. Appl. Phys. **103**, 07C501 (2008) (cit. on p. 11).

[60] N. Kikuchi, T. Kato, S. Okamoto, O. Kitakami, N. Tezuka, and S. Sugimoto, «Magnetization reversal process and bistability of Co/Pt multilayer dot», J. Appl. Phys. **103**, 07C510 (2008) (cit. on p. 11).

[61] A. Neumann, C. Thönnißen, A. Frauen, S. Heße, A. Meyer, and H. P. Oepen, «Probing the Magnetic Behavior of Single Nanodots», Nano Lett. **13**, 2199 (2013) (cit. on pp. 11, 33, 95).

[62] A. Vansteenkiste, J. Leliaert, M. Dvornik, M. Helsen, F. Garcia-Sanchez, and B. V. Waeyenberge, «The design and verification of MuMax3», AIP Advances **4**, 107133 (2014) (cit. on pp. 11, 26, 27, 89).

[63] G. Winkler, A. Kobs, A. Chuvilin, D. Lott, A. Schreyer, and H. P. Oepen, «On the variation of magnetic anisotropy in Co/Pt(111) on silicon oxide», Journal of Applied Physics **117**, 105306 (2015) (cit. on pp. 11, 29, 30, 89, 95, 96).

[64] G. Winkler, *Korrelation zwischen strukturellen und magnetogalvanischen Eigenschaften von Pt/Co/Pt- und Pd/Co/Pd-Schichtsystemen*, Ph.D. thesis (2015) (cit. on pp. 11, 29, 30, 96).

[65] A. Kobs, *Magnetogalvanic effects in ferromagnets of reduced dimensions*, Ph.D. thesis, Universität Hamburg (2013) (cit. on pp. 11, 29, 30, 34, 38, 40, 51, 55, 70, 72, 95, 96).

[66] A. Hubert and R. Schäfer, *Magnetic Domains* (Springer-Verlag Berlin Heidelberg, 1998) (cit. on pp. 13, 14, 16, 104, 107, 116).

[67] R. C. O'Handley, *Modern Magnetic Materials: Principles and Applications* (John Wiley & Sons Inc., 2000) (cit. on p. 13).

[68] J. Stöhr and H. C. Siegmann, *Magnetism: From Fundamentals to Nanoscale Dynamics*, Solid-State Sciences (Springer-Verlag Berlin Heidelberg, 2006) (cit. on pp. 13, 16).

[69] Y. Millev, E. Vedmedenko, and H. Oepen, «Dipolar magnetic anisotropy energy of laterally confined ultrathin ferromagnets: multiplicative separation of discrete and continuum contributions», J. Phys. D: Appl. Phys. **36**, 2945 (2003) (cit. on pp. 15, 56, 89).

[70] A. Aharoni, *Introduction to the Theory of Ferromagnetism* (Oxford University Press, 2000), second edition edn. (cit. on p. 15).

[71] E. Kondorsky, «On Hysteresis in Ferromagnetics», J. Phys. (Moscow) **II**, 161 (1940) (cit. on p. 15).

[72] Y. Uesaka, Y. Nakatani, and N. Hayashi, «Switching of Single Hexagonal Particles with Nonuniform Magnetic Properties», Jpn. J. Appl. Phys. **34**, 6056 (1995) (cit. on pp. 15, 87, 126).

[73] R. Dittrich, G. Hu, T. Schrefl, T. Thomson, D. Suess, B. D. Terris, and J. Fidler, «Angular dependence of the switching field in patterned magnetic elements», J. Appl. Phys. **97**, 10J705 (2005) (cit. on pp. 15, 87, 126).

[74] G. Hu, T. Thomson, C. Rettner, and B. Terris, «Rotation and wall propagation in multidomain Co/Pd islands», IEEE Trans. Magn. **41**, 3589 (2005) (cit. on pp. 15, 87, 126).

[75] M. Stearns, *Landolt-Börnstein - Group III: Condensed Matter, Numerical Data and Functional Relationships in Science and Technology, Vol 19a: 3d, 4d and 5d Elements, Alloys and Compounds*, chap. 1.1.2 Fe, Co, Ni, pp. 24–141 (Springer-Verlag Berlin, 1986) (cit. on pp. 16, 89).

[76] D. Stickler, R. Frömter, H. Stillrich, C. Menk, H. P. Oepen, C. Gutt, S. Streit-Nierobisch, L.-M. Stadler, G. Grübel, C. Tieg, and F. Yakhou-Harris, «Domain size in systems with canted magnetization», Physical Review B **84** (2011) (cit. on pp. 16, 89).

[77] R. Skomski, H.-P. Oepen, and J. Kirschner, «Micromagnetics of ultrathin films with perpendicular magnetic anisotropy», Phys. Rev. B **58**, 3223 (1998) (cit. on p. 16).

[78] J. A. Arregi, O. Idigoras, P. Vavassori, and A. Berger, «Field orientation dependent decorrelation of magnetization reversal in uniaxial Co-films», Applied Physics Letters **100**, 262403 (2012) (cit. on p. 18).

[79] C. Tannous and J. Gieraltowski, «The Stoner-Wolfarth model of ferromagnetism», Eur. J. Phys. **29**, 475 (2008) (cit. on p. 20).

[80] L. Néel, «Théorie du traînage magnétique des ferromagnétiques en grains fins avec applications aux terres cuites», Ann. Géophys **5**, 99 (1949) (cit. on p. 20).

[81] J. W. F. Brown, «Relaxational Behavior of Fine Magnetic Particles», J. Appl. Phys. **30**, S130 (1959) (cit. on p. 20).

[82] W. F. Brown, «Thermal Fluctuations of a Single-Domain Particle», Phys. Rev. **130**, 1677 (1963) (cit. on p. 20).

[83] L. Néel, *Selected Works of Louis Néel*, chap. Superparamagnetism of very small antiferromagnetic particles, pp. 107–113 (Gordon and Breach Science Publishers, 1988) (cit. on p. 20).

[84] W. T. Coffey and Y. P. Kalmykov, «Thermal fluctuations of magnetic nanoparticles: Fifty years after Brown», J. Appl. Phys. **112**, 121301 (2012) (cit. on pp. 20, 23).

[85] C. P. Bean and J. D. Livingston, «Superparamagnetism», J. Appl. Phys. **30**, 120S (1959) (cit. on pp. 20, 62).

[86] M. Sharrock and J. McKinney, «Kinetic effects in coercivity measurements», IEEE Trans. Magn. **17**, 3020 (1981) (cit. on p. 21).

[87] M. Sharrock, «Time-dependent magnetic phenomena and particle-size effects in recording media», IEEE Trans. Magn. **26**, 193 (1990) (cit. on p. 21).

[88] E. Kneller and E. P. Wohlfarth, «Effect of Thermal Fluctuations on the Anhysteretic Process in Ferromagnetic Fine-Particle Assemblies», J. Appl. Phys. **37**, 4816 (1966) (cit. on p. 21).

[89] R. Skomski, *Simple Models of Magnetism* (Oxford University Press Inc., New York, 2008) (cit. on p. 21).

[90] A. Neumann, *Magnetisierungsverhalten einzelner ferromagnetischer Nanostrukturen*, Ph.D. thesis (2014) (cit. on pp. 21, 23, 31, 32, 43, 44, 51, 52, 56).

[91] A. Garg, «Escape-field distribution for escape from a metastable potential well subject to a steadily increasing bias field», Phys. Rev. B **51**, 15592 (1995) (cit. on pp. 21, 23).

[92] L. Breth, D. Suess, C. Vogler, B. Bergmair, M. Fuger, R. Heer, and H. Brueckl, «Thermal switching field distribution of a single domain particle for field-dependent attempt frequency», J. Appl. Phys. **112**, 023903 (2012) (cit. on pp. 22, 23, 56).

[93] C. M. Hurd, *The Hall Effect in Metals and Alloys* (Plenum Press, New York, 1972) (cit. on pp. 23, 24, 25, 38).

[94] R. Karplus and J. M. Luttinger, «Hall Effect in Ferromagnetics», Phys. Rev. **95**, 1154 (1954) (cit. on p. 24).

[95] J. Kötzler and W. Gil, «Anomalous Hall resistivity of cobalt films: Evidence for the intrinsic spin-orbit effect», Phys. Rev. B **72**, 060412 (2005) (cit. on pp. 24, 40).

[96] S. P. McAlister and C. M. Hurd, «Hall effect in 3d-transition metals and alloys (invited)», Journal of Applied Physics **50**, 7526 (1979) (cit. on p. 24).

[97] A.Gerber, A. Milner, M. Karpovsky, B. Lemke, H.-U. Habermeier, J. Tuaillon-Combes, M. Négrier, O. Boisron, P. Mélinon, and A. Perez, «Extraordinary Hall effect in magnetic films», Journal of Magnetism and Magnetic Materials **242-245**, 90 (2002), proceedings of the Joint European Magnetic Symposia (JEMS'01) (cit. on p. 24).

[98] N. Nagaosa, J. Sinova, S. Onoda, A. H. MacDonald, and N. P. Ong, «Anomalous Hall effect», Rev. Mod. Phys. **82**, 1539 (2010) (cit. on p. 24).

[99] C. Goldberg and R. E. Davis, «New Galvanomagnetic Effect», Physical Review **94**, 1121 (1954) (cit. on p. 24).

[100] K. M. Koch, «Notizen: Zum Problem der galvanomagnetischen Effekte in Ferromagneticis», Zeitschrift für Naturforschung A **10** (1955) (cit. on p. 25).

[101] C. Hurd, «Galvanomagnetic effects in anisotropic metals», Advances in Physics **23**, 315 (1974) (cit. on pp. 25, 63).

[102] J. Jan, «Galvanomagnetic and Thermomagnetic Effects in Metals», Solid State Physics **Vol. 5** (1957) (cit. on p. 25).

[103] M. Donahue and D. Porter, *OOMMF User's Guide, Version 1.0*, Interagency Report NISTIR 6376, National Institute of Standards and Technology, Gaithersburg, MD (1999) (cit. on p. 27).

[104] J. Leliaert, M. Dvornik, J. Mulkers, J. D. Clercq, M. V. Milošević, and B. V. Waeyenberge, «Fast micromagnetic simulations on GPU—recent advances made with mumax^3», Journal of Physics D: Applied Physics **51**, 123002 (2018) (cit. on p. 27).

[105] J. Fidler and T. Schrefl, «Micromagnetic modelling - the current state of the art», Journal of Physics D: Applied Physics **33**, R135 (2000) (cit. on p. 27).

[106] M. Kruzík and A. Prohl, «Recent Developments in the Modeling, Analysis, and Numerics of Ferromagnetism», SIAM Review **48**, 439 (2006) (cit. on p. 27).

[107] P. F. Carcia, «Perpendicular magnetic anisotropy in Pd/Co and Pt/Co thin-film layered structures», Journal of Applied Physics **63**, 5066 (1988) (cit. on p. 29).

[108] M. Wellhöfer, *Herstellung ultradünner magnetischer Co/Pt-Filme mit Hilfe der ECR-Ionenätztechnik und Charakterisierung*, Master's thesis, Universität Hamburg (2003) (cit. on p. 29).

[109] M. Wellhöfer, M. Weissenborn, R. Anton, S. Pütter, and H. P. Oepen, «Morphology and magnetic properties of ECR ion beam sputtered Co/Pt films», J. Magn. Magn. Mater. **292**, 345–358 (2005) (cit. on p. 29).

[110] H. Stillrich, C. Menk, R. Fromter, and H. P. Oepen, «Magnetic anisotropy and the cone state in Co/Pt multilayer films», J. Appl. Phys. **105**, 07C308 (2009) (cit. on p. 29).

[111] H. Stillrich, C. Menk, R. Fromter, and H. P. Oepen, «Magnetic anisotropy and spin reorientation in Co/Pt multilayers: Influence of preparation», J. Magn. Magn. Mater. **322**, 1353–1356 (2010) (cit. on p. 29).

[112] A. Kobs, S. Heße, W. Kreuzpaintner, G. Winkler, D. Lott, P. Weinberger, A. Schreyer, and H. P. Oepen, «Anisotropic Interface Magnetoresistance inPt/Co/PtSandwiches», Physical Review Letters **106** (2011) (cit. on p. 29).

[113] C. Thönnißen, *Untersuchung der Schichtdickenabhängigkeit und Zuordnung der Hall-Signale einzelner Co/Pt-Nanodots*, Master's thesis, Universität Hamburg (2012) (cit. on pp. 31, 51, 52).

[114] H. R. Kaufman and R. S. Robinson, «Ion Source Design for Industrial Applications», AIAA Journal **20**, 745 (1982) (cit. on p. 32).

[115] P. Staeck, *Untersuchungen zur Wechselwirkung von magnetischen Nanostrukturen mittels Magnetotransport*, Ph.D. thesis (2017) (cit. on pp. 32, 39, 40, 44, 45, 56, 95, 96, 97).

[116] «Private communication with Christoph Karl from Oxford instruments», (cit. on p. 33).

[117] A. Pippard, *Magnetoresistance in Metals* (Cambridge University Press, 1989) (cit. on p. 33).

[118] R. Henriquez, L. Moraga, G. Kremer, M. Flores, A. Espinosa, and R. C. Munoz, «Size effects in thin gold films: Discrimination between electron-surface and electron-grain boundary scattering by measuring the Hall effect at 4 K», Applied Physics Letters **102**, 051608 (2013) (cit. on p. 34).

[119] B. S. Kwak, P. N. First, A. Erbil, B. J. Wilkens, J. D. Budai, M. F. Chisholm, and L. A. Boatner, «Study of epitaxial platinum thin films grown by metalorganic chemical vapor deposition», Journal of Applied Physics **72**, 3735 (1992) (cit. on p. 34).

[120] U. Rüdiger, J. Yu, L. Thomas, S. S. P. Parkin, and A. D. Kent, «Magnetoresistance, micromagnetism, and domain-wall scattering in epitaxial hcp Co films», Phys. Rev. B **59**, 11914 (1999) (cit. on p. 34).

[121] R. Skomski, «Nanomagnetics», Journal of Physics: Condensed Matter **15**, R841 (2003) (cit. on p. 37).

[122] P. Krone, D. Makarov, M. Albrecht, T. Schrefl, and D. Suess, «Magnetization reversal processes of single nanomagnets and their energy barrier», J. Magn. Magn. Mater. **322**, 3771 (2010) (cit. on p. 37).

[123] S. Pal, S. Saha, D. Polley, and A. Barman, «Magnetization reversal dynamics in Co nanowires with competing magnetic anisotropies», Solid State Communications **151**, 1994 (2011) (cit. on p. 37).

[124] A. Fernández-Pacheco, J. M. D. Teresa, R. Córdoba, and M. R. Ibarra, «Magnetotransport properties of high-quality cobalt nanowires grown by focused-electron-beam-induced deposition», Journal of Physics D: Applied Physics **42**, 055005 (2009) (cit. on p. 40).

[125] M. D. Kuz'min, «Shape of Temperature Dependence of Spontaneous Magnetization of Ferromagnets: Quantitative Analysis», Physical Review Letters **94** (2005) (cit. on p. 41).

[126] S. Blundell, *Magnetism in Condensed Matter* (Oxford University Press Inc., New York, 2006) (cit. on p. 41).

[127] C. Kittel, *Introduction to solid state physics. Eighth edition* (John Wiley & Sons Inc, 2005) (cit. on p. 41).

[128] C. M. Schneider, P. Bressler, P. Schuster, J. Kirschner, J. J. de Miguel, and R. Miranda, «Curie temperature of ultrathin films of fcc-cobalt epitaxially grown on atomically flat Cu(100) surfaces», Physical Review Letters **64**, 1059 (1990) (cit. on p. 41).

[129] H. van Kesteren and W. Zeper, «Controlling the Curie temperature of Co/Pt multilayer magneto-optical recording media», Journal of Magnetism and Magnetic Materials **120**, 271 (1993) (cit. on p. 41).

[130] P. J. Metaxas, J. P. Jamet, A. Mougin, M. Cormier, J. Ferré, V. Baltz, B. Rodmacq, B. Dieny, and R. L. Stamps, «Creep and Flow Regimes of Magnetic Domain-Wall Motion in Ultrathin Pt/Co/Pt Films with Perpendicular Anisotropy», Phys. Rev. Lett. **99**, 217208 (2007) (cit. on p. 41).

[131] S. Freercks, *in Preparation*, Ph.D. thesis, Universität Hamburg (2020) (cit. on pp. 41, 43, 45, 55, 56, 95, 113).

[132] S. Freercks, A. Philippi-Kobs, and H. P. Oepen, «Temperature-driven increase of perpendicular magnetic interface anisotropy in Co/Pt layered structures», in preperation (cit. on pp. 41, 43, 55, 113).

[133] J. Wagner, *The magnetic properties of ultrathin cobalt multilayers symmetrically and antisymmetrically sandwiched between layers of platinum and iridium*, Ph.D. thesis (2018) (cit. on pp. 41, 89, 131, 132).

[134] S. Freercks, *Temperaturabhangigkeit der Anisotropie in ferromagnetischen Nanostrukturen*, Master's thesis (2015) (cit. on pp. 43, 55).

[135] B. Barbara, W. Wernsdorfer, L. Sampaio, J. Park, C. Paulsen, M. Novak, R. Ferré, D. Mailly, R. Sessoli, A. Caneschi, K. Hasselbach, A. Benoit, and L. Thomas, «Mesoscopic quantum tunneling of the magnetization», J. Magn. Magn. Mater. **140–144**, 1825 (1995) (cit. on p. 43).

[136] W. Wernsdorfer, E. Bonet Orozco, K. Hasselbach, A. Benoit, D. Mailly, O. Kubo, H. Nakano, and B. Barbara, «Macroscopic Quantum Tunneling of Magnetization of Single Ferrimagnetic Nanoparticles of Barium Ferrite», Phys. Rev. Lett. **79**, 4014 (1997) (cit. on pp. 43, 54).

[137] B. Barbara and W. Wernsdorfer, «Quantum tunneling effect in magnetic particles», Current Opinion in Solid State and Materials Science **2**, 220 (1997) (cit. on p. 43).

[138] W. Wernsdorfer, *Classical and Quantum Magnetization Reversal Studied in Nanometer-Sized Particles and Clusters*, pp. 77–127 (Springer US, Boston, MA, 2006) (cit. on p. 43).

[139] C. L. Dennis, R. P. Borges, L. D. Buda, U. Ebels, J. F. Gregg, M. Hehn, E. Jouguelet, K. Ounadjela, I. Petej, I. L. Prejbeanu, and M. J. Thornton, «The defining length scales of mesomagnetism: a review», J. Phys.: Condens. Mat. **14**, R1175 (2002) (cit. on p. 43).

[140] S. Rao, E. D. Torre, L. H. Bennett, H. M. Seyoum, and R. E. Watson, «Temperature variation of the fluctuation field in Co/Pt», J. Appl. Phys. **97**, 10N113 (2005) (cit. on p. 43).

[141] E. Della Torre, L. H. Bennett, and R. E. Watson, «Extension of the Bloch $T^{3/2}$ Law to Magnetic Nanostructures: Bose-Einstein Condensation», Phys. Rev. Lett. **94**, 147210 (2005) (cit. on p. 43).

[142] K.-D. Durst and H. Kronmüller, «The coercive field of sintered and melt-spun NdFeB magnets», J. Magn. Magn. Mater. **68**, 63 (1987) (cit. on p. 43).

[143] S. Hashimoto, Y. Ochiai, and K. Aso, «Ultrathin Co/Pt and Co/Pd multilayered films as magneto-optical recording materials», Journal of Applied Physics **67**, 2136 (1990) (cit. on p. 43).

[144] D. Goll, M. Seeger, and H. Kronmüller, «Magnetic and microstructural properties of nanocrystalline exchange coupled PrFeB permanent magnets», Journal of Magnetism and Magnetic Materials **185**, 49 (1998) (cit. on p. 43).

[145] W. C. Nunes, W. S. D. Folly, J. P. Sinnecker, and M. A. Novak, «Temperature dependence of the coercive field in single-domain particle systems», Physical Review B **70** (2004) (cit. on p. 43).

[146] O. Fruchart, W. Wernsdorfer, J.-P. Nozières, D. Givord, F. Rousseaux, D. Mailly, D. Decanini, and F. Carcenac, «Arrays of ultrathin Fe 200-nm-wide particles investigated by microSQUID measurements», Journal of Magnetism and Magnetic Materials **198–199**, 228 (1999) (cit. on p. 44).

[147] O. Fruchart, J. Nozieres, W. Wernsdorfer, D. Givord, F. Rousseaux, and D. Decanini, «Enhanced coercivity in submicrometer-sized ultrathin epitaxial dots with in-plane magnetization», Phys. Rev. Lett. **82**, 1305 (1999) (cit. on p. 44).

[148] E. Bonet Orozco, W. Wernsdorfer, B. Barbara, A. Benoit, D. Mailly, and A. Thiaville, «Uniform rotation of magnetization measured in single nanometer-sized particles», J. Appl. Phys. **87**, 5097 (2000) (cit. on p. 44).

[149] C.-R. Chang, «Micromagnetic studies of coherent rotation with quartic crystalline anisotropy», J. Appl. Phys. **69**, 2431 (1991) (cit. on p. 44).

[150] H. Kronmüller, K.-D. Durst, and G. Martinek, «Angular dependence of the coercive field in sintered $Fe_{77}Nd_{15}B_8$ magnets», J. Magn. Magn. Mater. **69**, 149 (1987) (cit. on p. 44).

[151] M. Jamet, W. Wernsdorfer, C. Thirion, D. Mailly, V. Dupuis, P. Mélinon, and A. Pérez, «Magnetic Anisotropy of a Single Cobalt Nanocluster», Phys. Rev. Lett. **86**, 4676 (2001) (cit. on p. 45).

[152] C. Vouille, A. Thiaville, and J. Miltat, «Thermally activated switching of nanoparticles: A numerical study», J. Magn. Magn. Mater. **272–276**, E1237 (2004) (cit. on p. 45).

[153] B. Webb and S. Schultz, «Detection of the magnetization reversal of individual interacting single-domain particles within Co-Cr columnar thin-films», IEEE Trans. Magn. **24**, 3006 (1988) (cit. on pp. 51, 52).

[154] Y. Cornelissens and F. Peeters, «Response function of a Hall magnetosensor in the diffusive regime», J. Appl. Phys. **92**, 2006 (2002) (cit. on pp. 51, 52).

[155] W. Wernsdorfer, E. B. Orozco, K. Hasselbach, A. Benoit, B. Barbara, N. Demoncy, A. Loiseau, H. Pascard, and D. Mailly, «Experimental Evidence of the Néel-Brown Model of Magnetization Reversal», Physical Review Letters **78**, 1791 (1997) (cit. on p. 54).

[156] Z. Sun, S. T. Retterer, and D. Li, «The influence of ion-milling damage to magnetic properties of $Co_{80}Pt_{20}$ patterned perpendicular media», Journal of Physics D: Applied Physics **47**, 105001 (2014) (cit. on p. 58).

[157] J. Lee, C. Brombacher, J. Fidler, B. Dymerska, D. Suess, and M. Albrecht, «Contribution of the easy axis orientation, anisotropy distribution and dot size on the switching field distribution of bit patterned media», Appl. Phys. Lett. **99**, 062505 (2011) (cit. on p. 58).

[158] J. B. C. Engelen, M. Delalande, A. J. le Febre, T. Bolhuis, T. Shimatsu, N. Kikuchi, L. Abelmann, and J. C. Lodder, «Thermally induced switching

field distribution of a single CoPt dot in a large array», Nanotechnology **21**, 035703 (2010) (cit. on p. 58).

[159] H. Werners, «Magnetisierungsverhalten einzelnergekoppelter Co/Pt Nanopunkte», (2015) (cit. on p. 60).

[160] A. Neumann, *Temperaturabhängige Messungen an superparamagnetischen Nanodots mittels des anomalen Hall-Effektes*, Master's thesis, Universität Hamburg (2010) (cit. on pp. 61, 62).

[161] J. Crangle and W. R. Scott, «Dilute Ferromagnetic Alloys», Journal of Applied Physics **36**, 921 (1965) (cit. on pp. 62, 113).

[162] P. Gambardella, S. Rusponi, M. Veronese, S. S. Dhesi, C. Grazioli, A. Dallmeyer, I. Cabria, R. Zeller, P. H. Dederichs, K. Kern, C. Carbone, and H. Brune, «Giant Magnetic Anisotropy of Single Cobalt Atoms and Nanoparticles», Science **300**, 1130 (2003) (cit. on p. 62).

[163] S. R. De Groot, *Thermodynamics of Irreversible Processes* (North Holland, 1951) (cit. on p. 63).

[164] J. F. Nye, *Physical properties of crystals: Their representation by tensorsand matrices* (Oxford University Press, 1957) (cit. on p. 63).

[165] L. Onsager, «Reciprocal Relations in Irreversible Processes. I.», Physical Review **37**, 405 (1931) (cit. on p. 63).

[166] B. Leven, U. Nowak, and G. Dumpich, «Domain wall resistance in (Co/Pt)10-nanowires», Europhysics Letters (EPL) **70**, 803 (2005) (cit. on p. 69).

[167] R. Peierls, «Zur Theorie der magnetischen Widerstandsänderung», Annalen der Physik **402**, 97 (1931) (cit. on p. 72).

[168] B. Raquet, M. Viret, E. Sondergard, O. Cespedes, and R. Mamy, «Electron-magnon scattering and magnetic resistivity in 3*d* ferromagnets», Phys. Rev. B **66**, 024433 (2002) (cit. on p. 72).

[169] M. Hille, *Magnetotransport-Untersuchungen in Co/Pt-Drahten unter Berucksichtigung der Domanenstruktur*, Ph.D. thesis (2013) (cit. on p. 74).

[170] S. Ziesmann, «Untersuchung der Magnetowiderstandseffekte von nanostrukturierten Pt/Co/Pt-Schichtsystemen», (2016) (cit. on p. 74).

[171] P. Krone, D. Makarov, M. Albrecht, and T. Schrefl, «Magnetization reversal of bit patterned media: Role of the angular orientation of the magnetic anisotropy axes», J. Appl. Phys. **108**, 013906 (2010) (cit. on pp. 77, 96).

[172] W. Wernsdorfer, K. Hasselbach, A. Benoit, G. Cernicchiaro, D. Mailly, B. Barbara, and L. Thomas, «Measurement of the dynamics of the magnetization reversal in individual single-domain Co particles», J. Magn. Magn. Mater. **151**, 38 (1995) (cit. on p. 86).

[173] C. A. Ross, R. Chantrell, M. Hwang, M. Farhoud, T. A. Savas, Y. Hao, H. I. Smith, F. M. Ross, M. Redjdal, and F. B. Humphrey, «Incoherent magnetization reversal in 30-nm Ni particles», Phys. Rev. B **62**, 14252 (2000) (cit. on p. 87).

[174] M. Delalande, J. de Vries, L. Abelmann, and J. Lodder, «Measurement of the nucleation and domain depinning field in a single Co/Pt multilayer dot by Anomalous Hall effect», J. Magn. Magn. Mater. **324**, 1277 (2012) (cit. on pp. 87, 126).

[175] N. Kikuchi, R. Murillo, J. Lodder, K. Mitsuzuka, and T. Shimatsu, «Magnetization process of high anisotropy CoPt nanosized dots», IEEE Trans. Magn. **41**, 3613 (2005) (cit. on p. 88).

[176] N. Kikuchi, K. Mitsuzuka, T. Shimatsu, O. Kitakami, and H. Aoi, «Nucleation size of hcp-CoPt dot arrays characterized by time dependence of coercivity», Journal of Physics: Conference Series **200**, 102003 (2010) (cit. on p. 88).

[177] J. W. Lau, R. D. McMichael, S. H. Chung, J. O. Rantschler, V. Parekh, and D. Litvinov, «Microstructural origin of switching field distribution in patterned Co/Pd multilayer nanodots», Appl. Phys. Lett. **92**, 012506 (2008) (cit. on pp. 88, 131).

[178] N. Kikuchi, Y. Murayama, Y. Murakami, S. Okamoto, D. Shindo, and O. Kitakami, «Correlation between Switching Field and Microstructure of Individual Co/Pt Dots», Japanese Journal of Applied Physics **51**, 103002 (2012) (cit. on pp. 88, 131).

[179] J. Weissmuller, R. D. McMichael, A. Michels, and R. D. Shull, «Small-angle neutron scattering by the magnetic microstructure of nanocrystalline

ferromagnets near saturation», Journal of Research of the National Institute of Standards and Technology **104**, 261 (1999) (cit. on p. 89).

[180] H. A. Alperin, O. Steinsvoll, G. Shirane, and R. Nathans, «Observation of the Dispersion Relation for Spin Waves in Hexagonal Cobalt», Journal of Applied Physics **37**, 1052 (1966) (cit. on p. 89).

[181] G. Shirane, V. J. Minkiewicz, and R. Nathans, «Spin Waves in 3d Metals», Journal of Applied Physics **39**, 383 (1968) (cit. on p. 89).

[182] S. Chikazumi, *Physics of Ferromagnetism* (Oxford Press, 2009) (cit. on p. 89).

[183] J. Leliaert, B. Van de Wiele, A. Vansteenkiste, L. Laurson, G. Durin, L. Dupré, and B. Van Waeyenberge, «Current-driven domain wall mobility in polycrystalline Permalloy nanowires: A numerical study», Journal of Applied Physics **115**, 233903 (2014) (cit. on p. 90).

[184] J. Lau, R. McMichael, and M. Donahue, «Implementation of Two-Dimensional Polycrystalline Grains in Object Oriented Micromagnetic Framework», Journal of Research of the National Institute of Standards and Technology **114**, 57 (2009) (cit. on p. 90).

[185] R. H. Victora, S. D. Willoughby, J. M. MacLaren, and Jianhua Xue, «Effects of grain boundaries on magnetic properties of recording media», IEEE Transactions on Magnetics **39**, 710 (2003) (cit. on p. 91).

[186] T. Schrefl and J. Fidler, «3D calculation of magnetization processes in Co/Pt multilayers», Journal of Magnetism and Magnetic Materials **155**, 389 (1996), international Conference on Magnetic Recording Media (cit. on p. 96).

[187] Y. M. Jin, Y. U. Wang, A. Kazaryan, Y. Wang, D. E. Laughlin, and A. G. Khachaturyan, «Magnetic structure and hysteresis in hard magnetic nanocrystalline film: Computer simulation», Journal of Applied Physics **92**, 6172 (2002) (cit. on p. 96).

[188] L. Kaganovskiy, S. Khizroev, and D. Litvinov, «Influence of low anisotropy inclusions on magnetization reversal in bit-patterned arrays», J. Appl. Phys. **111**, 033924 (2012) (cit. on p. 96).

[189] L. Kaganovskiy, J. W. Lau, S. Khizroev, and D. Litvinov, «Influence of a low anisotropy grain on magnetization reversal in polycrystalline bit-patterned media», Journal of Applied Physics **114**, 123909 (2013) (cit. on p. 96).

[190] R. Skomski, H. Zeng, and D. Sellmyer, «Grain-boundary micromagnetism», IEEE Transactions on Magnetics **37**, 2549 (2001) (cit. on p. 108).

[191] J. Sichau, *Electron Spin Resonance Studies on Spin-Orbit Interactions in Graphene*, Ph.D. thesis, Fakultät für Mathematik, Informatik und Naturwissenschaften Fachbereich Physik der Universität Hamburg (2019) (cit. on p. 132).

Publications

Articles

R. A. Griffiths, P. W. Nutter, A. Neumann, C. Thönnißen, E.-S. Wilhelm, and T. Thomson: Signal asymmetries in the anomalous Hall effect of bilayer magnetic nanostructures, Appl. Phys. Lett. 109, 132401, 2016

S. Freercks, S. Hesse, A. Neumann, P. Staeck, C. Thönnißen, E.-S. Wilhelm, and H.P. Oepen: Magnetic Behavior of Single Nanostructures and their Mutual Interactions in Small Ensembles in "Atomic- and Nanoscale Magnetism", Springer Nature, Basel, 2018

Conference Contributions

S. Freercks, C. Thönnißen, E.-S. Wilhelm, P. Staeck, and H. P. Oepen, «Determining anisotropy and magnetic moment of single nanodots from switching time measurements», Talk at the Spring-meeting of the German Physical Society (DPG) 2017, Dresden (Germany).

S. Freercks, P. Staeck, C. Thönnißen, E.-S. Wilhelm, A. Neumann, and H. P. Oepen, «Magnetization behavior and interactions of single magnetic nanodots», Poster at the Spring-meeting of the German Physical Society (DPG) 2017, Dresden (Germany). 128

E.-S. Wilhelm, S. Freercks, P. Staeck, C. Thönnißen, and H.P. Oepen, «Noncoherent reversal of magnetization in single Pt/Co/Pt nanodots with diameter below 100nm», at the Spring-meeting of the German Physical Society (DPG) 2018, Berlin (Germany)

S. Freercks E.-S. Wilhelm, C. Thönnißen, P. Staeck, and H. P. Oepen, «Temperature dependence of the magnetic anisotropy of Pt/Co/Pt nanodots» at the Spring-meeting of the German Physical Society (DPG) 2018, Berlin (Germany)

Acknowledgements

This thesis would have never been possible without the support of many people. First of all im very grateful to Prof. Dr. Hans Peter Oepen for giving me the opportunity to do all the experiments and write this thesis. He guided me with valuable information, discussions and critical questions while leaving me the freedom to find my own way.
I am also very thankful to Prof. Dr. Robert Blick for refereeing this thesis as a second assessor.
Furthermore I would like to thank Dr. Carsten Thönnißen for taking a lot of time and effort, introducing me to the secrets of lithography and cryostats and for reading and discussing this manuscript. I would like to thank my office mate and dot team colleague Stefan Freercks for the best plant care ever, the great teamwork while moving and the nice time in ChyN. To Dr. Philip Staeck I'm very grateful for having come up with mumax 3 and discussions about tilting. Jonathan Jacobsohn was very helpful with fabricating the films in the sputter chamber. He also introduced me to MOKE and XRR, I am very thankful to him. I would like to thank also Dr. Robert Frömter for sharing knowledge whenever needed and discussing it. I am also very thankful to Fabian Kloodt-Twesten, Dr. Jochen Wagner, Dr. Susanne Kuhrau and Dr. Afsaneh Farhadi Ghalati for sharing this experience, many discussions and having a good time. I would also like to thank our technicians Sonja Hesselmann und Brigitte Muhlack for all the support they gave, and all former members of group G as well as the group of/and Prof. Huse for hosting us the last months. I am also very thankful to the SFB students for our great "Kegel" nights and exchange. I would like to thank Ricardo Viana for helping us move the Spectromag and fixing it and providing us with cryo expert knowledge. I would also like to thank the Helium-Team Alina Trumpjahn and Gerd Neuber for letting us stay cool.
Finally, I am very grateful to my family and friends, especially my parents for all their support and patience, Dr. Birte Baudis for being the best friend ever and all these uplifting phone calls and my partner Max Kesberger for his love, his never ending humor and best Brezel and Germknödel in the world!

Eidesstattliche Versicherung / Declaration on oath

Hiermit versichere ich an Eides statt, die vorliegende Dissertationsschrift selbst verfasst und keine anderen als die angegebenen Hilfsmittel und Quellen benutzt zu haben. Die eingereichte schriftliche Fassung entspricht der auf dem elektronischen Speichermedium. Die Dissertation wurde in der vorgelegten oder einer ähnlichen Form nicht schon einmal in einem früheren Promotionsverfahren angenommen oder als ungenügend beurteilt.

Hamburg, im März 2020